Spring 1-1-2016

Modeling of Post-Tensioned Rocking Bridge Columns

Brandon William Bowman
University of Colorado at Boulder, brbo1040@colorado.edu

Modeling of Post-Tensioned Rocking

Bridge Columns

Brandon Bowman

B.A., University of West Virginia, 2014

A thesis submitted to the Department of Civil, Environmental, and Architectural Engineering at the

University of Colorado at Boulder in partial fulfillment of the requirements for the degree of

Master of Science

2016

This thesis entitled:

Modeling of Post-Tensioned Rocking Bridge Columns

written by Brandon William Bowman

has been approved by the Department Civil, Environmental and Architectural Engineering

---

Petros Sideris

Ross Corotis

Yunping Xi

Date   4/22/16

The final copy of this thesis has been examined by the signatories, and we find that both the content and the form meet acceptable presentation standards of scholarly work in the above mentioned discipline

ABSTRACT

Bowman, Brandon (M.S Civil Engineering)

Modeling of Post-Tensioned Rocking Bridge Columns

Thesis directed by Assistant Professor Petros Sideris

Two separate columns were studied for this thesis. The first column was a column designed and tested by Marriot (2009) this column had energy dissipating (ED) links (or dissipators) and four internal unbonded tendons which served as a self-centering mechanism for the rocking column. The second column was a column designed and tested by (Sideris, 2012). This column did not include ED links and had eight internal unbonded tendons that served as a self-centering mechanism for the rocking column. The column by Sideris also included sliding at the segmental joints, which was not considered herein, as this thesis focuses solely on rocking columns. Two analytical models were created for each column with two modeling approaches for the contact interface (at the rocking joint), calibrated through parametric studies in this thesis. Parametric studies were also performed for design parameters to investigate their effect on the overall response of the columns.

The column by (Sideris, 2012) was further subjected to an Incremental Dynamic Analysis (IDA). The far-field record set from FEMA-P695 was used and scaled to the model/experimental domain through similitude analysis, since the column was not the prototype structure. The IDA looked at the effect of assuming that tendons fracture at a strain of 7.00% (typical design assumption), compared to experimental data gathered, which concluded that the individual wires start to fracture at 2.41% (Sideris, Aref, & Filiatrault, 2014) Damage measures (DMs) were recorded for each IDA and the probability of them exceeding specified limit states (LSs, threshold values representing damage states) under given seismic intensity, represented by a selected intensity measure (IM), was calculated. With this data, fragility curves were produced to compare the responses of the two separate IDA's.

DEDICATION

Dedicated to my parents, **Paul** and **Margaret**

My older sister, **Amanda**

My younger brother, **Zachary**

My cousin and good friend, **Eric**

And my late uncle, **Tim**

Without my family's continued support and encouragement throughout my undergraduate and graduate studies; I wouldn't have been able to accomplish as much as I have.

ACKNOWLEDGEMENTS

TABLE OF CONTENTS

TABLE OF FIGURES

INTRODUCTION

1.1. Literature Review on Post-tensioned Bridge Columns

During major earthquakes, the transportation system is extremely vulnerable and is mostly designed to prevent collapse. Interstate bridges that sustain large residual displacements following an earthquake can lose functionality. If a major corridor leading into a city becomes impassable, the social and economic effects become catastrophic. The first responders after an earthquake must be able to use the main corridors for quick access to the city. Seismic structural systems capable of low structural damage, and reduced downtime after a design-level earthquake are imperative. (Marriott, Pampanin, & Palermo, 2009). Post-tensioned rocking structural systems are an emerging technology that will help prevent large residual displacements. Post-tensioned rocking columns are essentially rigid bodies allowed to rotate at the base. Because there is no continuous longitudinal reinforcement at the base, the column is allowed to rock. The post-tensioned tendons; however, are continuous from the foundation to the top of the column. The tendons are situated in ducts that are roughly twice the diameter of the tendon. The tendons are typically unbonded to spread locally induced deformations over larger lengths and reduce residual displacements by self-centering the column with the post-tensioned force. Rocking post-tensioned columns have been proposed and studied by numerous researchers. (Hewes & Priestley, 2002) (Mander & Cheng, 1997) (Ou, Chiewanichakorn, Aref, & Lee, 2007) (Roh & Reinhorn, 2010) (Lee & Billington, 2011). (Marriott, Pampanin, & Palermo, 2009)

1.2. Modeling Challenges – Literature Review

Many challenges can be faced when modeling rocking columns, involving modeling of post-tensioned tendon fracture, contact and opening at the rocking joint, constraining of the tendon inside the ducts, and application of initial strains (initial post-tensioning) to the tendons. To model the tendons in OpenSEES, (Trono, 2014) used a gap material to prevent compression in series with an initial strain material to apply the initial post-tensioning. This approach did not take into account fracture of the tendon. The material would remain elastic and never fracture.

Modeling the contact surface is the most challenging part of modeling rocking systems. Two approaches were taken when modeling this system. The first was a multi-spring contact surface,

which is one of the more common approaches to modeling rocking systems. (Marriott, Pampanin, & Palermo, 2009) used multiple elastic, compression only, spring elements in Ruaumoko. Their approach defined the axial stiffness to be a function of the width/depth ratio, concrete properties, and cantilevered length of the column. Trono (2014) also used a set of compression only, vertical springs, defined as zero length elements (with an internal length). The element was defined with a compression-only material enabling uplift of the rocking plane. During rocking one side of the column is loses contact (uplift), while the other side is resisted by the compression force of the springs. A challenge involved with modeling many springs was the number of springs to have. A parametric study was done to find where the results started to converge. It is best to use the least amount of springs possible in order to speed up analysis time, but still have enough to capture the response of the interface accurately.

An alternative approach to model the rocking interface was considered by (Salehi & Sideris, 2016), who introduced a finite length two-node special joint element – termed hybrid sliding-rocking (HSR) joint element – on the basis of the flexibility-based element formulation. The HSR joint is a 2D two-node joint element of finite length that uses an empirical rocking model of the equivalent plastic hinge length. Rocking occurs at the mid-length of the element by using material models of no tensile strength, similar to the approach of the multi-spring contact surface. The strains are integrated using an adaptive weight, which changes, as the joint separation grows based on the equivalent plastic hinge length. (Salehi & Sideris, 2016). The plastic hinge length is a model parameter that typically varies between 80% to 110% of the cross-section depth. Although this element allows both sliding and rocking, it can be used for rocking-only systems by using a high friction input value to inhibit sliding.

Constraining the tendon inside the duct is important so that the actual physical geometry of the system is maintained. Typically, zero length gap elements can be used to achieve that (Salehi & Sideris, 2016).

1.3. Research Objectives and Scope

The objective of this research is investigate and assess the two aforementioned modeling strategies for rocking columns and quantify the effect of premature tendon fracture on the performance of bridges with rocking columns. Typically, seven-wire monostrands are designed to fracture at 7% strain; however, recent research (Sideris, Aref, & Filiatrault, 2014) has shown that

for unbonded post-tensioning systems, these monostrands fracture prematurely at the location of the anchorage hardware. This fracture occurs wire-by-wire and the first wire fracture may occur at strains of 2 % or less.

Parametric studies were done to investigate the effect of certain *design* and *model* parameters. The design parameters were of special importance because they are the parameters that can be changed in real world applications to obtain better performance for the bridge piers. The parametric study for the model parameters was performed to converge to the experimental data and validate the model.

1.4. Thesis Organization

Following this introductory chapter, Chapter 2 presents analytical models of two separate columns. The two columns examined were from a test by (Marriott, 2009) and a test by (Sideris, 2012). Modeling the contact surface is the most important part of rocking column systems. Chapter 2 is separated into two sections. Section 2.1 discusses the analytical model for the multi-spring contact surface. Section 2.2 describes the analytical model for the HSR joint contact surface. In each section, the loading protocol for the separate tests will be discussed, the mass calculations will be presented, the materials and their respective material models will be discussed as well as the elements used. The gravity analysis and convergence criteria are both presented in Section 2.1 and left out of Section 2.2 because they are identical procedures. Both sections have a parametric study that investigates model and design parameters and their implications to a static pushover response. Chapter 3 presents a performance assessment of bridges with rocking columns. This chapter investigates the performance of the bridge columns under seismic loading. Chapter 4 discusses the findings of the research.

2. MODELING APPROACHES

2.1. Multi-spring Contact Modeling

2.1.1. Implementation for column by Marriott

2.1.1.1. Model Description

An analytical model was developed to match the experimental results of a study that Marriott et al. (2009) performed. Their test specimens were a 1/3 scale single degree of freedom bridge pier. As shown in Figure 1, the bridge pier had a height of 4.8 meters scaled down to roughly 60 inches and a deck load of 1800kN scaled down to 67 kips. The bridge pier has a square cross section of 1.05 m scaled down to roughly 14 inches. Marriott et al (2009) tested 7 bridge piers each having different types of energy dissipating links (dissipators) and/or post-tensioning systems. Marriott tested internally grouted energy dissipators, internally grouted and threaded dissipators, external (replaceable) dissipators, internally threaded (semi-replaceable) dissipators, and 3 separate columns without dissipations. The analytical model developed in this thesis is a hybrid bridge pier with internal unbonded post-tensioning and external (replaceable) dissipators, in the form of buckling-restrained steel yielding elements.
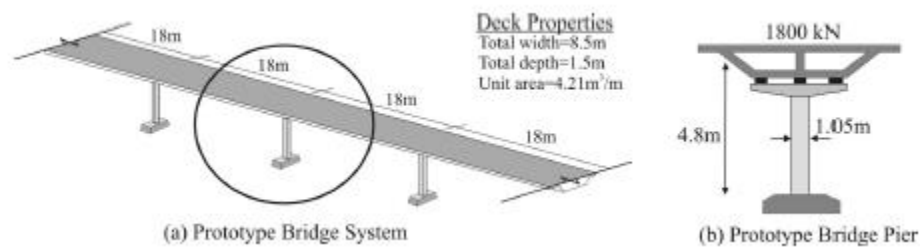
Figure 1. Prototype Bridge Pier (Marriott, 2009)

The post-tensioned bridge pier used in Marriot's experiment had a 1.6 m (60 in) cantilever length with a square cross section of 0.35m (14 in.). The rocking bridge pier had 8 dissipators; 2 on each face, spaced 115 mm (4.5 in.) apart as shown in Figure 2. The dissipators had a fuse length of 115 mm (4.5 in) and a fuse diameter of 8.0 mm (0.315 in). They were fabricated at the Civil Engineering Laboratory at the University of Canterbury from 20 mm (0.787in.) mild steel bar. The bar was placed in a lathe and the fused length was turned into the desired diameter. A 34 mm (1.34

in.) tube was then placed over the fused section of the bar and an epoxy was injected into the tube to prohibit buckling.
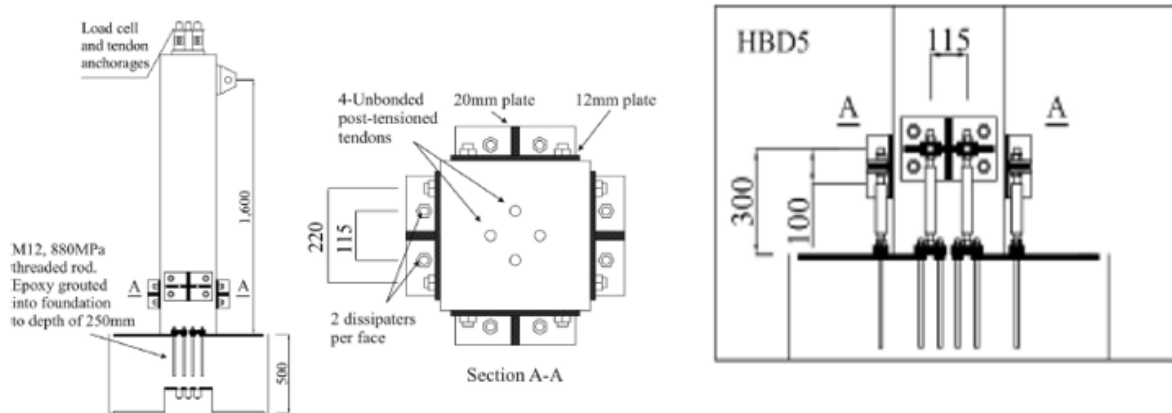
Figure 2. Construction drawing of the pier with external ED links (Marriott, 2009)

The column studied has four post-tensioned tendons and eight external dissipators. The 4 tendons are post-tensioned to 300 kN (67.4 kips), or 75kN (16.86kips) each. This post-tension force accounts for both the gravity load and the initial PT force. The post-tensioned tendons are essentially seven-wire monostrands of 0.5-inch diameter. Marriott et al (2009) carried out monotonic test on the tendons and they reported that the Modulus of Elasticity of the seven-wire strand to be 197100Mpa (28500 ksi), with a yield strength of 1560Mpa (226 ksi), with a yield strain of 0.00792. Marriott et al. did not test the tendons to rupture; so the data from the material testing carried out by the steel distributor were used, which identified the rupture strength to be 1850MPa (268 ksi). The 8 external mild steel machined dissipators have a fuse length of 115 mm (4.5 in) and a diameter of 8 mm (0.314 in). Marriott et al (2009) carried out monotonic tension testing on the ED links, which were found to have a modulus of elasticity of 193000 MPa (28000 ksi) and a yield strength of 320 MPa (46.4 ksi) with a yield strain of 0.00165. The rupture strength was found to be 461 MPa (67 ksi) with a rupture strain of 0.2.

Figure 2 above shows the layout of the dissipators and tendons. The post-tensioned tendons are placed in ducts and are not grouted to remain unbonded. With an unbonded post-tensioning system, the force in the stressed tendon is transferred to the concrete by the anchors at each end of the tendon. Since the anchors transfer most of force from the tendon to the concrete, they become very crucial throughout the service life. Unconfined cylinder concrete compression tests were carried out by (Marriott, 2009) and the strength of concrete at the first day of testing was found to be 54.1 MPa (7850 psi).

2.1.1.2. Loading

A uniaxial quasi-static loading protocol was used to test the columns. The loading protocol was adopted from the ACI recommendations "Acceptance criteria for moment frames based on structural test" (ACI (2001)). These criteria states:

"*1) Three fully reversed cycles shall be applied at each drift ratio.*

2) The initial drift ratio shall be within the essentially linear elastic response range for the module. Subsequent drift ratios shall be to values not less than one and one-quarter times, and not more than one and one-half times, the previous drift ratio

3) Testing shall continue with gradually increasing drift ratios until the drift ratio equals or exceeds 0.035"

The initial post-tensioning for the bridge pier represented the summation of the gravity load of the deck and the initial post-tensioned force of the prototype pier. As the lateral load was applied the axial force would increase due to the elongation of the tendons. The test set up is shown below in Figure 3 by (Marriott, 2009)
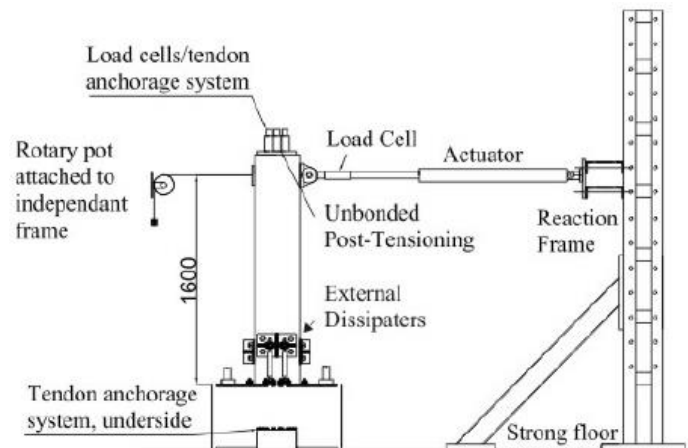
Figure 3. Test setup used by Marriott et al. (2009)

2.1.1.3. Seismic Mass

Marriott gives limited dimensions for the prototype bridge superstructure; therefore, the mass and mass moment of inertia of the superstructure were estimated. These approximate values were used to calculate the period of the system for dynamic analysis in the transverse direction. The

deck properties are shown in Figure 4. The prototype deck properties were converted to the model domain using the 1:3 scaling factor, as shown in Figure 5. The unit area of the prototype bridge deck is 4.21 m^2. The area is scaled down by a factor of 9 and then converted to inches to give a total model domain deck area of 725 in^2. A thin wall cross-section was then created with the outer dimensions equal to the width and height of the model domain cross-section to easily calculate the moment of inertia, as shown in Figure 6. The calculations for the mass moment of inertia can be found in Appendix I.

(a) Prototype Bridge System

Deck Properties
Total width=8.5m
Total depth=1.5m
Unit area=4.21m³/m

(b) Prototype Bridge Pier
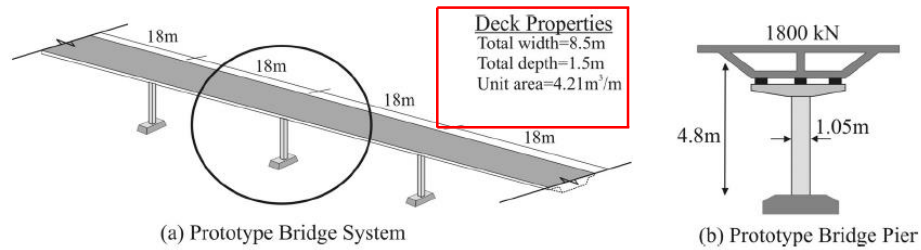
Figure 4. Deck properties
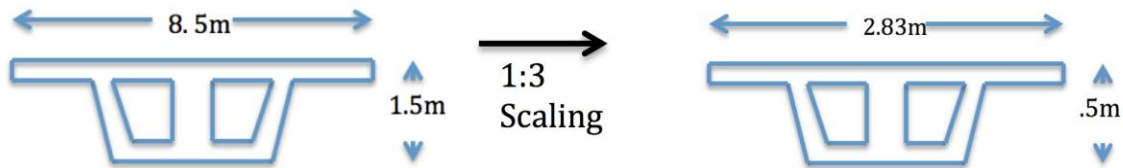
Figure 5. Prototype deck conversion to model domain
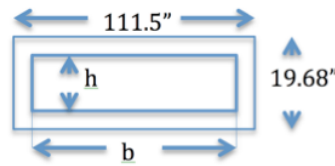
Figure 6 Approximate cross section

2.1.1.4. Material Models

Concrete

When modeling the concrete pier, it is important to model the concrete with two separate strengths. The cover concrete (unconfined concrete), can be modeled to replicate the cylinder concrete compression tests; however the confined concrete, or the concrete incased inside the confining hoops must be modeled accounting for the confining pressure. In low levels of stress, the confined concrete acts much like the unconfined concrete; however, when the concrete reaches

levels close to its uniaxial strength, the internal fracturing causes the concrete to dilate and bear out against the transverse reinforcement, which then causes the confining action. (Reddiar, 2009) When designing or modeling for structural concrete members in areas prone to seismic activity, that causes the concrete to reach its uniaxial strength, it is important to differentiate between the confined and unconfined concrete material. Kent and Park (1971) found out that there was no substantial increase in concrete compressive stress due to confinement. Their model didn't see a substantial increase in compressive strength because they were conducting small-scale test. They concluded that confinement only affected the slope of the post-peak branch (as shown Figure 7); however Scott et al. (1982) ran tests that were conducted at rapid strain rates to simulate seismic loading and found that there was a substantial increase in the compressive strength of confined concrete as shown in Figure 8. (Reddiar, 2009)
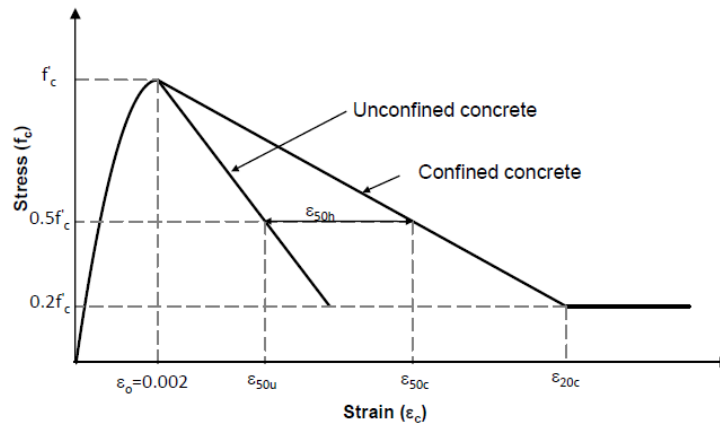
Figure 7 Modified Kent and Park model (Scott et al. 1982)
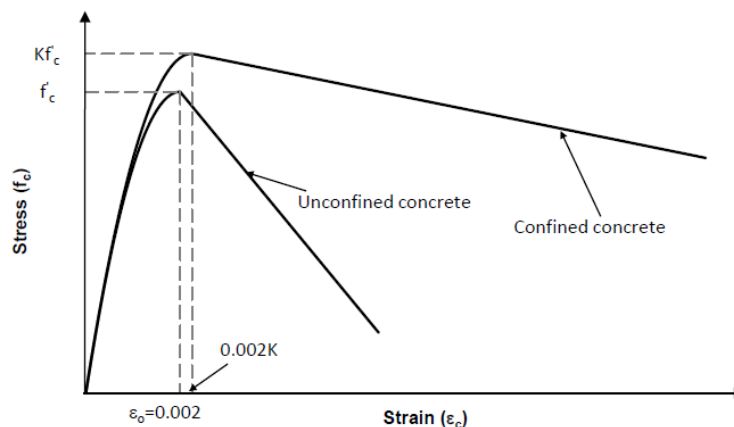
Figure 8 Stress-Strain Model for confined and unconfined concrete Kent & Park 1971

The reason that the results were different than the Kent and Park model was because Scott et al. ran larger scale tests that were more practical to real world applications as well as implement

rapid strain rates. Therefore, modifications were made to the Kent-Park model to incorporate the increase in compressive stress. A factor "K" was added to the model, which was a function of the transverse steel ratio, yield strength of hoops, and the original unconfined compressive strength of concrete. This K value could increase the confined compressive strength by a factor of 1.0-1.5 (Scott, Park, & Priestley, 1982).

Unconfined Concrete

For the unconfined cover concrete, the material *Concrete01* from the structural analysis program OpenSEES (OpenSees, 2016) was used. Concrete01 is a material model with degraded linear unloading/reloading stiffness and no tensile strength. Concrete01 has four parameters that must be inputted, namely, the 28-day compressive strength (f_c'), the strain at peak strength (ε_0), the strength at crushing, and the strain at spalling (ε_{sp}). For the cover concrete the peak compressive strength f'_c is given as 54.1 MPa (7850 psi) and the strain at peak strength is assumed to be 0.002. The strength, when the cover concrete has completely spalled and ceases to carry any stress, was taken as zero. The strain at spalling was found using the following equation from (Mander, Priestly, & Park, Theoretical Stress-Strain Model For Confined Concrete, 1988):

$$\varepsilon_{sp} = 0.012 - 0.0001 f_c' \quad \text{(f}_c\text{' in MPa)} \tag{1}$$

The material properties for the cover concrete are summarized in Table 1. The response for a compression test for the cover concrete is shown in Figure 9
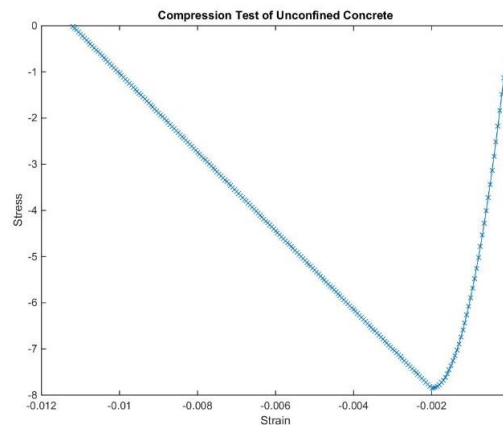
Figure 9 Compression test response for cover concrete using the OpenSees material Concrete01

Table 1 Cover Concrete Properties

Cover Concrete Parameters		
f_c'	54.1 Mpa	7850psi
ε_{c0}	0.002	
ε_{sp}	0.00659	

Confined Concrete

As stated above, it is important to differentiate between unconfined cover concrete and confined core concrete. Concrete01 was also used for the confined concrete material model; however, different values for the model parameters were used, based on the work of (Mander, Priestly, & Park, Theoretical Stress-Strain Model For Confined Concrete, 1988) & (Scott, Park, & Priestley, 1982). The material properties and material response that is trying to be achieved can be seen in Figure 10.
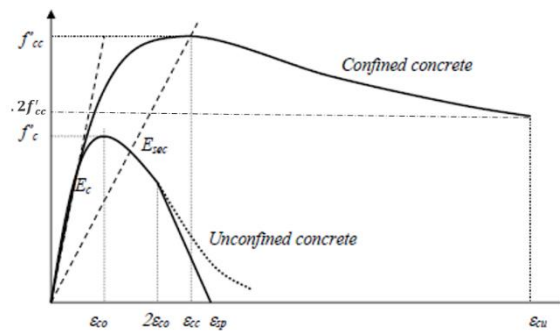
Figure 10. Material parameters of the confined and unconfined concrete

The maximum confined concrete stress f$_{cc}$' is found using the following equation:

$$f_{cc}' = f_c'\left(-1.254 + 2.254\sqrt{1 + \frac{7.94 f_1'}{f_c'}} - 2\frac{f_1'}{f_c'}\right) \tag{2}$$

where f_c' is the unconfined concrete compressive strength defined above (in MPa). The lateral confining stress (f_1') is defined by the following equation:

$$f_1' = k_e \rho_v f_{yh} \tag{3}$$

where the yield strength of the transverse reinforcement (f_{yh}) must be considered when calculating he confined strength of concrete. This causes the transverse reinforcement to yield. (Reddiar, 2009) The transverse reinforcement ratio (ρ_v) is calculated by:

$$\rho_v = \rho_{ax} + \rho_{ay} = \frac{A_{shx}}{hcy_s} + \frac{A_{shy}}{h_{cx}s} \tag{4}$$

where A_{shx} is the area of transverse reinforcement providing confinement in the x-direction and $A_{shx}=A_{shy}$ since we have a square column with equivalent reinforcement in each direction, $h_{cy}=h_{cx}$ which is the width of the confined core in the x and y direction, s is the spacing between the transverse reinforcement, k_e is the confinement effectiveness factor which is found from the following equation:

$$k_e = \frac{A_e}{A_{cc}} \tag{5}$$

where the effectively confined area $A_e = b_{ex} \times b_{ey}$. And the total confined core area $A_{cc} = h_{cx} \times h_{cy}$. **Error! Reference source not found.** illustrates the parameters used to calculate the transverse reinforcement ratio and the confinement effectiveness factor.
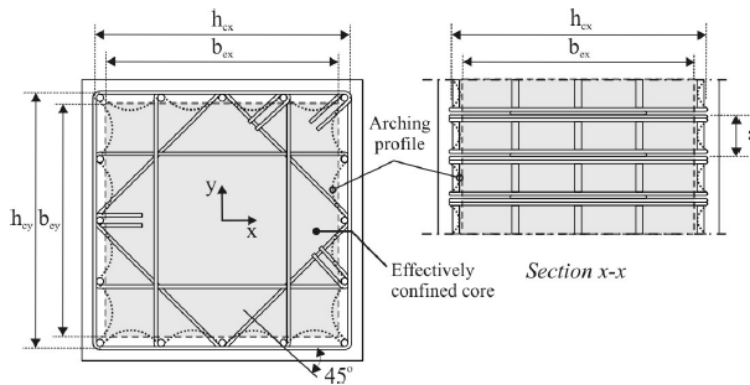
Figure 11 illustrates the parameters used to calculate the confinement effectiveness factor and the transverse reinforcement ratio (Marriott et al.)

The strain (ϵ_{cc}) at the maximum confined concrete stress was calculating using the following equation:

$$\varepsilon_{cc} = \varepsilon_{co} \left[1 + 5 \left(\frac{f'_{cc}}{f'_c} - 1 \right) \right] \tag{6}$$

The ultimate strength was taken as .2f$_{cc}$' and the ultimate strain was found using the following equation:

$$\varepsilon_{cu} = 0.004 + \frac{1.4\rho_{v}f_{yh}\varepsilon_{su}}{f_{cc}^{'}} \tag{7}$$

where ε_{su} is the ultimate steel strain of the transverse reinforcement. The material response of the confined concrete and unconfined concrete can be seen in Figure 12 and the summary of the material properties for the confined concrete can be seen in Table 2.

Table 2 Material properties for unconfined concrete

Confined Core Concrete Parameters			
$f_{cc}^{'}$	76.96		11161.8 Psi
ε_{cc}	0.006225		
ε_{cu}	0.022628		
$.2f_{cc}^{'}$	15.39 MPa		2232.4 Psi
ρ_{v}	0.016		
f_{yh}	320 MPa		46412.2 Psi
ke	0.75		
$f_{1}^{'}$	3.84 MPa		556.9 Psi
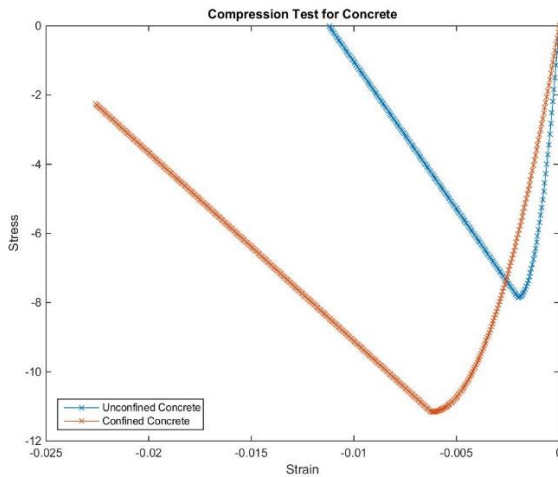
Figure 12 shows the comparison between the confined and unconfined concrete.

Tendons

The tendons used in Marriot's experiment were seven-wire strands that had a nominal diameter of 0.5 in. The modulus of Elasticity was found from a material test to be 28500 ksi with a yielding stress of 243 ksi and strength of 273 ksi. The tendon was modeled wire by wire to capture the fracture of individual strand wires. The tendon is made up of seven wires consisting of 6 outer wires and 1 inner wire. The outer wires have a diameter of 0.167 in. while the center wire, or inner wire, has a slightly larger diameter of 0.173 in as shown in Table 3.

Since rupture of individual wires at the anchorage hardware is the failure mode of unbonded tendons, it was determined that in the vicinity of the anchorage hardware, the tendon will be modeled by 7 individual corotTruss elements. The wires will fracture at different strains as indicated in the study by (Sideris, Aref, & Filiatrault, 2014) on the effects of anchorage hardware on the cyclic tensile response of unbonded monostrands. In this study, cyclic tests were conducted on five 0.5in-diameter monostrands of length of 53 inches and strains were recorded at each wire fracture. The mean strains of each wire failure are recorded in Table 4. Accordingly, an effective

length of 53 inches was considered in the modeling of the tendons for the column by Marriot et al (2009). This test was duplicated in an OpenSees model and compared to the actual test data. The comparison is shown in Figure 14 and Figure 15.

For the post-tensioning system, a material model called "*uniaxialMaterial PTSteel*" created in OpenSees by Salehi and Sideris (2016) was used. This is a tension-only material that follows the backbone curve of Mattock's model for PT monostrands (Mattock, Yamazaki , & Kattula, 1969). This material has 5 main parameters, namely, the elastic modulus of unbonded monostranded, E_{pt}, the nominal yield force of monostrand, f_{py}, the post-elastic to elastic modulus ratio, r_{pt}, the actual yield stress to nominal yield stress ratio, K, and the smoothness factor that controls transition from elastic to inelastic range, R. The calibrated values of these parameters for the 0.5 in monostrand are shown in Table 5 (Sideris, Aref, & Filiatrault, 2014). The material has an optional input of initial strain to apply the initial post-tensioning. A pure tension test was ran in OpenSees to validate the tendon model and its capability of capturing the successive wire fractures, as shown in Figure 13. The tendon model was then validated by comparing its response with the data from the cyclic tensile tests by (Sideris, Aref, & Filiatrault, 2014) as shown in Figure 14 and Figure 15.

Table 3 Geometry of wires

Nominal Diameter, in.	Outer Wire Diameter, in.	Center Wire Diameter, in.	Outer Wire Area, in^2	Center Wire Area, in^2.
0.5	0.167	0.173	0.02190	0.023506

Table 4. Strain at each wire fracture (Sideris, Aref, & Filiatrault, 2014)

Monostrand diameter	Fractured wire						
	1st	2nd	3rd	4th	5th	6th	7th
0.5 in.	0.0293	0.0359	0.0393	0.0437	0.0584	0.0596	0.0925

Table 5 Properties of 0.5in. Tendon

Property	0.5in monostrand
A_{PT} ,in^2 Area of Tendon	0.153
E_{PT} ,ksi Elastic modulus of unbonded monostrand	28,500
f_{py} Nominal yield force of monostrand	243
K, Actual yield stress to nominal yield stress of a mono	1.045
rPT Post-eleastic over elastic modulus of a monostran	0.015
R, Smoothness Factor	8
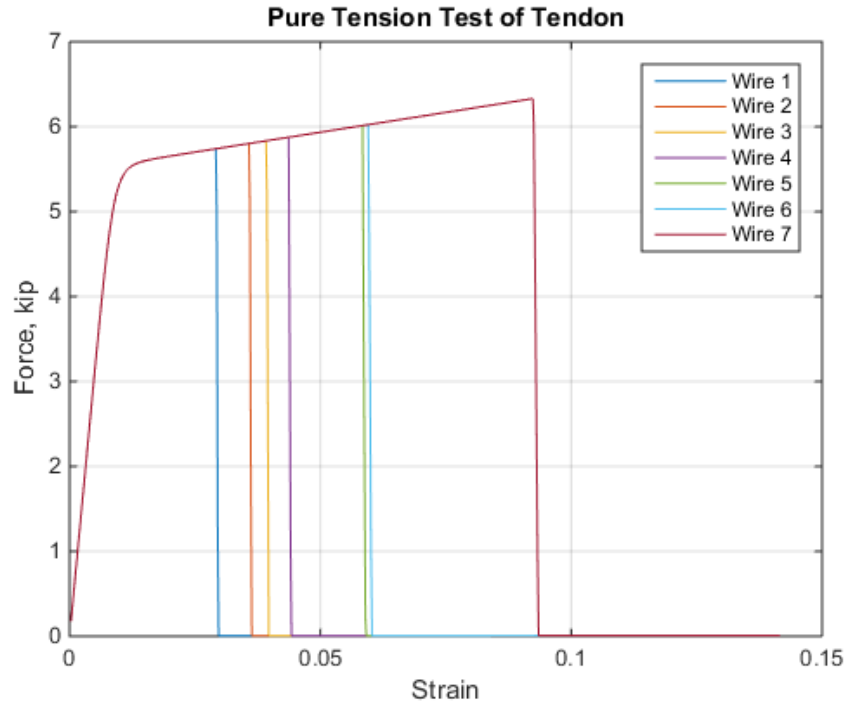
Figure 13. Pure tension test of Tendon.
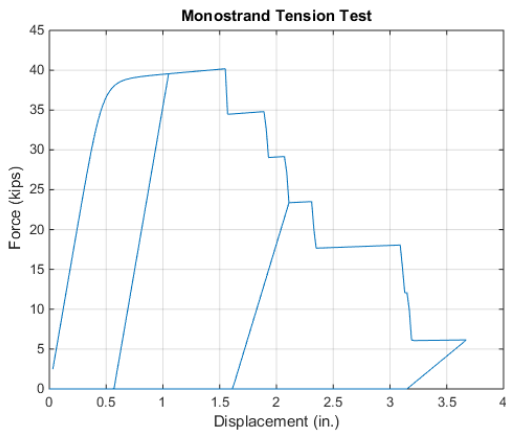
Figure 14. OpenSees model of .5in tendon under cyclic tensile loading
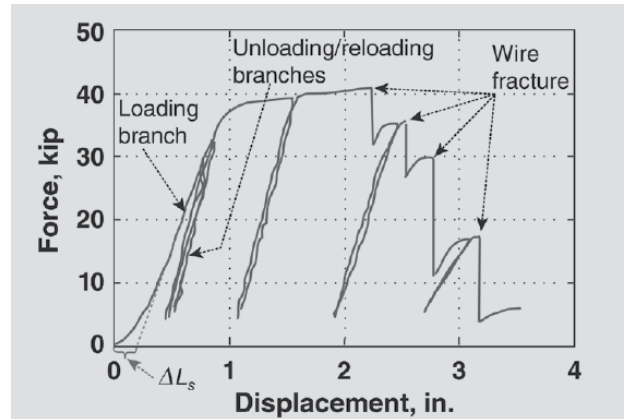
Figure 15. Experimental model of .5in tendon under cyclic tensile loading (Sideris, Aref, & Filiatrault, 2014)

Reinforcing Steel & Dissipater Material

The mild steel used for the longitudinal reinforcement, confining reinforcement, and dissipators had a modulus of elasticity of 193000 MPa (28,000 ksi), yield stress of 320 MPa (46.41 ksi), ultimate stress of 461 MPa (66.86 ksi), yield strain of 0.001657, and ultimate strain of 0.2. To model this material, the bilinear damage model, termed "*BilinDamage*", developed by by

Salehi and Sideris (2016) was used. This material modelled captures fracture of the elements, unlike existing models, e.g. *Steel02*. The Bilinear damage material model has 3 required input parameters and 3 optional input parameters. The required parameters are the yield stress, f_y, yield strain, ε_y, and strain hardening ratio, r_y. The three optional parameters are the strain at initiation of deterioration, eps$_1$, strain at the end of deterioration, eps$_2$, and the post-deterioration stress reduction factor, rf$_{min}$. The parameters were kept consistent with Marriott et al. experiment and are shown in Table 6. A test model was created in OpenSees to validate the response of the dissipaters and reinforcing steel under pure tension loading and cyclic loading, as shown in Figure 16 & Figure 17.

Table 6 Material properties for Longitudinal Reinforcement and Dissipators

Longitudinal Reinforcement & Dissipator Steel Properties		
Modulus of Elasticity, E	28000	ksi
Yield Strain, f_y	46.412	ksi
Ultimate Strength, f_u	66.86	ksi
Ultimate Strain, ε_u	0.2	
Yield Strain ε_y	0.0016576	
Post Yield Modulus	103.09	ksi
Strain Hardening Ratio r_y	0.00368194	
eps1	0.2	
eps2	0.21	
rfmin	0.001	
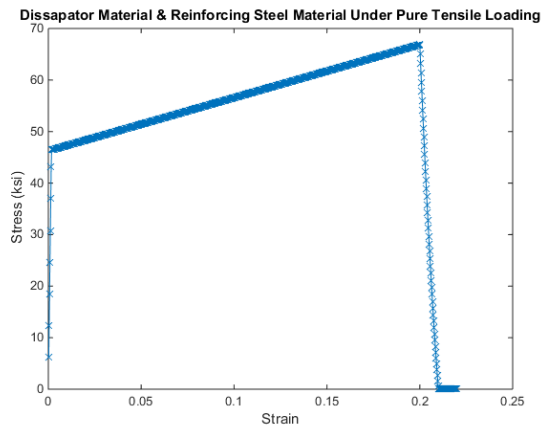
Figure 16 shows material test of reinforcing steel and dissipator steel with BiLinearDamage material under pure tension loading
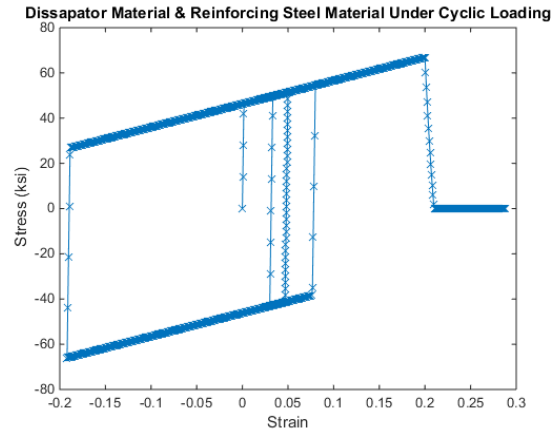
Figure 17 shows material test of reinforcing steel and dissipator steel with BiLinearDamage material under cyclic loading

2.1.1.5. Elements

Reinforced Concrete Column

The reinforced column is modeled using a force-based fiber element, with fiber sections which are composed of separate fibers containing separate uniaxial materials. The section command is used to create composite sections. Each fiber section is broken into patch fibers and layer fibers as shown in Figure 18. The cover concrete and confined concrete are rectangular patch fibers that are discretized into multiple subdivisions. The reinforcing steel is broken up into 5 vertical straight-line fibers with coordinates equal and area of steel equal to placement of the longitudinal steel. Three materials are used to construct the fiber section which include *Concrete01* for both the confined and unconfined concrete and *BiLinDamage* for the reinforcing steel. The fiber sections are then incorporated into the forceBeamColumn element, which is based on an iterative force-based formulation. The Gauss-Lobatto integration is used for the forceBeamColumn element and 2 integration points are used at each end of the element. The column consists of five 12" forceBeamColumn elements. The bottom forceBeamElement is connected to the contact element
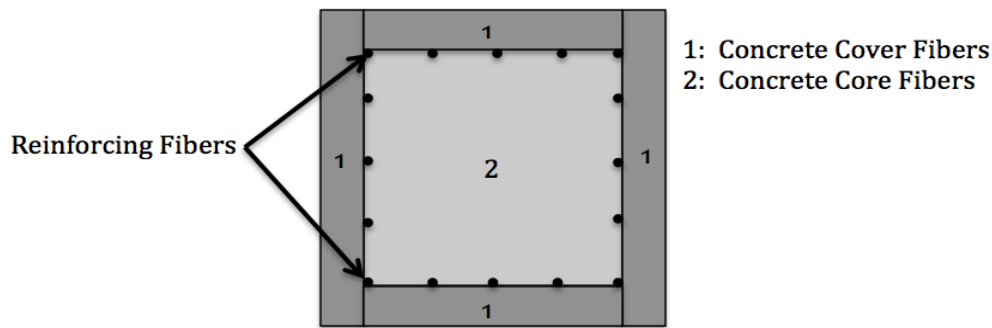
Figure 18. Cross-section separation into sub-sections with different material properties

Post-Tensioning Tendons

As mentioned earlier, the tendons are modeled with seven corotational truss elements – "corotTruss" elements – each representing an individual wire with separate fracture strains. The length of these elements was taken to be 53 inches, as explained earlier. The remaining length of the tendons was modeled using truss elements accounting for the entire diameter of the tendons. The corotational transformation was chosen because the strands will be inclined by the amount approximately equal to the base rotation as the column uplifts. (Trono, 2014).

The initial post-tensioning was statically applied as an initial strain in the material *PTsteel*.

Dissipators

The energy dissipators are coupons (dog bone shaped) made of mild steel as shown in Figure 19. The central fuse is modeled using a truss element. The two ends, which remain elastic, are modeled with an elastic beam element. The fuse of the dissipator was confined with a steel tube injected with epoxy to inhibit buckling.
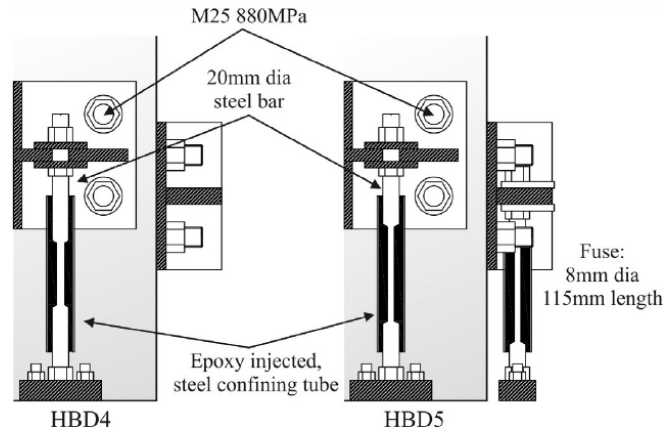
Figure 19 shows how the epoxy injected dissipators are connected to the column

Constraint

The duct constraining the tendon has a diameter of 0.9 inches. The tendon has a 0.5-inch diameter, so if the tendon is centered inside the duct it has a tolerance of 0.2inches on each side. In order to constrain this tendon inside that duct, a node was placed 0.2 inches away from the center of the tendon and connected to the column with a rigid link. A truss element was placed in between the nodes with a multi-linear elastic material - *elasticmultilinear* material in OpenSEES library. This material shows a very small stress of 0.1 ksi up to a strain of 1. Beyond that strain, the tendon has made contact with the restraining duct and a stress of 100ksi per .005 is applied to constrain the tendon inside the duct as shown Figure 20.
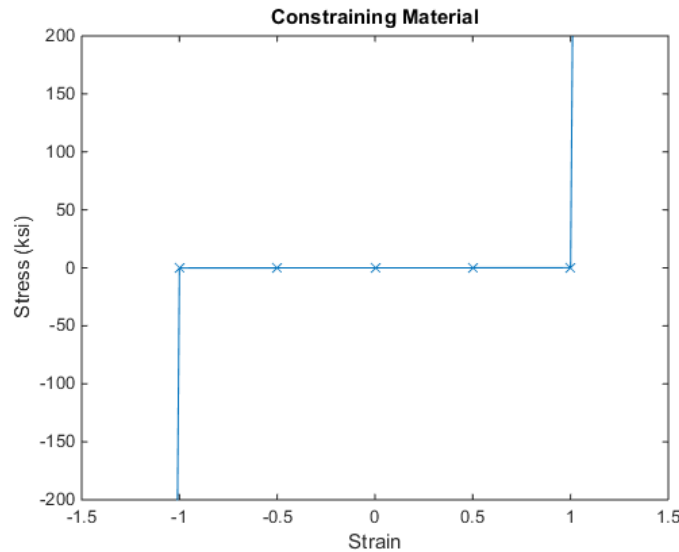
Figure 20. Multi-linear elastic material model to keep the tendon inside the duct

2.1.1.6. Gravity Analysis

For the gravity analysis, loads are placed at all the nodes connecting the concrete column elements. OpenSEES allows multiple linear equation solvers to find a solution for the linear system of equations Ku=P. The analytical model is not a linear system; however, for gravity analysis it is treated as such because it hasn't experienced any nonlinear effects yet. The *BandGeneral* solver was used for the gravity analysis in this model and it is a direct solver for banded unsymmetric matrices. The transformation method was used for the constraint equations in the analysis. The single-point constraints are done directly when doing the transformation method and the matrix equation is not manipulated to enforce them, instead trial displacements are set directly at the nodes at the start of each analysis step. Also, for the analysis, a Degree of Freedom numberer must be assigned so an *RCM* numberer was chosen to provide the mapping between the degree-of-freedom at the nodes and the equation numbers. The RCM numberer uses the reverse Cuthill-McKee scheme to order the matrix equations. This method is frequently used when the matrix being generated whose rows and columns are numbered according to the numbering of the nodes. When the nodes are renumbered internally it is possible to produce a matrix with a much smaller bandwidth which makes the matrix much quicker to solve. During the gravity analysis a convergence test is used which is separate from the convergence test used in the pushover and cyclic analyses. A normal displacement increment test is used in the model that uses the norm of

the left hand side solution vector of the matrix equation to determine if convergence has been reached. The *NormDispIncr* command in OpenSees requires a tolerance and a max number of iterations as an input. A very low tolerance of 1.0E-12 was used with 10 iterations to check before returning failure condition. The Newton Algorithm was used to solve the nonlinear residual equations because of its robust method for solving nonlinear algebraic equations. A static analysis was used for the gravity analysis with a load control integrator used with 10 steps of .1 to reach the load level. In order to keep the gravity applied through all of the analyses the command *LoadConst* was used which sets the loads constant in the domain and also resets the time in the domain which starts all the other analyses at time 0.0 with all the gravitational forces already applied.

2.1.1.7. Convergence Criteria

The same convergence criteria are used for both the monotonic and cyclic pushover analyses. First, the *NormDispIncr* is used similar to the gravity analysis except a lower tolerance of 1E-6 is used and 100 iterations is used. Multiple methods are used to achieve convergence if the original convergence test doesn't work. If convergence is not reached, the analysis step is repeated with a smaller time step size. If convergence still is not reached, the *energy increment test* is used rather than the *NormDispIncr*. This test uses the dot product of the solution vector and norm of the right hand side of the matrix equation to determine if convergence has been reached. The *Norm Unbalance Test* is then used, if convergence is still not reached. The last step to try to reach convergence is by increasing the tolerance on the *NormDispIncr* test. The tolerance is increased by E+2 then E+4, if convergence is still not achieved. If convergence still fails, analysis is aborted.

2.1.1.8. Element and Node Recorders

The purpose of the models is to investigate the response of certain materials and parameters. In order to do this, node and element recorders were added to the model. These recorders would record variables such as stress, strain, global forces, axial forces, displacements, and eigenvalues. A node recorder was placed at the top of the column, which recorded the displacement of the top column node. An element recorder was placed at a rigid link that was connected to the top column node to the application of the displacement (for static pushover purposes). Calculating the force in this element was the same as the summation of all the base forces, which simplified the analysis.

An element recorder was placed on the dissipators and the tendons to record the axial force and deformation. The cross section of the column had recorders that monitored the stress and strain of the reinforcing steel, cover concrete, and confined concrete as shown in Figure 21.
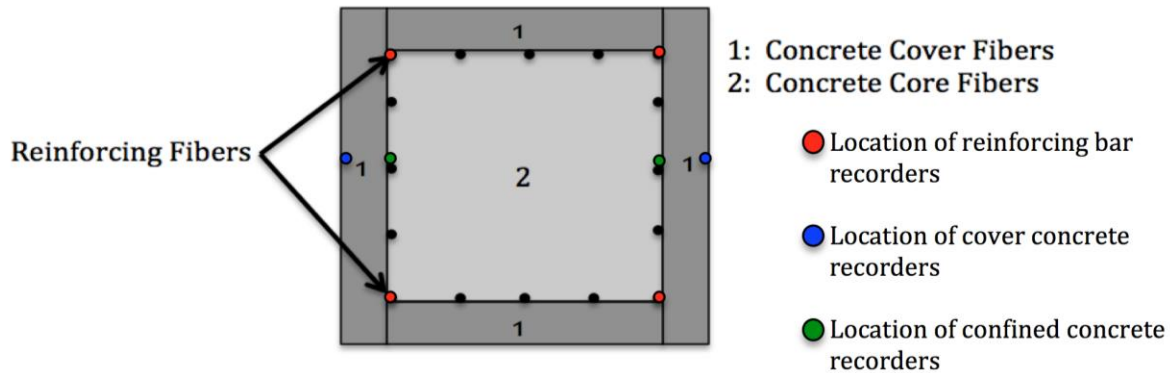
Figure 21 shows the locations of the recorders in the column cross section

2.1.1.9. Multi-Spring Contact Surface

The contact surface considered to simulate the rocking of a column is the most crucial part of modeling rocking columns. Two different contact concepts were implemented in modeling the rocking system, the first was a bed of compression contact springs that were added to the base of the column as shown in Figure 22. There are three types of springs at the rocking interface, accounting for the cover concrete, confined concrete, and longitudinal reinforcment, as shown in Figure 23. All springs have zero tensile strength and a compression force that was function of the area on which they are acting, number of springs and compressive strength of the concrete or steel.

The material used for the contact spring was either *Concrete01* (for the cover and confined concrete springs) or *BilinDamage* (for the longitudinal reinforcement springs). Concrete01 does not have tensile strength; however, the BilinDamage material does have tensile strength and only compressive contact springs should be consider. For this reason, the BilinDamage material was combined in series with a multi-linear elastic material to ensure that the spring cannot take a tension. The longitudinal reinforcement springs are modeled using five springs that are account for the five rows of reinforcement. The outer springs have an area equal to five longitudinal reinforcing bars, whereas the central springs have an area equal to two longitudinal reinforcing bars. The concrete springs have an area equal to the gross area of the columns cross section divided by the number of springs choosen.

The materials used for the contact springs have by default stress-strain input parameters. The springs should have force-displacement parameters; therefore, the stress values were multiplied by the area in which they act (depended on the number of springs) and the strain values were multiplied by an effect spring length, l_c, creating a force displacement relationship. The effective spring length and number of contact springs are analyzed in a parametric study presented in a later section. An overall summary of the multi-spring column is illustrated in Figure 24 .
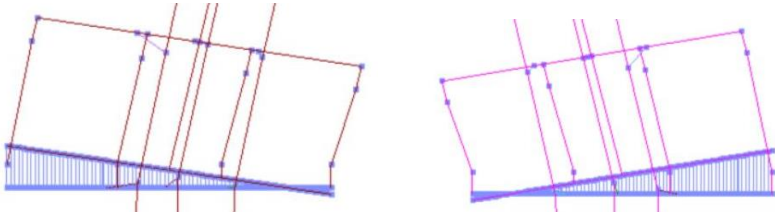
Figure 22. Distributed contact springs at the base that allow the system to rock back and forth
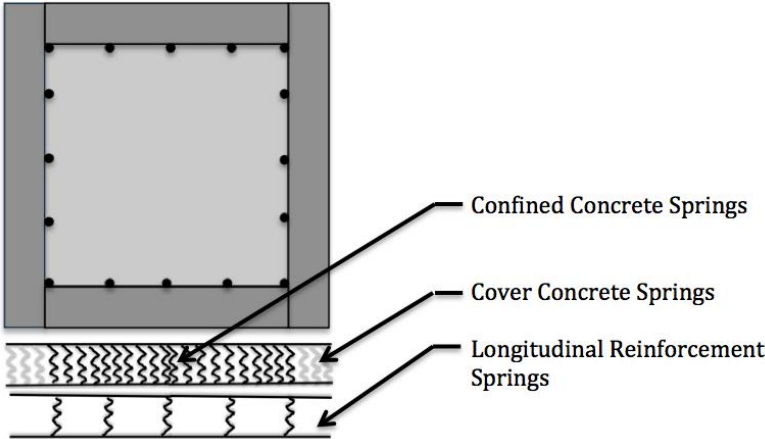
Figure 23 shows the 3 types of compression springs and their location in the rocking system

SUPERSTRUCTURE MASS

RIGID LINK CONNECTING
SUPERSTRUCTURE MASS TO TOP OF
COLUMN

RIGID LINKS CONNECTING TOP OF
POST-TENSIONED TENDONS &
REINFORCED CONCRETE COLUMN

FORCEBEAM COLUMN ELEMENTS W/ FIBER
SECTION (REINFORCED CONCRETE
COLUMN)

COROTTRUSS ELEMENTS
(POST-TENSIONED TENDONS) CENTRAL
TENDON IS OFFSET FOR VISUAL EFFECT

53" TENDON EFFECTIVE LENGTH

FORCEBEAM COLUMN ELEMENTS W/
FIBER SECTION (REINFORCED
CONCRETE COLUMN) TYPICAL

NODES THAT CONNECT MASSES
(RIGID LINK ELASTIC BEAMCOLUMN ELEMENTS)

NODES THAT CONNECT ZERO LENGTH ELEMENTS
(ZERO LENGTH ELEMENTS)

NODES THAT CONNECT DISSAPATORS
(TRUSS & ELASTICBEAMCOLUMN ELEMENTS)

NODES THAT CONNECT COLUMN ELEMENTS
(FORCE BEAM COLUMN ELEMENTS)

NODES THAT CONNECT TENDONS
(COROT TRUSS ELEMENTS)

NODE CONSTRAINING TENDON INSIDE DUCT
(ELASTICMULTILINEAR ELEMENT)

ELASTICMULTILINEAR ELEMENTS
CONSTRAING TENDON INSIDE DUCT

RIGID LINKS CONNECTING
DISSIPATORS TO REINFORCED
CONCRETE COLUMN

ELASTIC BEAM COLUMN ELEMENTS
(THICKER PART OF WISHBONE
SHAPE)

TRUSS ELEMENTS (THINNER FUSE MEMBER
THAT YIELD)

RIGID LINKS CONNECTING FREE
END OF ZERO LENGTH ELEMENTS

ZERO LENGTH CONTACT
ELEMENTS (SHOWN WITH LENGTH
FOR VISUAL EFFECTS)

MARRIOTT COLUMN: MODELING APPROACH: MULTIPLE
COMPRESSION SPRING ROCKING

Figure 24 Overall summary of the multi-spring model

2.1.1.10. Parametric Studies on Model Parameters

The concrete springs and the steel reinforcing springs were both connected by a zero length element at two nodes sharing the same coordinates with one of the nodes fixed and the other free. The nodes that were free were connected to the centroid at the column base through rigid links. A model was created to see the effect the number of springs has on the response of the column. According to Figure 25, as the number of springs was increased, the response converged. It was decided that 80 springs would be used to make the model converge even better.

Another modeling parameter that was tested was the lc length. The springs have zero length; however, the material used for the zero-length elements has an effective spring length (lc) built into the force-displacement of the material. This effective spring length is analyzed in Figure 26 with a reference value of 80 contact springs.
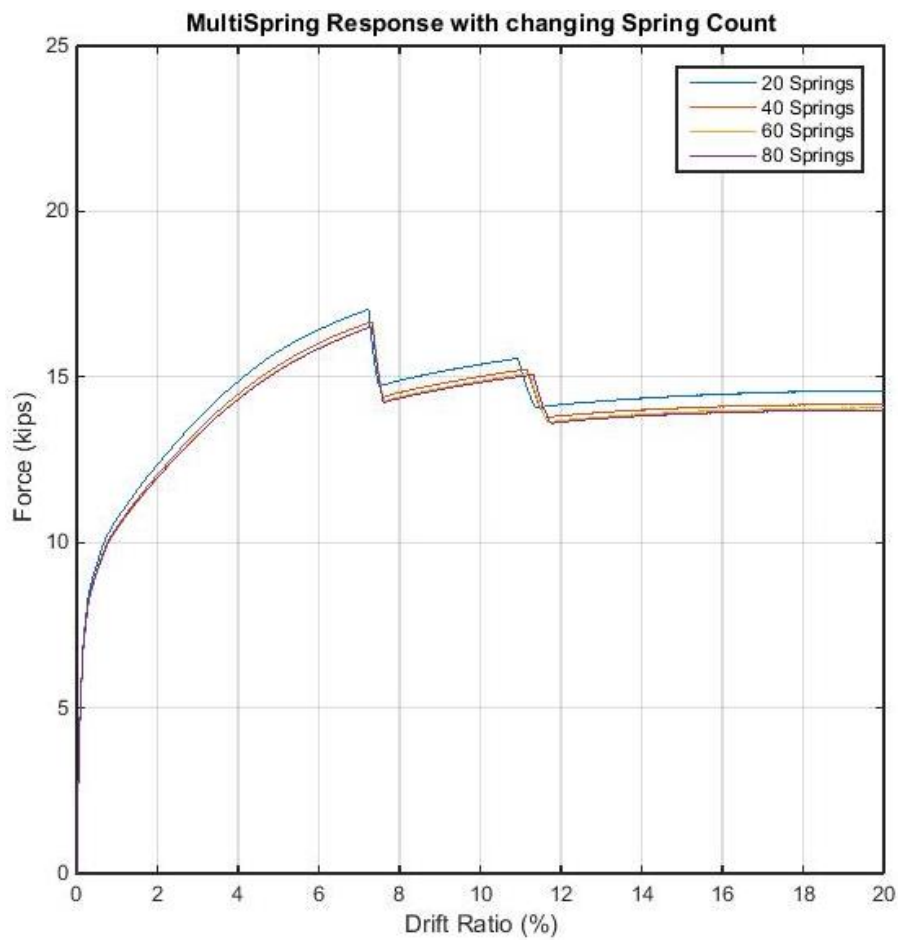
Figure 25 shows the effect the number of springs has on the response
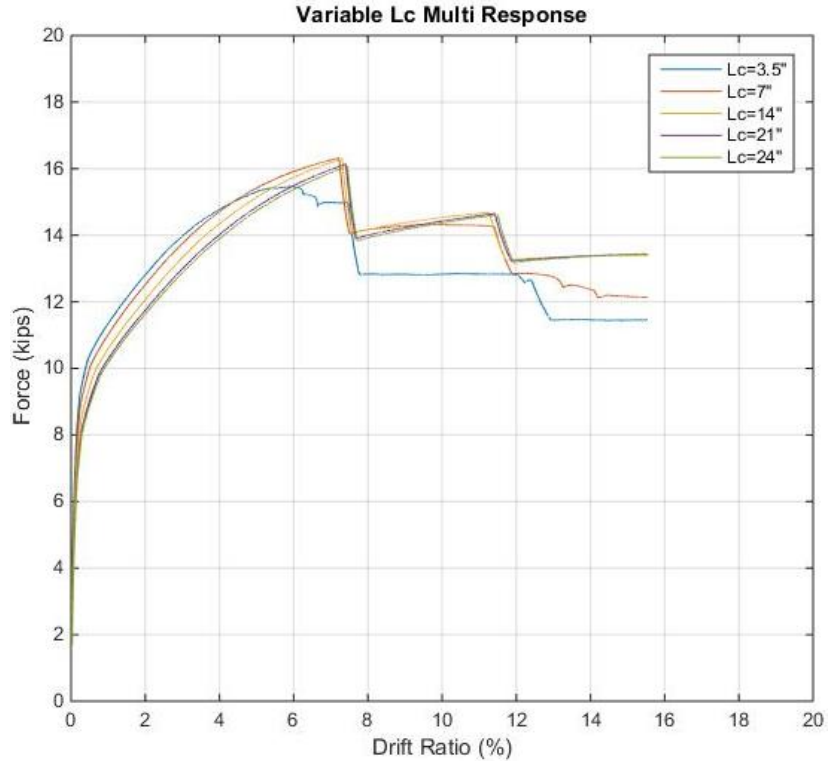
Figure 26 shows the responses of a varying lc

2.1.1.11. Monotonic Pushover Analysis

The pushover analysis was performed to provide insight into the column ductility capacity. For 80 contact springs and an effective spring length of 24 inches, the pushover was conducted by a monotonically increasing displacement applied at to the top of the column at a low rate of 0.004 in/sec to avoid dynamic effects. Figure 27 shows where the displacement application was applied for the pushover analysis. The base force was recorded in the rigid links in order to decrease the amount of recorders needed. This allowed the base force to be recorded in one element instead of summing up the base forces in the dissipators, tendons, and column. The lateral force vs. drift ratio curve is plotted in Figure 28. The plot shows distinctive drops in the lateral force at a drift ratio of 8 and 12 percent. The first drop comes from the far left dissipator fracturing and the second drop comes from the left central dissipator fracturing. The material responses from the multicolumn pushover can be found in Appendix II.
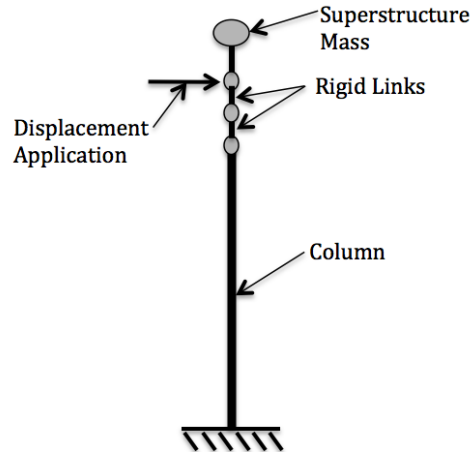
Figure 27. Location of the displacement application
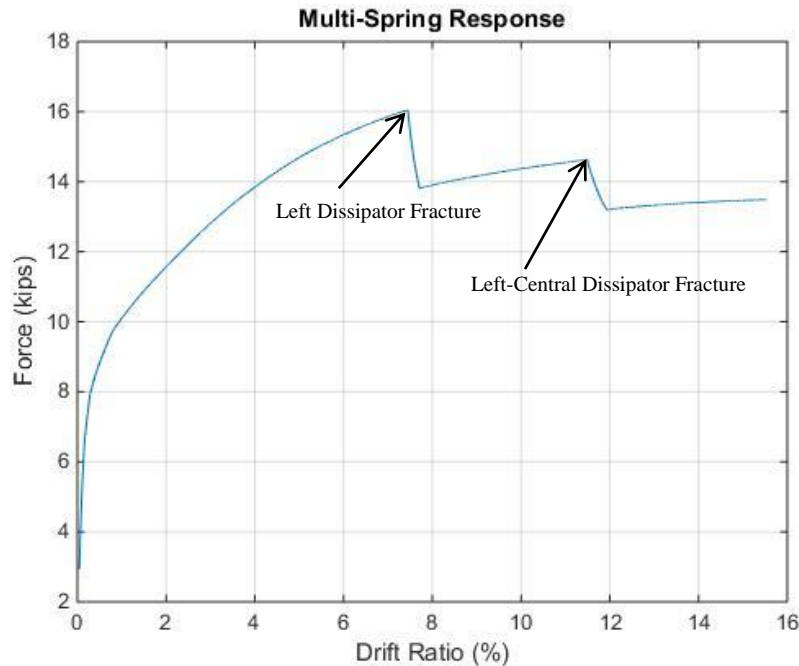
Figure 28. Lateral force versus drift ratio response

2.1.1.12. Comparison with Experimental data

Quasi-static cyclic loading was applied to the multi-spring model and compared to an experimental quasi-static cyclic response that was ran by Marriott et al (2009). The experimental data from that study are shown in Figure 29. The comparison between our model and these

experimental data is shown in Figure 30. The cyclic responses for the dissipators, cover concrete, confined concrete, and reinforcing steel can be found in Appendix II.

(a) Lateral Response   (b) Post-Tensioned Tendon Response
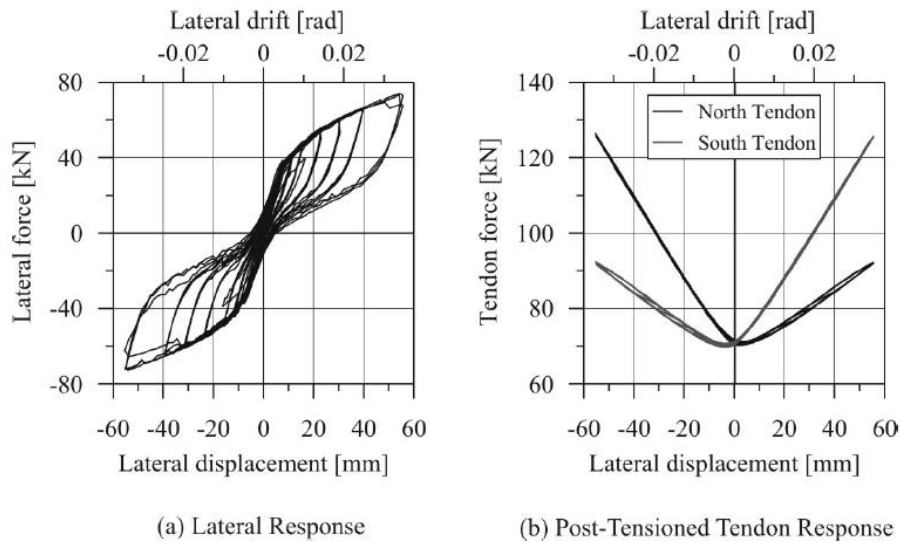
Figure 29. Data from cyclic testing by Marriot et al. (2009)
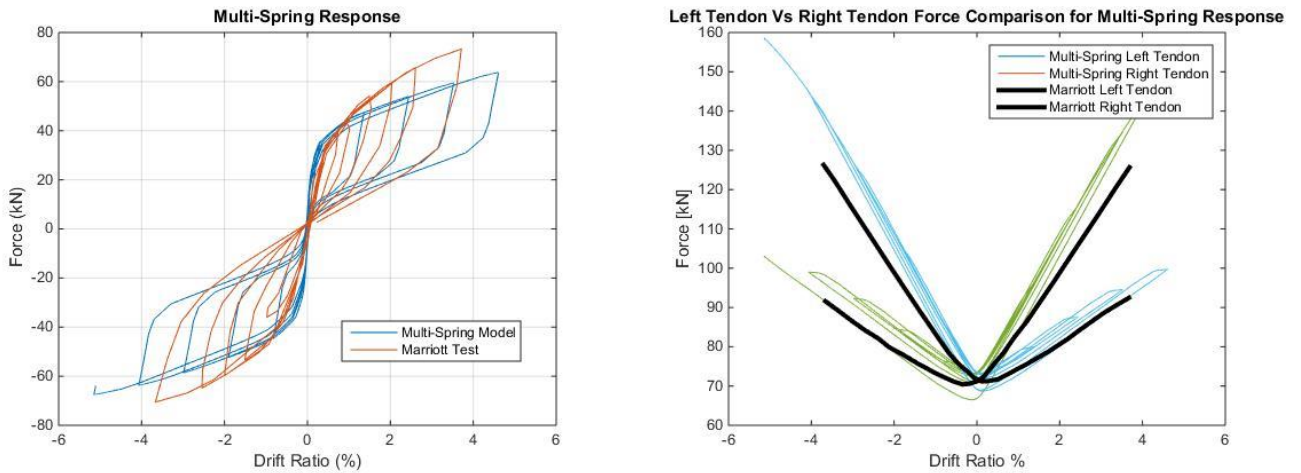
Figure 30. Comparison between Multi-Spring model and Marriott's Experimental Results

2.1.1.13. Parametric Studies on Design Parameters

The reference model for the parametric study on the column design parameters included the effective spring length of 24 inches and 80 contact springs. The design parameters that were studied included the initial post-tensioning load and the yielding strength of the energy dissipators.

Effect of initial post-tensioning

The column response to various post-tensioning forces was investigated. The post-tensioning force varied from ±20% and ±40%, similar to (Sideris, 2015). The corresponding lateral force vs. displacement curves are presented in Figure 31. It can be shown that increasing the PT force ratio results in greater lateral strength. With an increase of the post-tensioning force, the tendons will begin to yield earlier. Therefore, it is suggested to choose a PT force ratio that gives a value close to the peak lateral strength and yielding at large drift ratios.

The cyclic response for varying post-tensioning forces can be found in Appendix II. The cyclic response looks at drift ratios of ±4%.
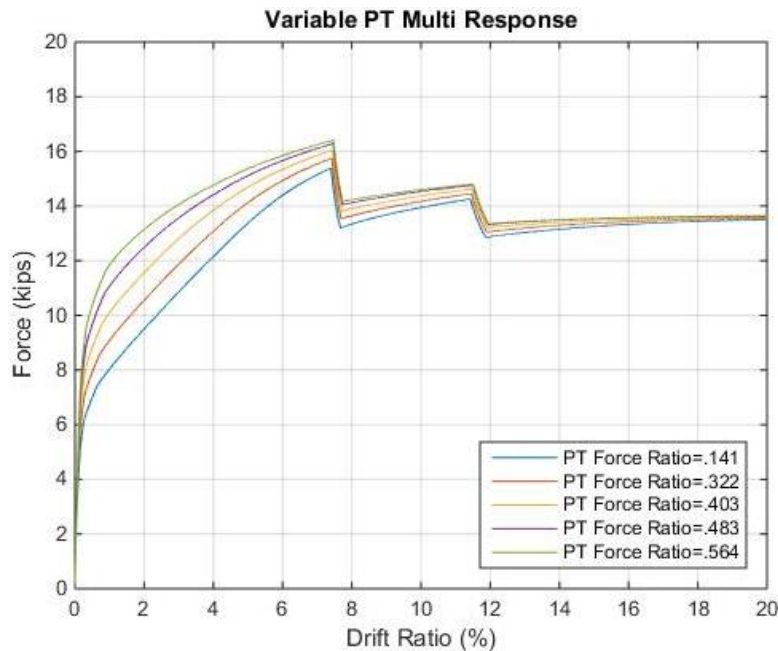
Figure 31 Lateral force versus displacement response for varying PT forces

Effect of varying dissipator yield strength

The columns response to varying yield strength of the energy dissipators was investigated. The yield strength of the energy dissipators varied from 46.4ksi (value used by Marriott) to more common steel yield strengths of 36ksi, 50ksi and 60ksi. The corresponding lateral force vs. displacement curves are presented in Figure 32 . It can be shown the increasing the yield strength in the dissipator will result in greater lateral strength

The cyclic response for varying post-tensioning forces can be found in Appendix II. The cyclic response shows drift ratios of ±4%.
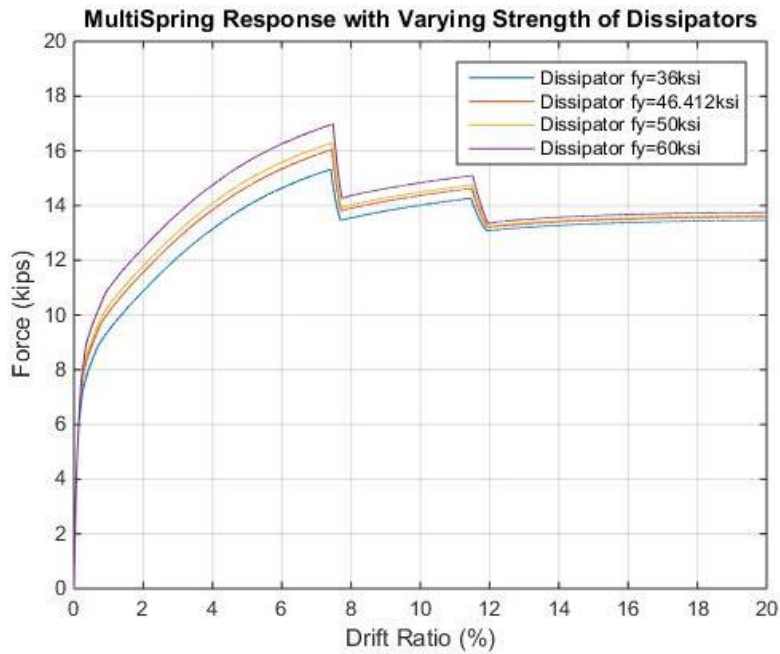
Figure 32. Lateral forces versus displacement response for varying dissipator yield strengths

2.2. Continuous HSR Joint Modeling

2.2.1. Implementation for Column by Marriott

The second concept that was implemented in the rocking system was the HSRjoint element. The HSRjoint simplifies modeling of rocking columns because the rocking interface is modeled by a single element (see Figure 33) instead of multiple contact springs.
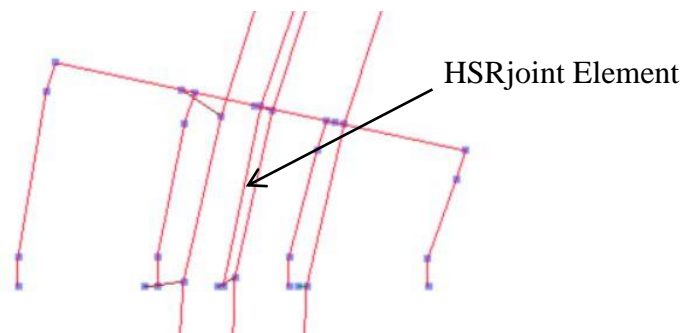
Figure 33 shows the single element HSRjoint contact

This element is a force-based formulation that satisfies force-equilibrium along the element length. A parameter used in this formulation is the number of integration points taken along the element. A minimum of 3 integration points is required for the element to run. This is typical for elements with shorter lengths. The number of integration points must satisfy the following equations:

$$\frac{l_c}{\Delta x} \geq 2 \quad \text{and} \quad \Delta x = \frac{L}{N-1} \tag{8}$$

where N is the number of integration points, L is the element length, and l_c is the equivalent plastic hinge length due to rocking. Rearranging the equation:

$$\frac{l_c}{L}(N-1) \geq 2 \qquad N \geq 1 + \frac{2L}{l_c} \tag{9}$$

The element also has separate sections that must be added which are the joint section (where the rocking occurs), bottom section, and top section. The bottom and top section are the same sections defined earlier in the report that have steel that can take both tension and compression. The joint section has longitudinal steel that can only take compression just like how the longitudinal reinforcement compression springs were formulated in the multi-spring rocking system. Since the steel cannot take tension, it allows the column to rock when it is acted on by an external lateral force. The element also has a few parameters that consider sliding. These parameters are the coefficient of friction at the joint interface, initial stiffness of friction hysteretic model, and secondary stiffness of friction hysteretic model (usually, very close to zero). Since the column is being analyzed as a rocking-only system, those parameters were set to high values to inhibit sliding. The major parameter that must be input in the HSRjoint element is the equivalent plastic hinge length, l_c. The materials, elements, loading, masses, gravity loads, and convergence criteria were all identical to those used for the model with the multi-spring contact area, but in the model with the HSRjoint element, the zero-length springs were removed and replaced with a single HSRjoint element, as shown in Figure 34.

SUPERSTRUCTURE MASS

RIGID LINK CONNECTING SUPERSTRUCTURE MASS TO TOP OF COLUMN

RIGID LINKS CONNECTING TOP OF POST-TENSIONED TENDONS & REINFORCED CONCRETE COLUMN

COROTTRUSS ELEMENTS (POST-TENSIONED TENDONS) CENTRAL TENDON IS OFFSET FOR VISUAL EFFECT

53" TENDON EFFECTIVE LENGTH

FORCEBEAM COLUMN ELEMENTS W/ FIBER SECTION (REINFORCED CONCRETE COLUMN)

ELASTICMULTILINEAR ELEMENTS CONSTRAING TENDON INSIDE DUCT

NODES THAT CONNECT MASSES
(RIGID LINK ELASTIC BEAMCOLUMN ELEMENTS)

NODES THAT CONNECT DISSAPATORS
(TRUSS & ELASTICBEAMCOLUMN ELEMENTS)

NODES THAT CONNECT COLUMN ELEMENTS
(FORCE BEAM COLUMN ELEMENTS)

NODES THAT CONNECT TENDONS
(COROT TRUSS ELEMENTS)

NODE CONSTRAINING TENDON INSIDE DUCT
(ELASTICMULTILINEAR ELEMENT)

RIGID LINKS CONNECTING DISSIPATORS TO REINFORCED CONCRETE COLUMN

ELASTIC BEAM COLUMN ELEMENTS (THICKER PART OF WISHBONE SHAPE)

HSR ELEMENT USED TO SIMULATE THE ROCKING SYSTEM

TRUSS ELEMENTS (THINNER FUSE MEMBER THAT YIELDS)

BASE OF COLUMN. CENTRAL TENDON IS CENTERED IN COLUMN BUT OFFSET FOR VISUAL EFFECT

MARRIOTT COLUMN: MODELING APPROACH: HSRJOINT ELEMENT ROCKING

Figure 34 HSRjoint Model

2.2.1.1. Parametric Studies on Model Parameters

The equivalent plastic hinge length at rocking (l_c) was an important model parameter to examine, because it can affect the predicted response considerably. A parametric study was performed to see how varying values for the victual plasticity spreading affected the predicted response. The typical values for l_c are usually 80% to 100% of the cross-section depth of the column. The column from Marriot et al had a cross-section 14x14 in^2. The results for various values of l_c are shown in Figure 35. As shown, the response does not change much for a plastic hinge length larger than the cross-section depth.
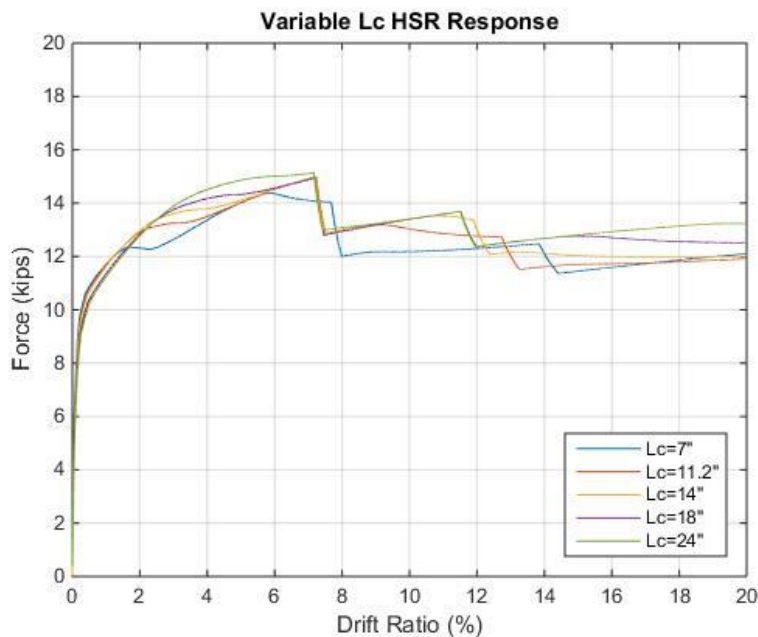
Figure 35 shows the effect Lc has on the columns response

2.2.1.2. Pushover Analysis

The same pushover analysis performed in section 2.1.1.11 was performed on the HSRjoint contact column as shown in Figure 36.
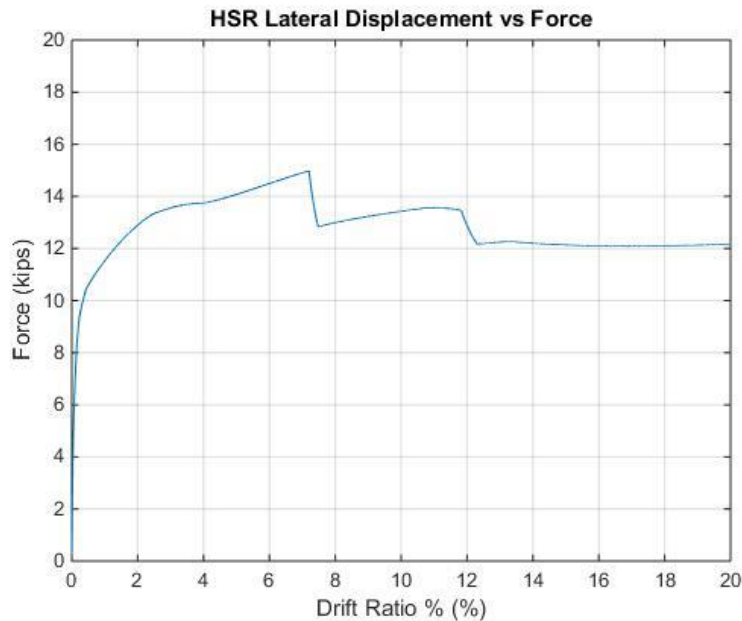
Figure 36 Lateral Force versus Displacement

2.2.1.3. Comparison with Experimental Data

Quasi-static cyclic loading was applied to the column model with HSRjoint element and the response was compared to the experimental data by Marriott et al (2009). Marriott et al's lateral force vs. displacement response and total PT force vs. lateral displacement response is shown in . The comparison between the HSRjoint model and Marriot's experimental data is shown in Figure 37. The cyclic responses for the dissipators, cover concrete, confined concrete, and reinforcing steel can be found in Appendix III
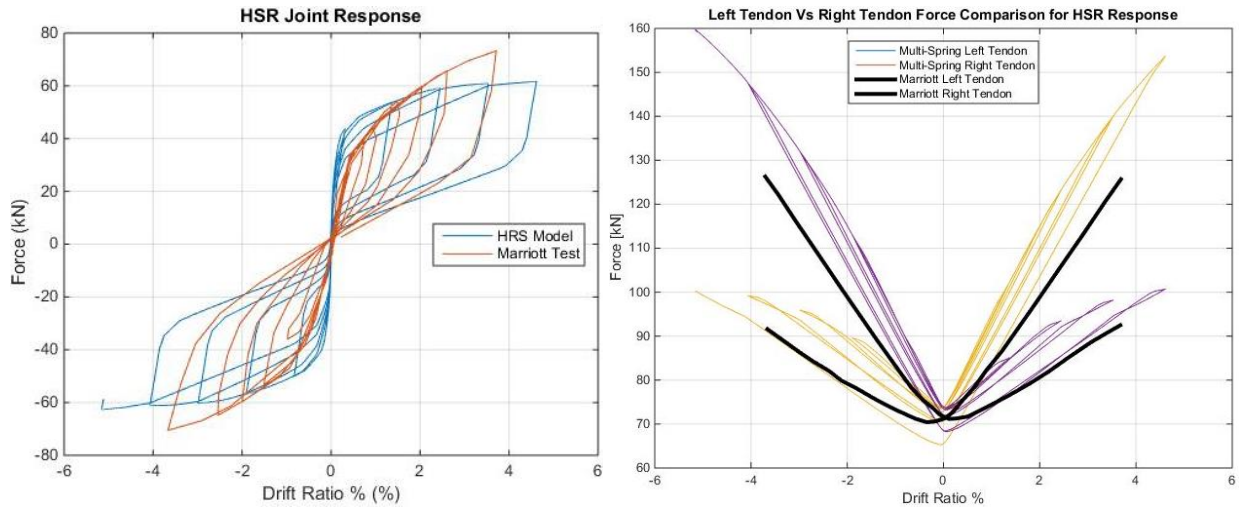
Figure 37 HSR Model versus Marriott Experimental Data

2.2.1.4. Parametric Studies on Design Parameters

The reference model for the design parameter parametric study included a plastic hinge length equal to the diameter. The design parameters that were studied were the initial post-tensioning load and the yielding strength of the energy dissipators. The application of the displacement and the materials were the same as before.

<u>Effect of initial post-tensioning</u>

The column's response to varying post-tensioning forces was investigated. The post-tensioning force varied from ±20% and ±40%, similar to (Sideris, 2015). The corresponding lateral force vs. displacement curves are presented in Figure 38. It is observed that increasing the PT force ratio results in greater lateral strength. Also, increasing the initial post-tensioning force results in early yielding of the tendons.

The cyclic response for varying post-tensioning forces can be found in Appendix III. The cyclic response looks at drift ratios of ±4%.
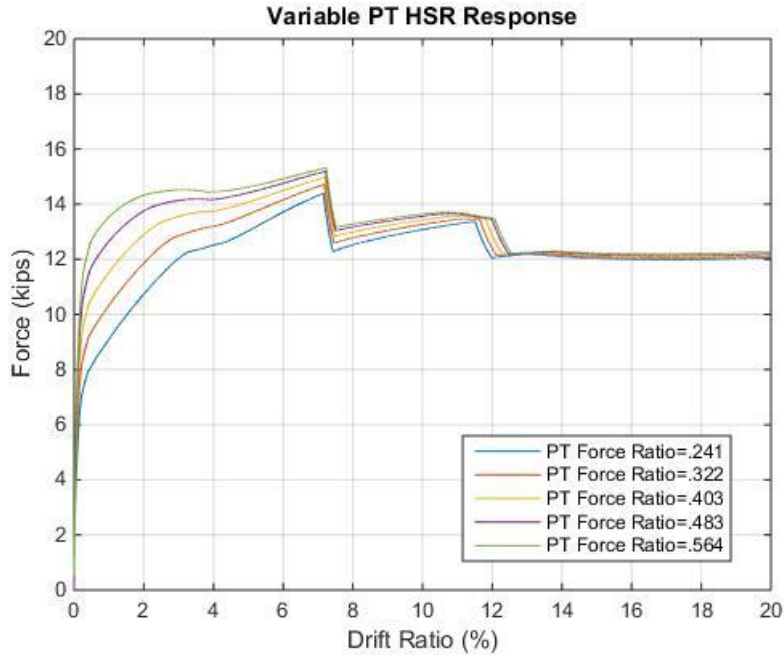
Figure 38 Lateral Force versus Drift Ratio Response of varying initial post-tensioning

<u>Effect of yield strength of the dissipator</u>

The columns response to various yield strengths of the energy dissipators is investigated. The following yield strengths were considered; 36 ksi, 46.4 ksi (value used by Marriott), 50 ksi and 60 ksi. The corresponding lateral force vs. displacement curves are presented in Figure 39. It can be shown the increasing the yield strength in the dissipator will result in greater lateral strength

The cyclic response for varying post-tensioning forces can be found in Appendix III. The cyclic response looks at drift ratios of ±4%.
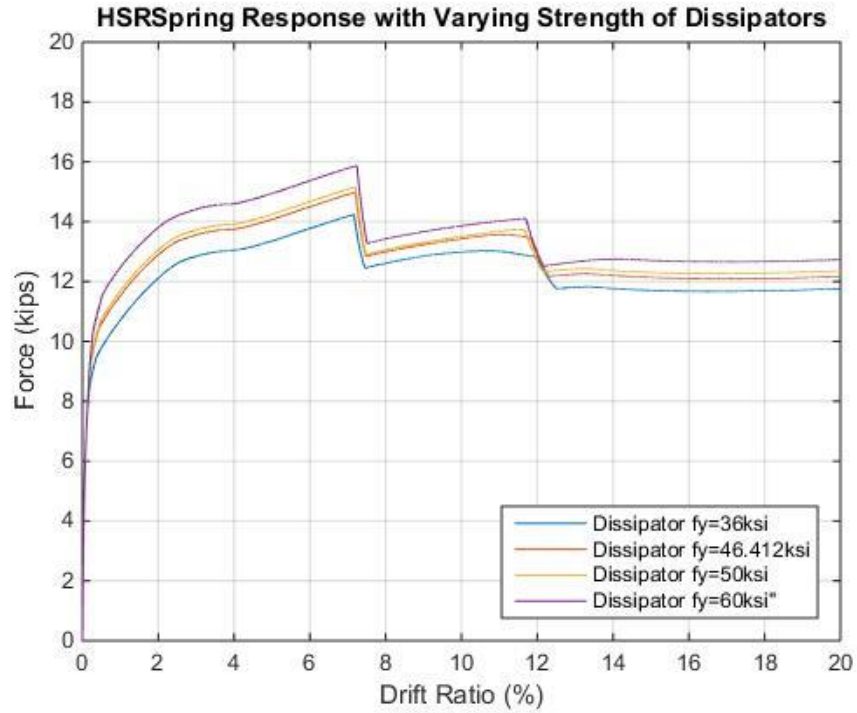
Figure 39 Lateral Force versus Drift Ratio with varying Dissipator Yield Strengths

2.2.2. Implementation for Column by Sideris

2.2.2.1. Model Description

A model using the HSRjoint element was created for the HSR bridge pier tested at the University at Buffalo – SUNY (Sideris, 2012). The test specimen was a scaled down (1:2.39) version of the prototype structure considered by (Megally,, Garg, Seible , & Dowell, 2002). The prototype structure is shown in Figure 40. The experimental specimen was a single cell box girder precast concrete segmental bridge. The superstructure had a longitudinal length of 61.875ft with pier-to-pier distance of 41.875ft. The pier height (which included the cap beam but not the superstructure deck) was 11.875ft, as shown in Figure 41.
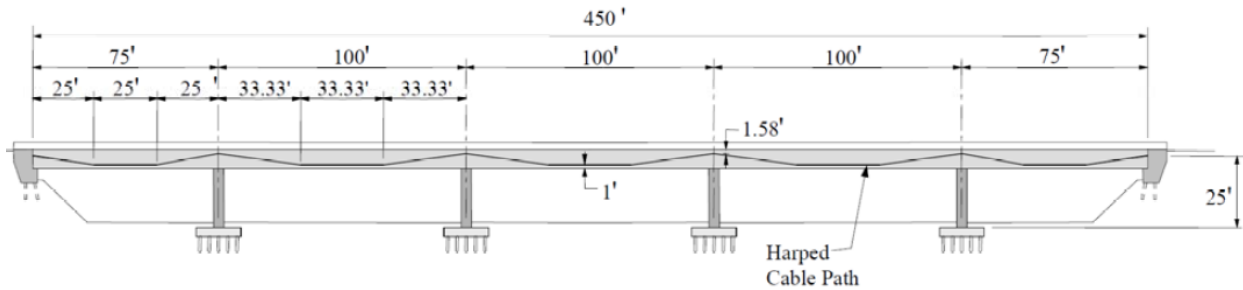
Figure 40 Prototype bridge (From Megally,, et al., 2002)
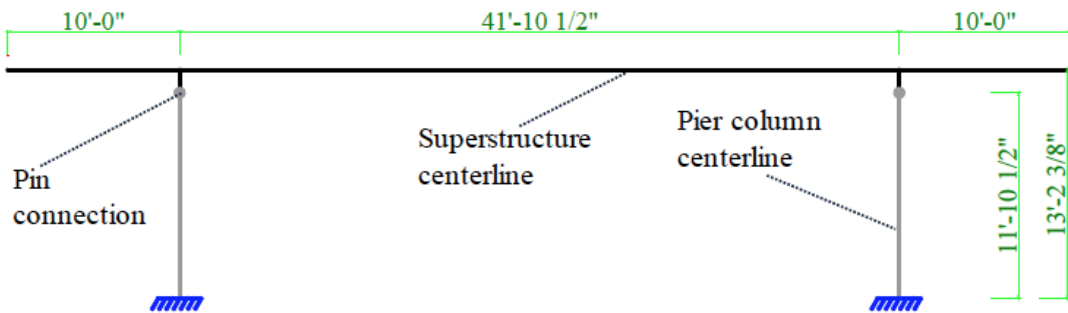
Figure 41 Specimen Model. (Model Domain) From Sideris, 2012

The elevation view of the specimen structure consisted of the bridge pier (five segments), cap beam, and the superstructure, as shown in the Figure 42. The column had eight 0.6"-diameter post-tensioning tendons that were anchored in the foundation and the top of the cap beam. They are placed in the ducts that run through the bridge pier, as shown in the cross section of the bridge pier in Figure 42. Each tendon was initially post-tensioned to 20kips. The 61'-10½" superstructure rested on the cap beam was supported by two bridge piers. The overall weight of the superstructure is split between the two bridge piers and calculated to be 44 kips per pier. The weight of the cap beam is calculated to be 3.65 kips.

The model created in this study focused on the response of the bridge in the transverse direction. For this reason, half of the bridge was modeled, including one of the two piers. This study solely focused on the rocking response; hence sliding was neglected/restrained.
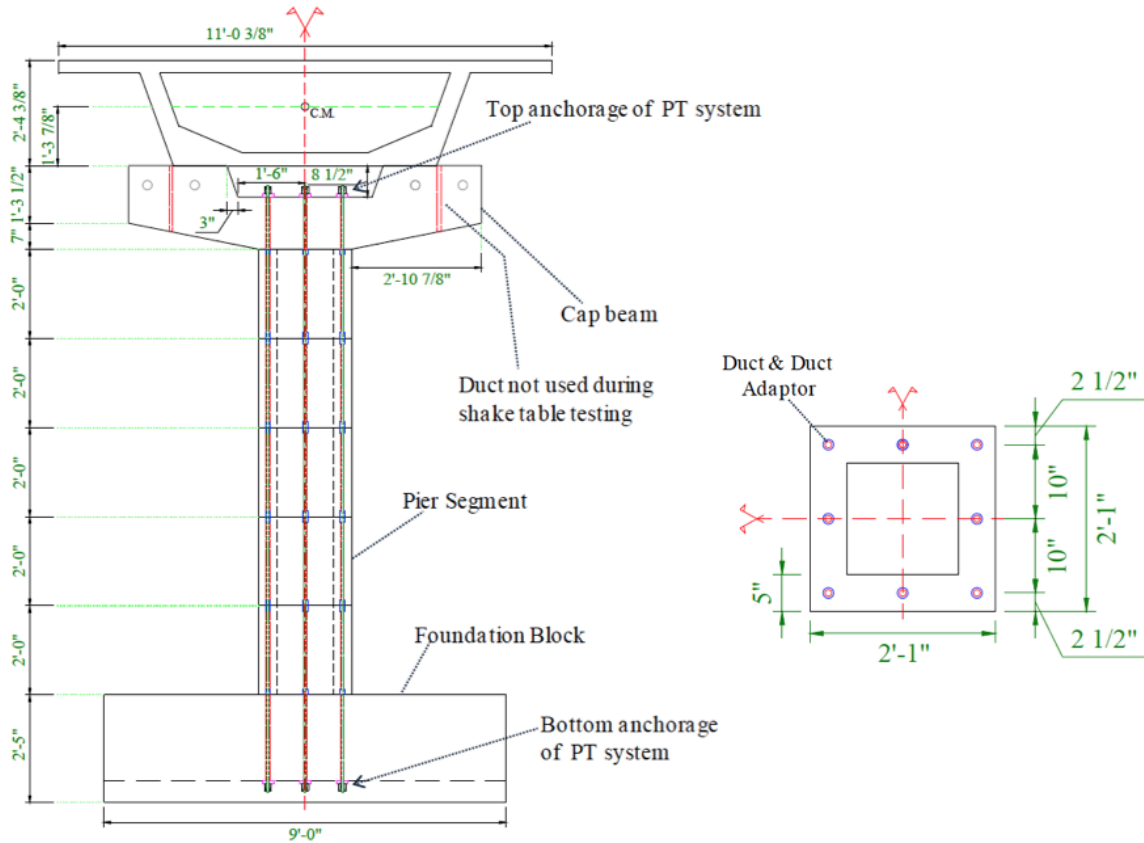
Figure 42 Elevation view of specimen structure and cross section of bridge pier, (Sideris, 2012)

2.2.2.2. Materials

Concrete

As stated in section 2.1.1.4, it is important to model the concrete with two separate strengths. The cover concrete (unconfined concrete) can be modeled to replicate the cylinder concrete compression tests; however the confined concrete, or the concrete incased inside the confining hoops must be modeled separately.

Unconfined Concrete

For the unconfined cover concrete the OpenSees material Concrete01 was used. Concrete01 is a material with degraded linear unloading/reloading stiffness with no tensile strength. Concrete01 has four parameters that must be inputted which are the 28-day compressive strength (f_c'), the strain at maximum strength (ε_0), the strength at crushing, and the strain at crushing (spalling ε_{sp}). For the cover concrete the maximum compressive strength f'_c is given as 5000psi and the strain

at maximum strength is assumed to be .002. The strength at crushing is taken as 5000psi/1000 and the strain at crushing is taken as .008.

Confined Concrete

For the confined concrete the OpenSees material Concrete01 was also used. For the concrete confined inside the reinforcing bars the maximum compressive strength f'_c was found to be 6000psi using the same equations defined in 2.1.1.4. The strain at maximum strength was found to be 0.004. The compressive strength at crushing was found to be 3700psi with a crushing strain of 0.02.

The separate materials were defined in a fiber section. Since the columns cross section is hollow there was cover concrete on the inside face and the outside face as shown in Figure 43
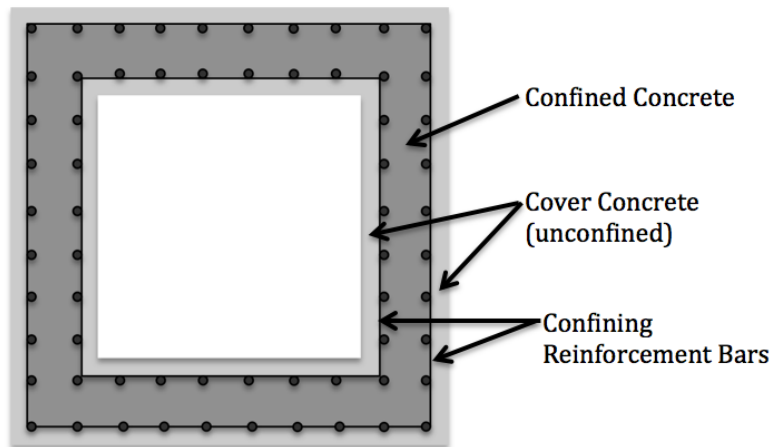
Figure 43. Cross-section regions of confined and unconfined concrete

Reinforcing Steel

The mild steel used for the longitudinal reinforcement had a modulus of elasticity of 29,000ksi and yield strength of 60ksi. To model this material, the bilinear damage model, *BilinDamage*, described earlier was used. The selected input properties are shown in Table 7

Table 7 Longitudinal and Confining Steel Properties for *BilinDamage* model

Longitudinal Reinforcement & Confining Steel Reinforcment		
Modulus of Elasticity, E	29000	ksi
Yield Strain, f_y	60	ksi
Strain Hardening Ratio r_y	0.10%	
eps1	0.2	
eps2	0.21	
rfmin	0.001	

Tendons

The tendons used were seven-wire strands that had a nominal diameter of 0.6 in. The seven-wire monostrands conformed to Gr. 270-ASTM A416. The tendon material has a modulus of elasticity of 28500 ksi with a yield stress of 243 ksi. Similarly to the approach followed in section 2.1.1.4 and 2.1.1.5, the tendon was modeled wire by wire over a length of 53 inches, in accordance with the test data by by (Sideris, Aref, & Filiatrault, 2014). The selected fracture strains for the 0.6"-diameter monostrand are shown in Table 8. The *PTSteel* material model, described earlier, was used. The material properties of the tendon that were parameters for the PTSteel material are shown in Table 9.

Table 8 Individual wire fracture strains

Monostrand diameter	Fractured wire						
	1st	2nd	3rd	4th	5th	6th	7th
0.5 in.	0.0293	0.0359	0.0393	0.0437	0.0584	0.0596	0.0925
0.6 in.	0.0241	0.0371	0.0450	0.0527	0.0598	0.0695	0.0908

Note: 1 in. = 25.4 mm.

Table 9 Properties of 0.6in Tendon

Property	0.6in monostrand
A_{PT} ,in^2 Area of Tendon	0.217
E_{PT} ,ksi Elastic modulus of unbonded monostrand	28,500
f_{py} Nominal yield force of monostrand	243
K, Actual yield stress to nominal yield stress of a mono	1.045
rPT Post-eleastic over elastic modulus of a monostran	0.015
R, Smoothness Factor	5

2.2.2.3. Element and Node Recorders

The element and node recorders were set up the same as in previous sections expect for the cross section had different recorders due to the hollow cross section. The recorders for the cross section are shown in Figure 44. An overall summary of the HSRjoint column is illustrated in Figure 45.
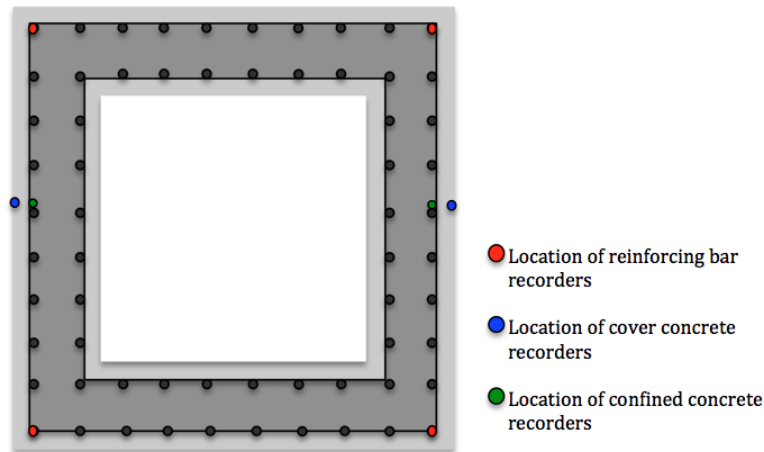
Figure 44 Location of Concrete and Reinforcing Steel Recorders
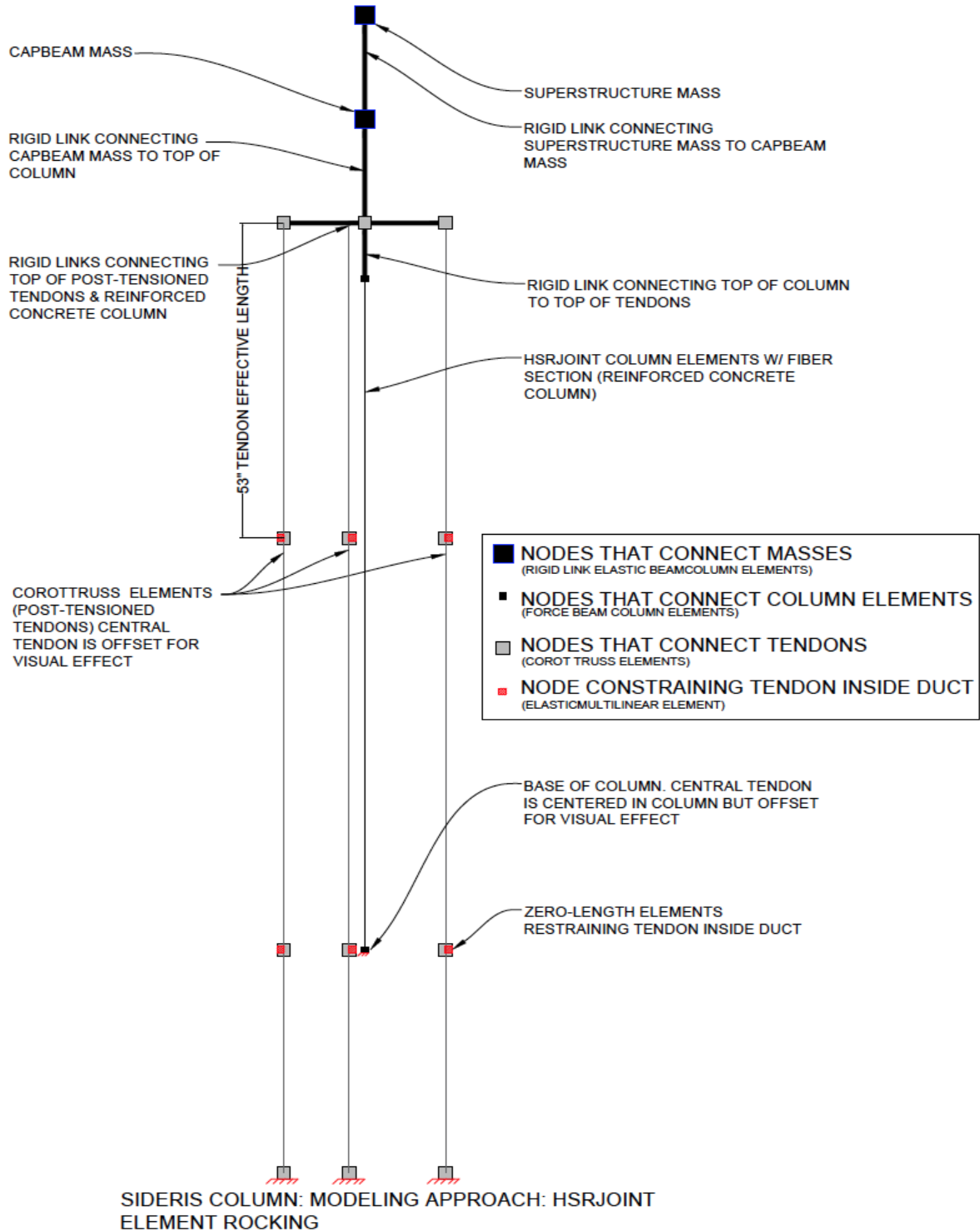
Figure 45 Overall Summary of HSRjoint Model

2.2.2.4. Parametric Study on Model Parameters

The equivalent plastic hinge length at rocking, l_c, was an important model parameter to examine because it can effect the results considerably. A parametric study was performed to see how varying values for l_c affect the predicted response. The typical values for l_c are usually 80% to 100% of the column cross-section depth. The column cross-section is 25"x25". The results of various values of l_c are shown in Figure 46 with a zoomed-in response shown in Figure 47. The impulsive responses in the pushover curves are generated because of the fracture of the tendon wires.
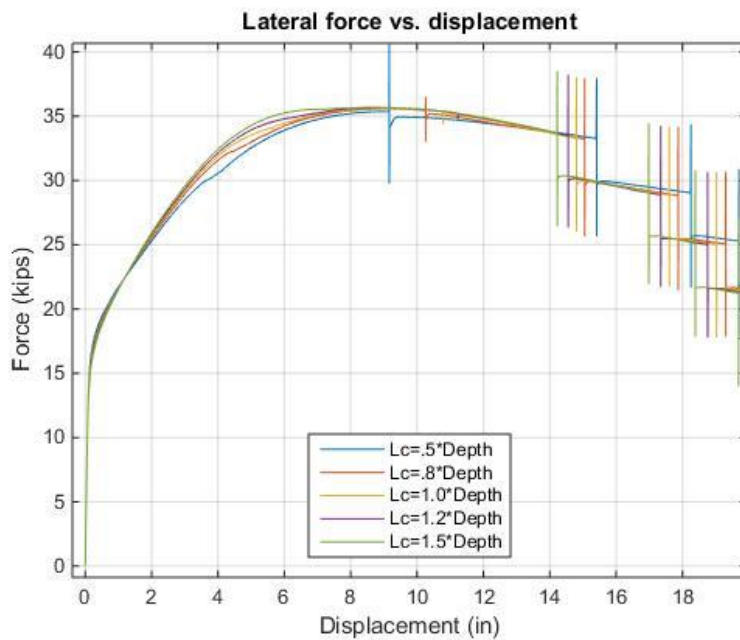
Figure 46 Effect l_c has on the columns response
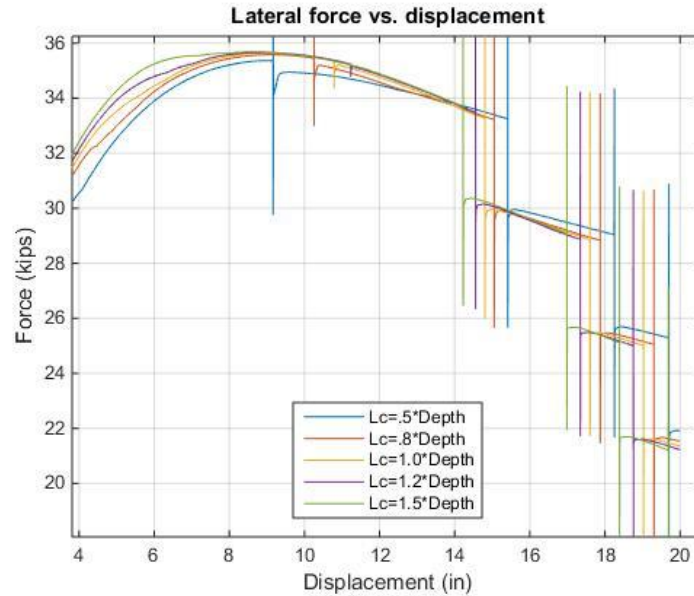
Figure 47 Effect of l_c has on the columns response (zoomed-in)

2.2.2.5. Parametric Study on Design Parameters

The reference model for the design parameter parametric study included a plastic hinge length equal to the cross-section depth of 25". The design parameters considered were the initial post-tensioning load and the gravity load. The application of the displacement and the materials were all kept constant.

Effect of initial post-tensioning

The columns response to varying post-tensioning forces was investigated. The post tensioned force varied from ±20%, similar to (Sideris, 2015). The corresponding lateral force vs. displacement curves are presented in Figure 48. It can be shown the increasing the PT force ratio will result in greater lateral strength, while increasing the initial post-tensioning force results in early yielding of the tendons.
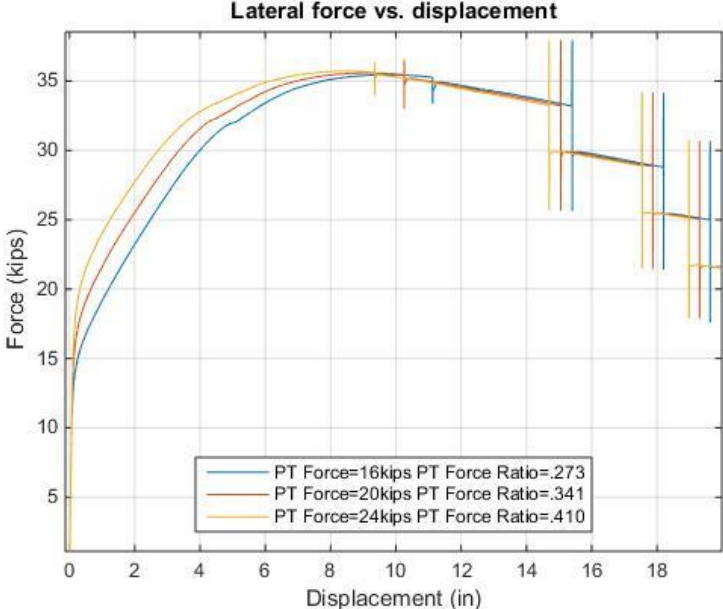
Figure 48 Lateral force versus displacement with varying initial Post-Tensioning

Effect of Gravity Load

The current gravity load being applied to the column is 44kips. This parametric study will look at the effects of varying the external vertical load by ±30%. The analysis was performed with three external vertical loads, which are: 31kips, 44kips, and 57kips. The peak strength for all three-pushover curves ranged from 34.9 to 36.1kips at a drift ratio of 7.5% or 9.1in displacement as shown in Figure 49.
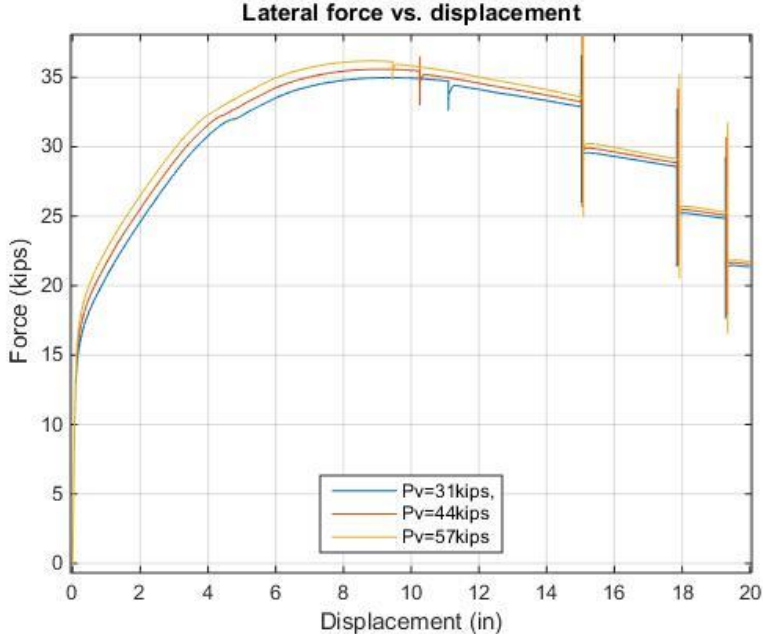
Figure 49 Lateral force vs displacement with varying external loads

3. PERFORMANCE ASSESSMENT OF BRIDGES WITH ROCKING COLUMNS

3.1. Introduction to Incremental Dynamic Analysis

Incremental dynamic analysis (IDA) was formalized by (Vamvatsikos & Cornell, 2002) as a means of assessing the performance of structures under seismic loading. The overall concept is to subject a structure to multiple earthquake ground motions under many different intensities. FEMA P695 provides far-field and near-fault ground motion sets (FEMA, 2009). These ground motion sets were selected by FEMA, based on the criteria shown in Figure 50. Note that no single ground motion meets all of the criteria establish in Figure 50, because of the limitations of available data.

IDA is crucial in the framework of Performance-based earthquake engineering (PBEE), which focuses on the estimation of the seismic demand and capacity of structures. IDA curves are plots of Damage Measures (DM); such as peak drift ratios or peak cover concrete strain vs. an Intensity Measure (IM), which is usually the spectral acceleration at the fundamental mode (Vamvatsikos & Cornell, 2005). Limit states (LS) are threshold values to the damage measures in reference to selected damage states. Typical damage states include life- safety and collapse prevention.

- **Code (*ASCE/SEI 7-05*) Consistent** – The records should be consistent (to the extent possible) with the ground motion requirements of Section 16.1.3.2 of ASCE/SEI 7-05 *Minimum Design Loads for Buildings and Other Structures* (ASCE, 2006a) for three-dimensional analysis of structures. In particular, "ground motions shall consist of pairs of appropriate horizontal ground motion acceleration components that shall be selected and scaled from individual recorded events."
- **Very Strong Ground Motions** – The records should represent very strong ground motions corresponding to the MCE motion. In high seismic regions where buildings are at greatest risk, few recorded ground motions are intense enough, and significant upward scaling of the records is often required.
- **Large Number of Records** – The number of records in the set should be "statistically" sufficient such that the results of collapse evaluations adequately describe both the median value and record-to-record (RTR) variability of collapse capacity.
- **Structure Type Independent** – Records should be broadly applicable to collapse evaluation of a variety of structural systems, such as systems that have different dynamic response properties or performance characteristics. Accordingly, records should not depend on period, or other building-specific properties of the structure.
- **Site Hazard Independent** – The records should be broadly applicable to collapse evaluation of structures located at different sites, such as sites with different ground motion hazard functions, site and source conditions. Accordingly, records should not depend on hazard de-aggregation, or other site- or hazard-dependent properties.

Figure 50 Criterion for FEMA-P695 Ground Motion Ensemble Selection (FEMA, 2009)

3.2. Model Dynamic Properties

The seismic mass for this model included the gravity load and the mass moment of inertia described earlier. Conducting Eigen analysis with OpenSEES, the natural period and the corresponding modeshapes are shown in Figure 51.
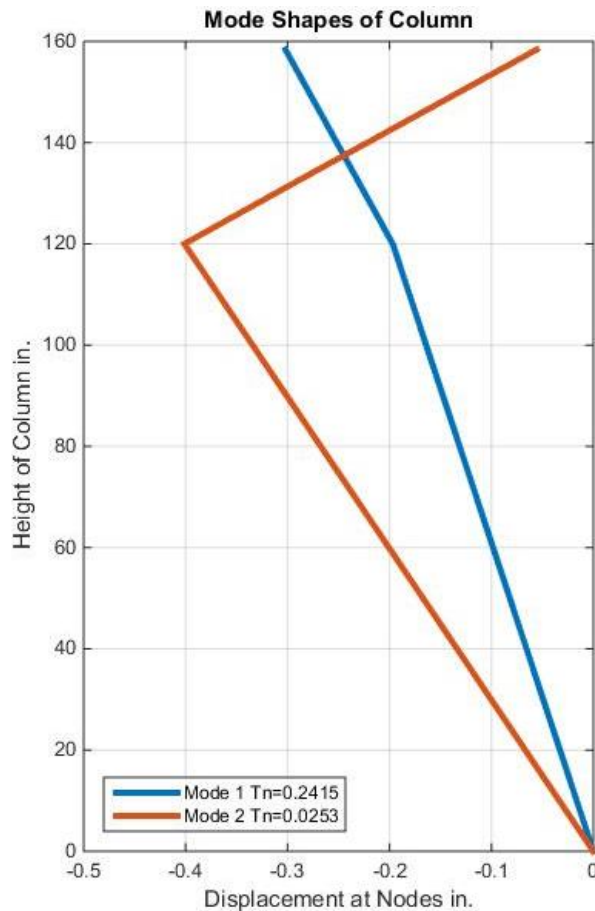
Figure 51 Mode Shapes of Column

3.3. Earthquake motions

As shown in Figure 50, certain criteria were used to create an ensemble of 22 far-field ground motions, which are shown in Table 10. Each ground motion has X, Y, and Z accelerations recorded. In this study, the X and Y motions were taken as separate earthquakes resulting in a total of 44 ground motions. However, some of the ground motions did not have vertical, Z, accelerations, therefore they were eliminated from the list and only 20 ground motions were used. The corresponding X & Y motions used the same vertical, Z-motions. The ground motions are

plotted in Figure 52. These ground motions are the exact motions downloaded from the PEER website without any scaling. These are the ground motions that would be applied to the prototype column.

Table 10 Far-Field Ground Motions

ID No.	Earthquake			Recording Station		Recorded Motions	
	Magnitude	Year	Name	Name	Owner	PGA_{max} (g)	PGV_{max} (cm/s)
1	6.7	1994	Northridge	Beverly Hills - Mulhol	USC	0.52	63
2	6.7	1994	Northridge	Canyon Country-WLC	USC	0.48	45
3	7.1	1999	Duzce, Turkey	Bolu	ERD	0.82	62
4	7.1	1999	Hector Mine	Hector	SCSN	0.34	42
5	6.5	1979	Imperial Valley	Delta	UNAMUCSD	0.35	33
6	6.5	1979	Imperial	El Centro Array #11	USGS	0.38	42
7	6.9	1995	Kobe, Japan	Nishi-Akashi	CUE	0.51	37
8	6.9	1995	Kobe, Japan	Shin-Osaka	CUE	0.24	38
9	7.5	1999	Kocaeli, Turkey	Duzce	ERD	0.36	59
10	7.5	1999	Kocaeli, Turkey	Arcelik	KOERI	0.22	40
11	7.3	1992	Landers	Yermo Fire Station	CDMG	0.24	52
12	7.3	1992	Landers	Coolwater	SCE	0.42	42
13	6.9	1989	Loma Prieta	Capitola	CDMG	0.53	35
14	6.9	1989	Loma Prieta	Gilroy Array #3	CDMG	0.56	45
15	7.4	1990	Manjil, Iran	Abbar	BHRC	0.51	54
16	6.5	1987	Superstition Hills	El Centro Imp. Co.	CDMG	0.36	46
17	6.5	1987	Superstition Hills	Poe Road (temp)	USGS	0.45	36
18	7	1992	Cape Mendocino	Rio Dell Overpass	CDMG	0.55	44
19	7.6	1999	Chi-Chi, Taiwan	CHY101	CWB	0.44	115
20	7.6	1999	Chi-Chi, Taiwan	TCU045	CWB	0.51	39
21	6.6	1971	San Fernando	LA - Hollywood Stor	CDMG	0.21	19
22	6.5	1976	Friuli, Italy	Tolmezzo	--	0.35	31
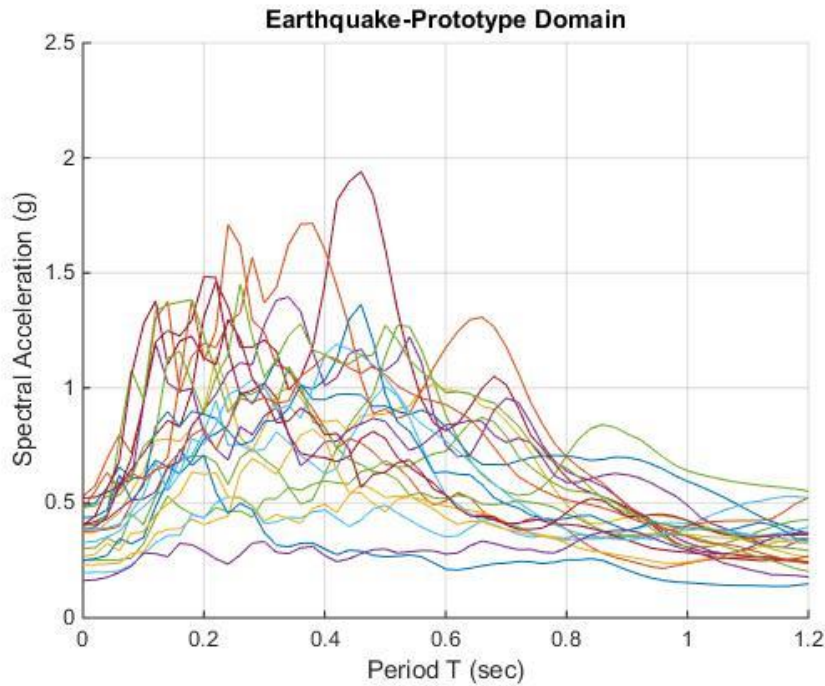
Figure 52 Far-Field Ground Motions

3.3.1. Similitude Analysis

Since the model being tested is a scaled down version of the prototype column, the ground motions and time step must be scaled as well. A similitude analysis establishes relationships between parameters measured in the prototype structure and a scaled down model. (Sideris, 2012). The scale factors are expressed by the following equation:

$$S_x = \frac{X_p}{X_m} \tag{10}$$

where S_X is the scale factor for the physical parameter X, p and m are subscripts referring to the prototype and model domain. The similitude analysis for all the column parameters is found in Table 11. Length (L), Force (F), and Time (T) are the quantities that are scaled in this similitude analysis. The scaling factor for the length is S_L=2.388. Since the model dimensions, model forces, and model masses were given the only values that need to be scaled in the dynamic analysis are the acceleration and time step of the earthquakes. The scaling factor for acceleration is 0.419. Therefore, all of the accelerations in the prototype domain are divided by 0.419 resulting in an increase of the spectral accelerations. The time is divided by 2.388 resulting in a smaller time step. The resultant ground motions are plotted in Figure 53. The spectral acceleration at the fundamental period, (SA(T1)), is an important value for the IDA. The IDA curves include the SA(T1) on the vertical axis versus the damage measure on the horizontal axis. The spectral acceleration at the fundamental period is shown in Figure 54.

Table 11 Scaling Factors for bridge specimen (Sideris, 2012)

Type	Quantity	Scale Factors	Values
Geometry	Length	S_L	2.39
	Displacement	S_L	2.39
	Area	S_L^2	5.71
	Volume	S_L^3	13.6
	Moment of Area	S_L^4	32.5
Dynamic Loading	Force	S_L^2	5.70
	Mass	S_L^3	13.6
	Acceleration	S_L^{-1}	0.419
	Time	S_L	2.39
	Velocity	1	1
	Natural Period	S_L	2.39
Material Properties	Stress	1	1
	Strain	1	1
	Elastic Modulus	$S_E(=1)$	1
	Mass density	$S_\rho(=1)$	1
Gravity-induced Loading and Material Properties	Weight (Force)	S_L^3	13.6
	Gravitational Acceleration	1	1
	Gravity-induced Stress	S_L	2.39
	Gravity-induced Strain	S_L	2.39
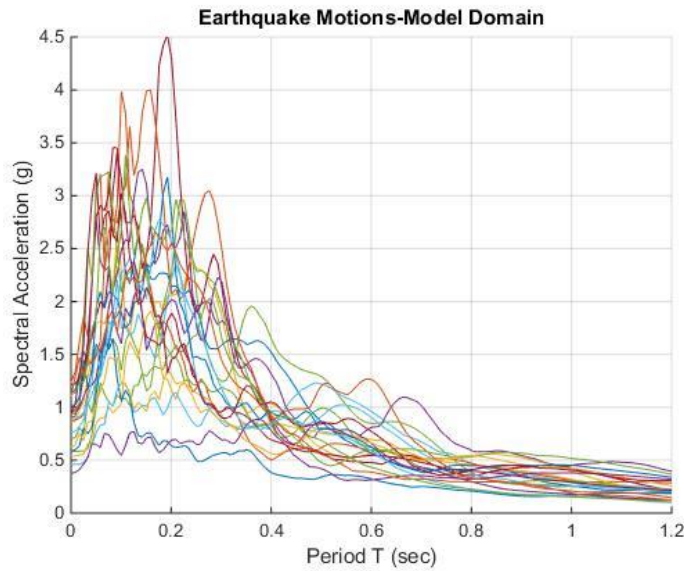
Figure 53 Earthquake Motions-Scaled to Model Domain
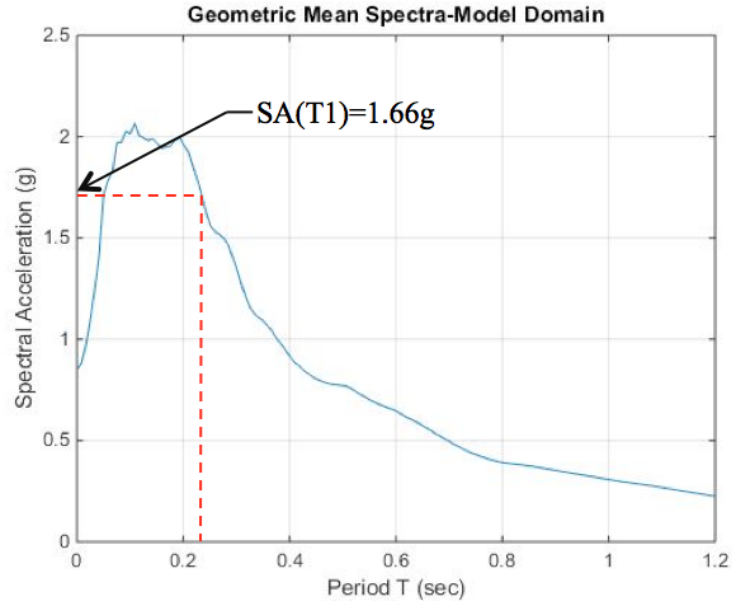
Figure 54 Geometric Mean Spectra in the Model Domain with SA(T₁) shown

3.3.2. Design Earthquake and Maximum Considered Earthquake

The geometric mean spectra is plotted versus the design earthquake and the maximum considered Earthquake as shown in Figure 55.
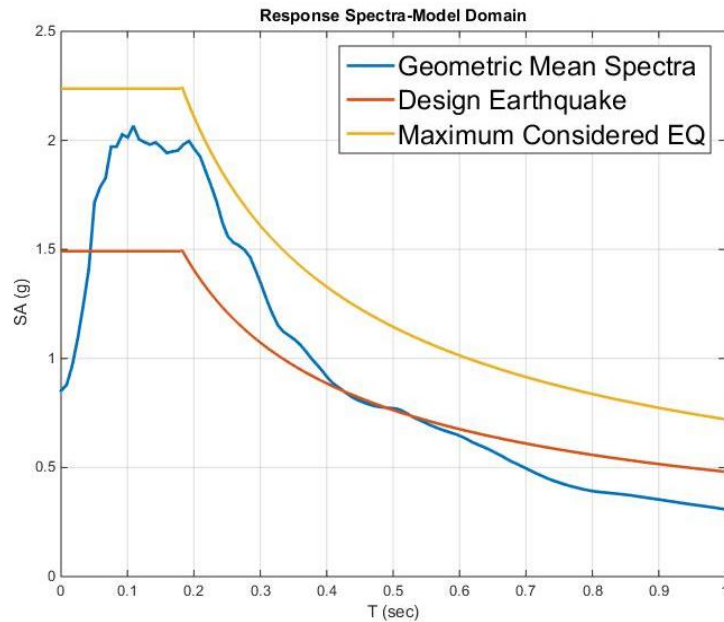
Figure 55 DE versus MCE versus Geometric Mean Spectra

3.4. Limit States

Damage Measures (DM), as introduced earlier, are structural parameters that are monitored throughout an IDA to rate the performance of the structure. Multiple DMs are monitored in this study. Each DM is considered a function of the Intensity Measure (IM). When it comes to PBEE, limit states (LS) for the selected DMs can be associated with of certain performance objectives, whether it be life safety or collapse prevention. In this study, we only consider limit states for collapse preventions, relating to tendon fracture, displacement at 80% of the peak strength in the post-peak range, confined concrete failure, and cover concrete spalling. The peak strength on the pushover curve is 26.5 kips. At 80% of the peak strength (21.2 kips) in the post-peak range, the drift ratio is 10%, which is considered to be the collapse drift ratio. The application of load for the pushover in Figure 56 is at the centroid of the superstructure; whereas, the pushovers for the parametric studies had an application of load much lower. This was because the pushovers in the parametric studies were compared to tests done by (Sideris, 2015) for validation. The pushover curve for the entire system must have an application of load at the superstructure mass for a more accurate representation of the dynamic analysis. All limit states are shown in Table 12.
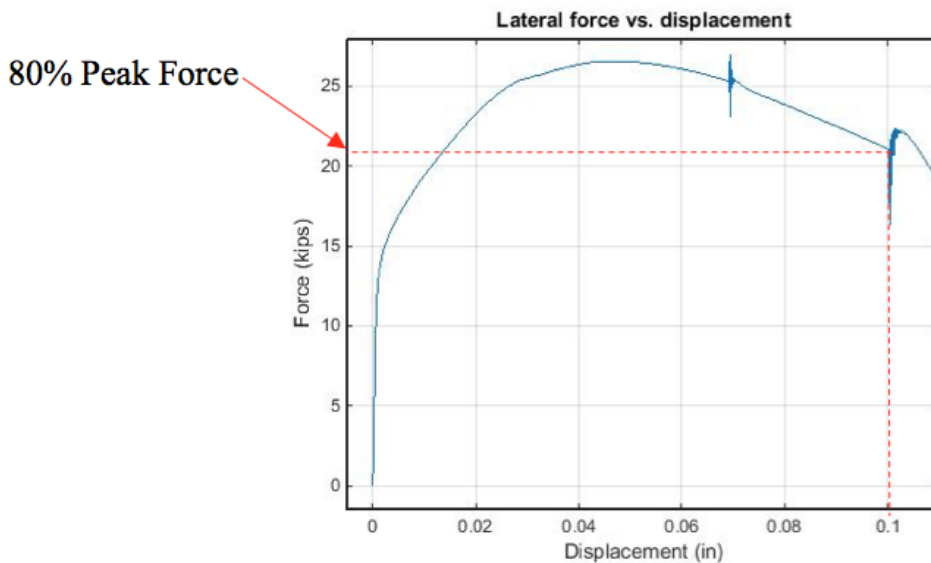
Figure 56 Collapse drift ratio

Table 12 Limit States

Damage Measure	Limit
Tendon Fracture	ε<.0241
Displacement at 80% residual strength	u<ucollapse drift<10.0%.
Unconfined Cover Concrete Strain	ε<.003
Confined Concrete Strain	ε<.0226

With these DMs and LSs defined, fragility curves can be determined through Incremental Dynamic Analysis. Fragility curves are given by the probability of a DM (engineering demand parameter), exceeding a certain LS under given IM, which can be calculated using equation (11):

$$P(DM > LS \mid IM) = \frac{N_{exceeded}(IM)}{N_{total}} \tag{11}$$

3.5. Incremental Dynamic Analysis

3.5.1. IDA with Lateral and Vertical Motions & 2.41% First Wire Tendon Fracture

The first incremental dynamic analysis was conducted with the model that considered sequential wire facture, with first wire tendon fracture at 2.41%. The following figures show the response of the peak displacement, residual displacement, and post-tensioning force/strain, cover concrete, and confined concrete.

(A)

(B)

(C)

(D)
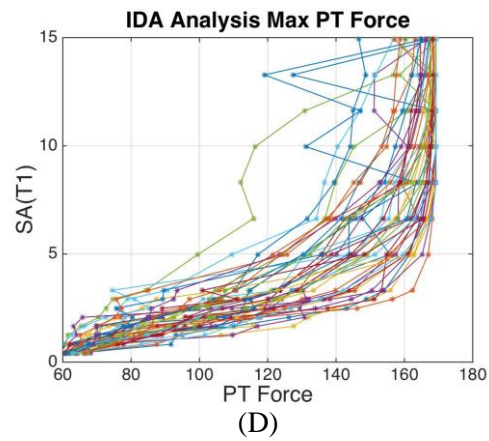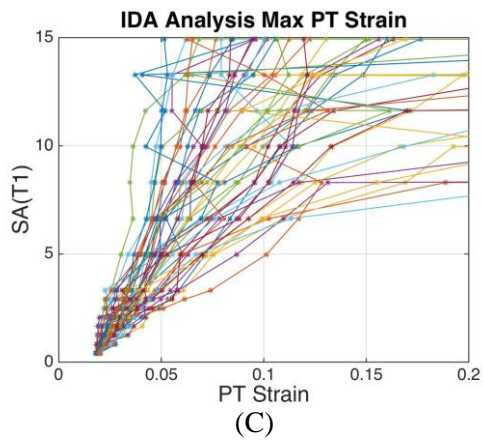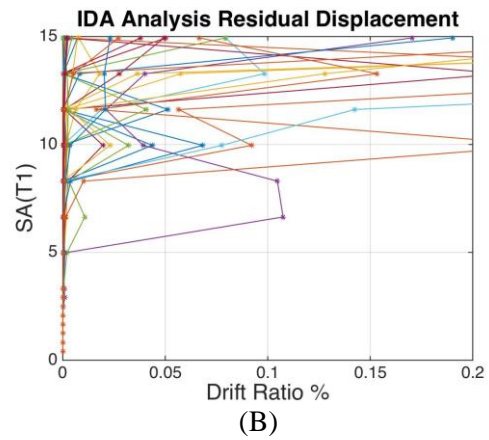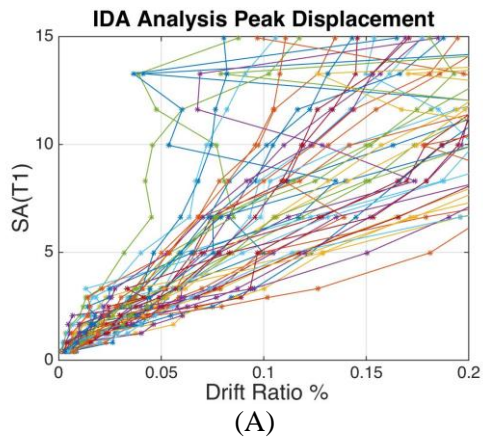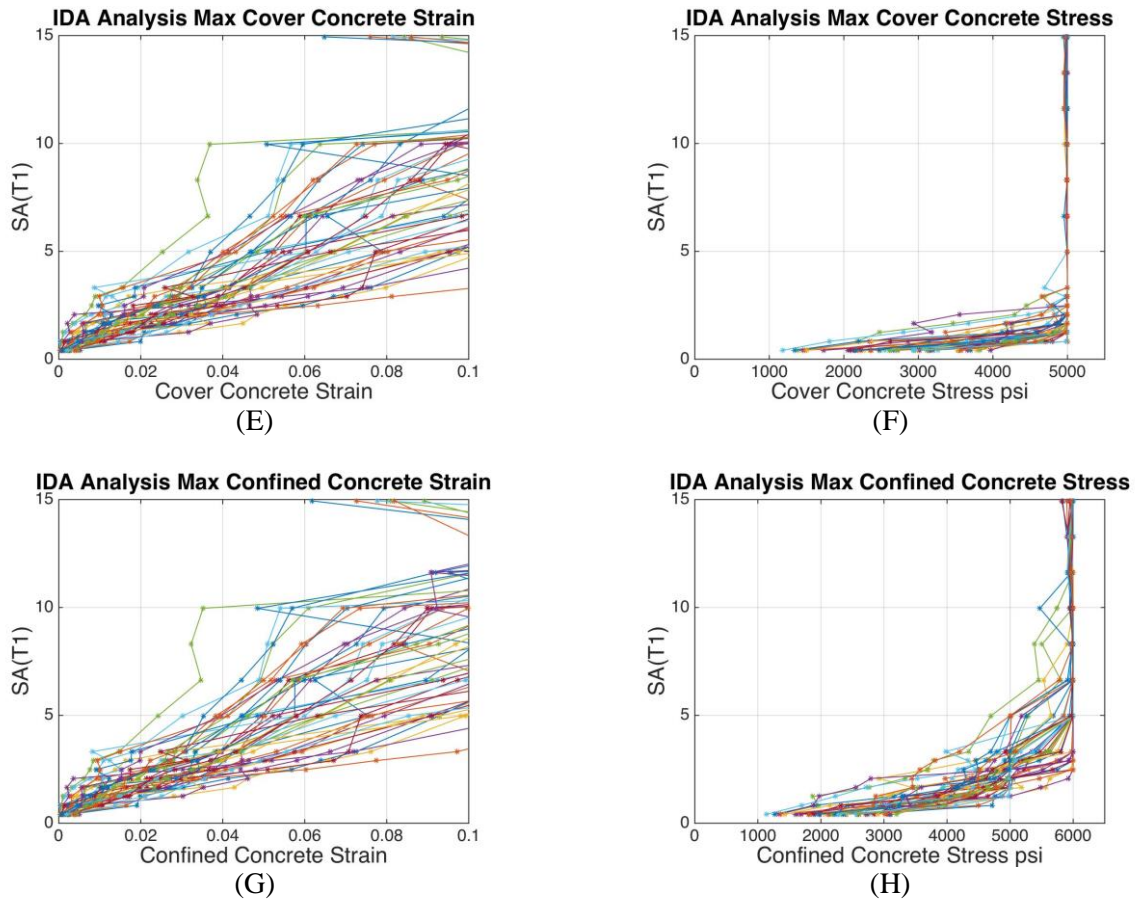
Figure 57 Incremental Dynamic Analysis for (A) Peak Displacement (B) Residual Displacement (C) PT Strain (D) PT Force (E) Cover Concrete Strain (F) Cover Concrete Stress (G) Confined Concrete Strain (H) Confined Concrete Stress

3.5.2. IDA with Lateral and Vertical Motions & 7.00% First Wire Tendon Fracture

The second incremental dynamic analysis was conducted with the model that considered simultaneous fracture of all tendon wires at 7.00% strain, which is a common design assumption. The following figures show the response of the peak displacement, residual displacement, post-tensioning force/strain, cover concrete, and confined concrete.

(A)

(B)

(C)

(D)

(E)

(F)

(G)

(H)
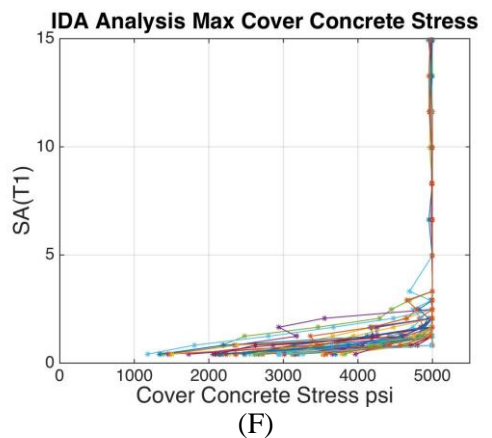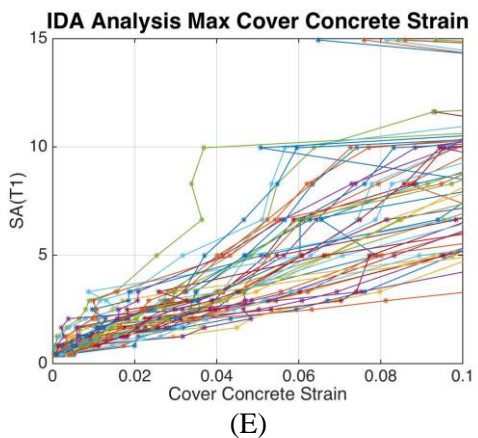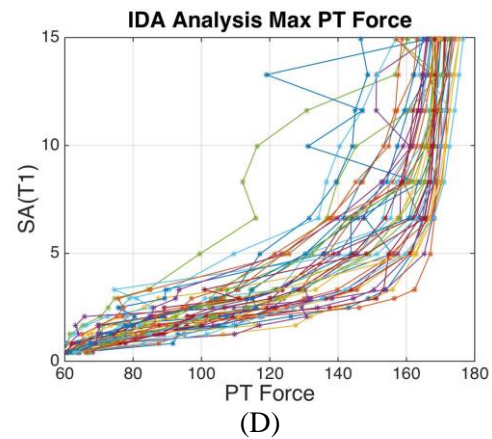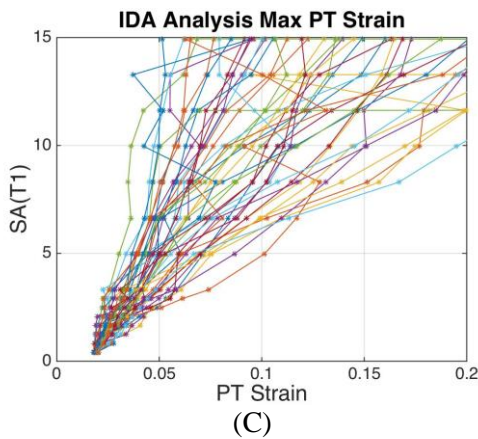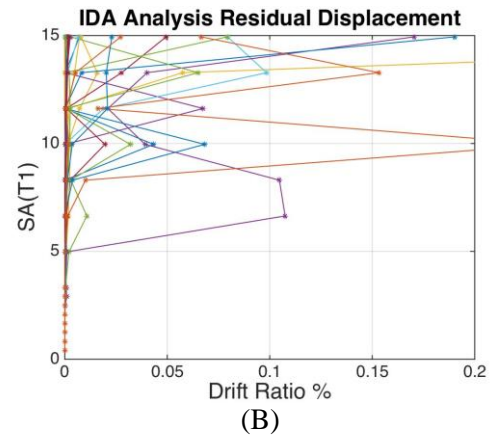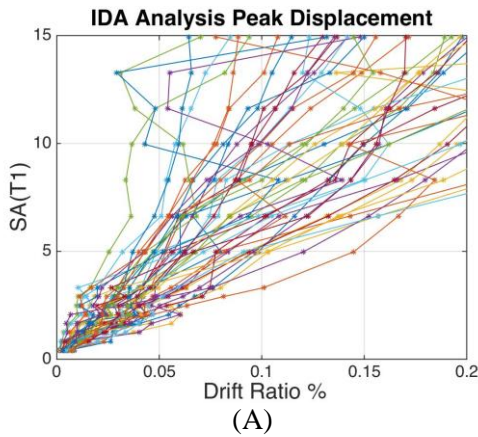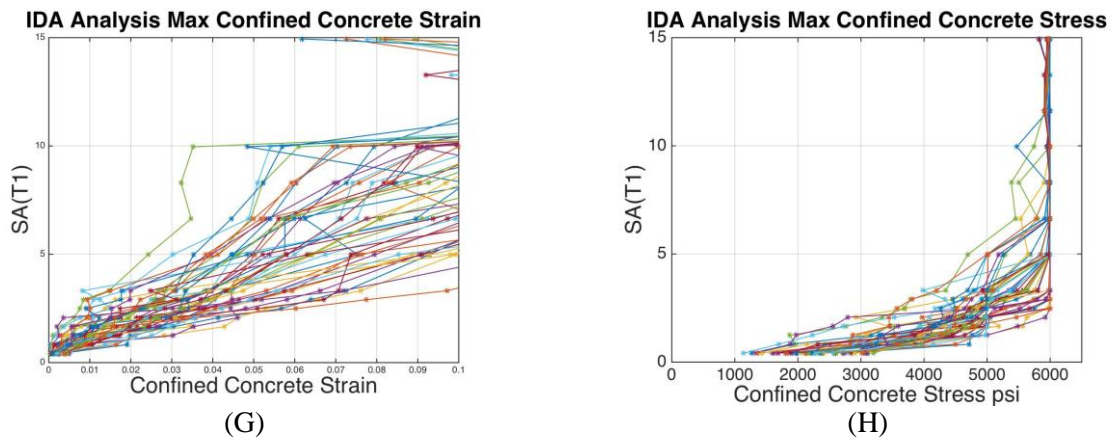
Figure 58 Incremental Dynamic Analysis for (A) Peak Displacement (B) Residual Displacement (C) PT Strain (D) PT Force (E) Cover Concrete Strain (F) Cover Concrete Stress (G) Confined Concrete Strain (H) Confined Concrete Stress

3.5.3. IDA Fragility Curve Comparison

Fragility curves were used to analyze the probability of certain DMs exceeding LSs representing the *collapse* damage state given a certain intensity measure for the two scenarios. The first scenario (Section 0) is when successive fracture occurred of the individual wires in the seven-wire strand tendon. The wires fracture at strains ranging from 2.41% to 9.08% as shown in Table 8. The second scenario (Section 0) is when each wire is considered to fracture at 7%, which is typically assumed in design codes. The DMs considered were the peak column displacement, peak post-tensioning strain, peak cover concrete strain, and peak confined concrete strain (representing the initiation of plateau in the selected model). The fragility curve for peak displacement is shown in Figure 59. The median peak displacement exceeds the selected displacement limit state at 8.9 g when the tendon is assumed to fracture at 7.0%, whereas, for first wire fracture at 2.41%, the median peak displacement exceeds the selected displacement limit state at 7.2 g. A fragility curve for the peak post-tensioning strain for each wire is shown in Figure 60. Note that the dark black line shows the fracture strain of all 7-wires with 7.00% fracture strain; whereas, the rest are 7 separate wires with successive wire fractures ranging from 2.41%-9.08%. The fragility curves for both the confined and unconfined concrete seem to follow the same trend for both the scenarios. This is because the first wire fracture does not occur until after the concrete failure which explains

why there is no difference. The tendons act similarly until the first wire fracture of the first scenario. The fragility curves for both the confined and unconfined concrete are shown in Figure 61. Figure 62 shows all the fragilities plotted against each other with the peak median values shown in Table 13.
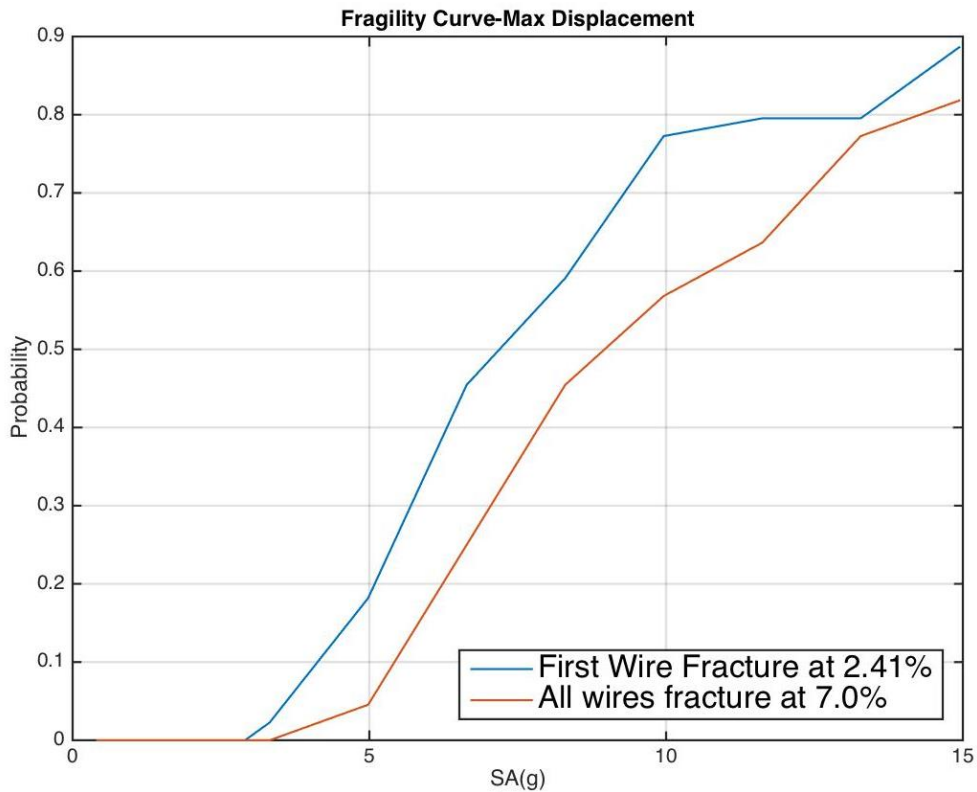
Figure 59 Fragility curve for max displacement
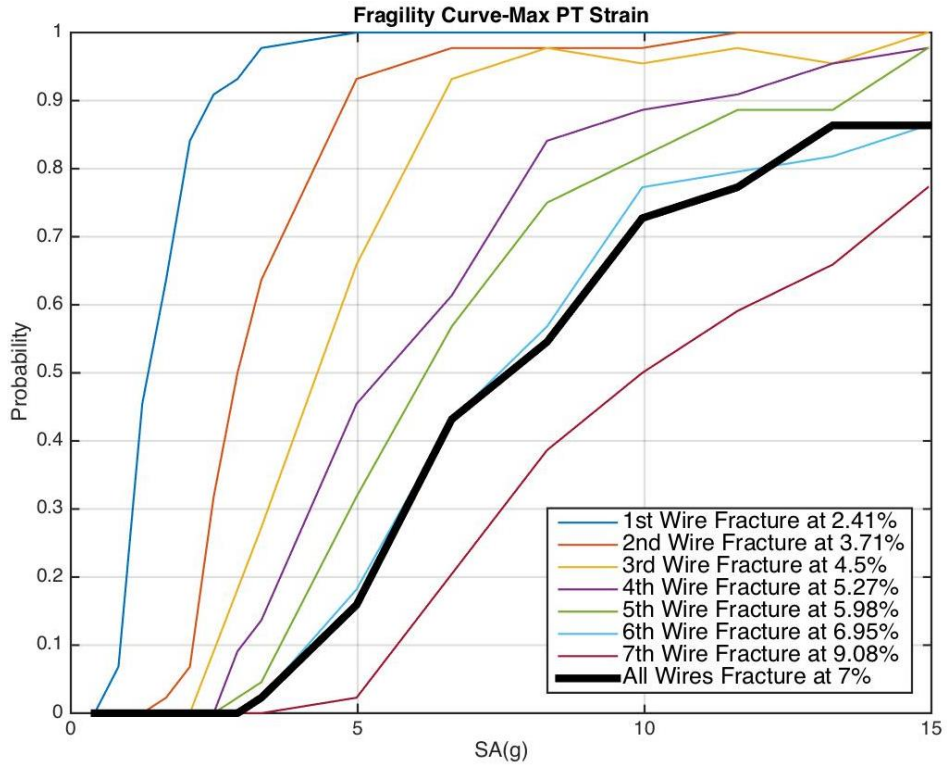
Figure 60 Fragility Curve for Max Post-Tensioning Strain
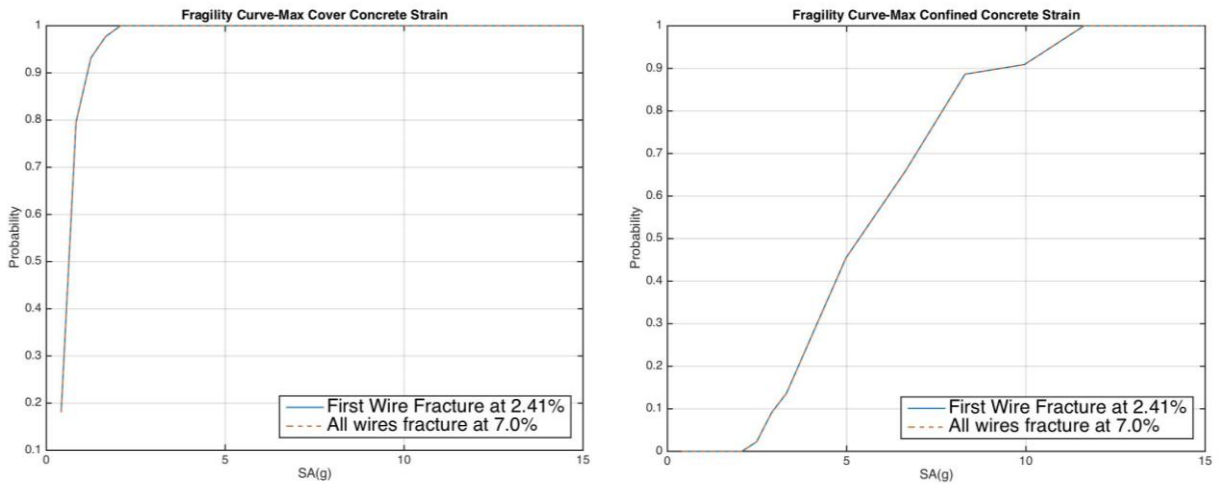
Figure 61 Fragility Curve for Max Confined and Max Unconfined Concrete Strain
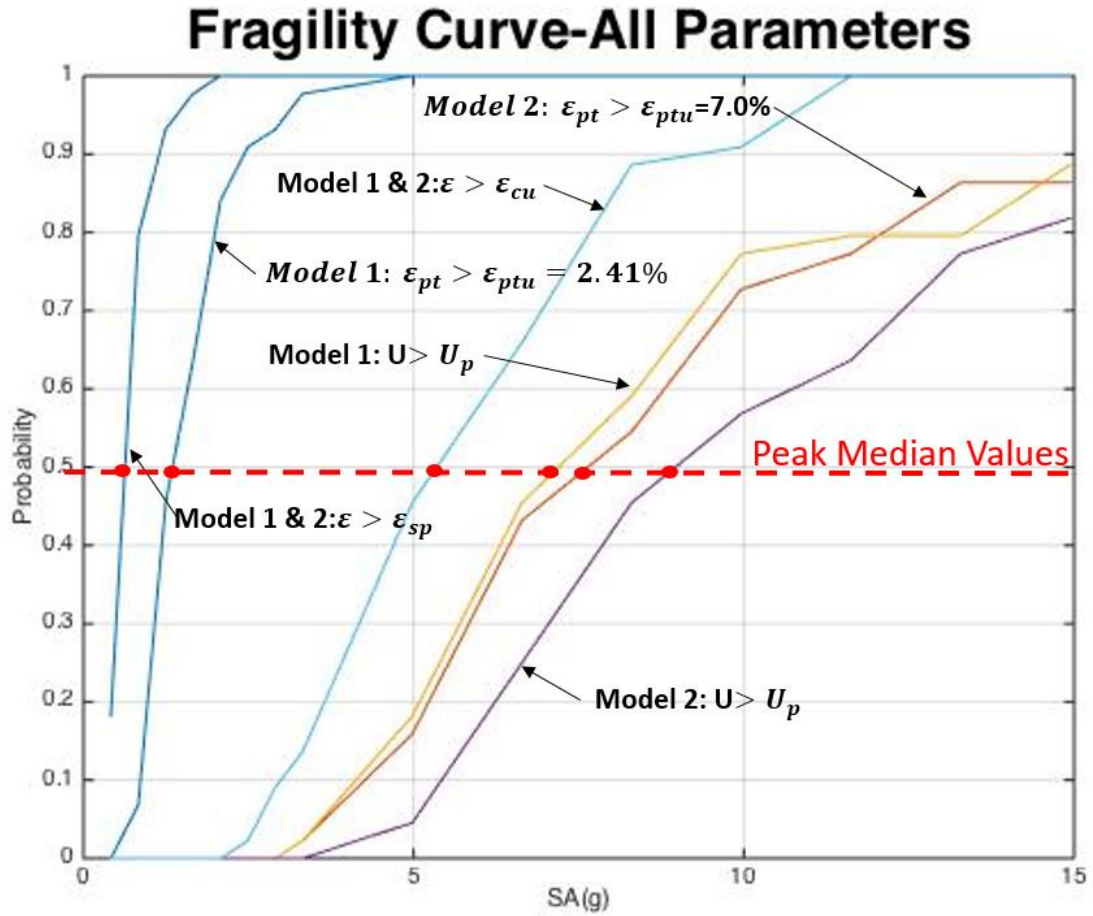
Figure 62 Fragility curves comparing Model 1 & Model 2 with respect to various damage measures

Table 13 Median Peak Values for two Separate Models

	Median Peak Value	
Damage Measure	Model 1	Model 2
Tendon Fracture	1.35g's	7.6g's
Displacement	7.2g's	9.0g's
Cover Concrete Strain	.63g's	.63g's
Confined Concrete Strain	5.3g's	5.3g's

4. CONCLUSION

Two separate columns were studied for this thesis. The first column was a column designed and tested by. Marriott et al (2009). This column had energy dissipators and four internal unbonded tendons, which served as a self-centering mechanism for the rocking column and simulated gravity loads. The second column was a column designed and tested by (Sideris, 2012). This column did not include energy dissipators, but included sliding at the joints and had 8 unbonded tendons to provide self-centering. Joint sliding was not considered in this study. Two analytical models were created for each column with two separate contact surfaces, calibrated through parametric studies in this thesis. Parametric studies were also performed for design parameters to investigate the effect on the columns overall response.

An important conclusion made from the monotonic and cyclic pushover analysis was that the HSR joint and Multi-Spring contact surfaces responded similarly and provided responses close to the experimental data. However, the HSR element was much easier to use. The multi-spring contact has many nodes and many elements, while the HSR joint element only has 2 nodes and 1 element. It was also concluded that increasing the PT force ratio results in greater lateral strength and early tendon yielding. Therefore, the PT force ratio should be chosen so that large lateral strength is achieved without diminishing the ductility capacity of the column through early tendon yielding. Increasing the yield strength of the dissipators was shown to increase the lateral strength and energy dissipation capabilities of the column.

Incremental Dynamic Analyses were performed only for the column by (Sideris, 2012), with the sliding being restrained. The far-field ground motion set from FEMA-P695 was used and scaled with a similitude analysis, since the column was a scaled model. The IDA investigated the effect of assuming tendon fracture at a strain of 7 %, compared to recent experimental data, which have concluded that individual wires fracture prematurely at the location of the anchorage hardware, with the first wire fracture occurring at 2.4%. Damage measures were monitored throughout these analyses and the probability of them exceeding specified limit states under a given intensity measure was computed. Through these fragility curves, the effect of premature tendon fracture on the seismic performance of the selected rocking columns was quantified.

It was concluded that designing the tendons to fracture at a 7.00% strain underestimates the probability of failure. This study shows that premature tendon fracture should be considered when designing rocking bridge piers, which can be used in order to maintain small residual displacements after strong earthquakes. In fact, self-centering is provided by the unbonded PT tendons, while adding dissipators help provide hysteretic damping.

5. REFERENCES

ACI (2001). (n.d.). *Acceptance Criteria for Mement Frames Based on Structural Testing (T1.1-01) and commentary (T1.1R-01).* Farmington Hills, Michigan: A.I.T.G.1. ed..

FEMA. (2009). *Quantification of Building Seismic Performance Factors.* FEMA P695, Prepared by the American Society of Civil Engineers for the Federa, Emergency Management Agency, Washington, D.C.

Hewes, J., & Priestley, M. (2002). *Seismic design and performance of precast concrete segmental bridge columns.* Structural Systems Research Project, Univ. of California at San Diego.

Housner, G. (1963). The Behavior of Inverted Pendulum Structures During Earthquakes. *Bulletin of the Seismological Society of America, 53*(No. 2), 403-417.

Kent, D., & Park, R. (1971). Flexural Members with Confined Concrete. *Journal of the Structural Division, 97*(ST7), 1969-1990.

Lee, W., & Billington, S. (2011). Performance-based earthquake engineering assessment of a self-centering, post-tensioned concrete bridge system. *EARTHQUAKE ENGINEERING AND STRUCTURAL DYNAMICS, 40*, 887-902.

Mander, J., & Cheng, C. (1997). *Seismic resistance of bridge pier based on damage avoidance design.* Univ. at Buffalo—State Univ. of New York.

Mander, J., Priestly, M., & Park, R. (1988). Theoretical Stress-Strain Model For Confined Concrete. *Journal of Structural Engineer, No. 8.*

Marriott, D. (2009). *The Development of High-Performance Post-Tensioned Rocking Systems for the Seismic Design of Structures.* Christchurch New Zealand.

Marriott, D., Pampanin, S., & Palermo, A. (2009). Quasi-static and pseudo-dynamic testing of unbonded post-tensioned rocking bridge piers with external replaceable dissipaters. *EARTHQUAKE ENGINEERING AND STRUCTURAL DYNAMICS, 38*, 331-354.

Mattock, A., Yamazaki , J., & Kattula, B. (1969). *A Comparison of the Behavior of Post-Tensioned Pre-stressed Concrete Beams with and without Bond.* Mechanics Report, University of Washington, Department of Civil Engineering.

Megally,, S., Garg, M., Seible , F., & Dowell, R. (2002). *Seismic Performacnce of Precast Segmental Bridge Superstructures.* University of Calfornia, San Diego , Department of Structural Engineering, La Jolla, California.

OpenSees. (2016). *Zero Tensile Strength*. Retrieved 2016, from http://opensees.berkeley.edu/wiki/index.php/Concrete01_Material_--_Zero_Tensile_Strength.

Ou, Y., Chiewanichakorn, M., Aref, A., & Lee, G. (2007). Seismic performance of segmental precast unbonded post-tensioned concrete bridge columns. *J. Struct. Eng, 133*(11), 1636–1647.

Reddiar, M. K. (2009). *Stress-Strain Model of Unconfined and Confined Concrete and Stress-Block Parameters.*

Roh, H., & Reinhorn, A. (2010). Nonlinear Static Analysis of Structures with Rocking Columns. *J. Struct. Eng*.

Sakai, J., & Mahin, S. (2003). Hysteretic Behavior and Dynamic Response of Re-Centering Reinforced Concrete Columns.

Salehi, M., & Sideris, P. (2016). Nonlinear Dynamic Analysis of Hybrid Sliding-Rocking Bridges. *Geotechnical and Structural Engineering Congress.*

Scott, B., Park, R., & Priestley, M. (1982). Stress-Strain behavior of concrete confined by overlapping hoops at low and high strain rates. *American Concrete Instuitute, 79*, 13-27.

Sideris, P. (2012). *"Seismic Analysis and Design of Precast Concrete Segmental Bridges" Ph.D. Dissertation.* State University of New York at Buffalo, Department of Civil, Structural and Environmental Engineering, Buffalo, NY, U.S.A.

Sideris, P. (2015). NonLinear quasi-static analysis of hybrid sliding-rocking bridge columns subjected to lateral loading. *Engineering Structures*, 125-137.

Sideris, P., Aref, A., & Filiatrault, A. (2014). Effects of anchorage hardware on the cyclic tensile response of unbonded monostrands. *PCI Journal*.

Trono, W. D. (2014). *Earthquake Resilient Bridge Columns Utilizing Damage Resistant Hybrid Fiber Reinforce Concrete. .* University of California, Berkeley.

Vamvatsikos, D., & Cornell, A. (2002). Incremental Dynamic Analysis. *Earthquake Engineering and Structural Dynamics, 31*, 491-514.

Vamvatsikos, D., & Cornell, A. (2005). The Incremental Dynamic Analysis And Its Application TO Performance-Based Earthquake Engineering. *12th Eurpoean Conference on Earthquake Engineering.* 12th Eurolsevier Science Ltd.

Vamvatsikos, D., & Cornell, A. (2006). Direct estimation of the seismic demand and capacity of oscillators with multi-liner static pushovers through IDA. *Earthquake Engineering and Sructural Dynamics*.

APPENDICES

Appendix I.   Mass Calculations

i.   Marriott Column

Note: for Marriott Model Units are kips and inch.

$$I_{xx} = \underbrace{\frac{bh^3}{12}}_{\text{Outer}} - \underbrace{\frac{bh^3}{12}}_{\text{Inner}} = \frac{111.5" * (19.68")^3}{12} - \frac{91.23" * (16.1")^3}{12} = \mathbf{39094in^4}$$

$$I_{yy} = \underbrace{\frac{bh^3}{12}}_{\text{Outer}} - \underbrace{\frac{bh^3}{12}}_{\text{Inner}} = \frac{19.68" * (111.5")^3}{12} - \frac{16.1" * (92.23")^3}{12} = \mathbf{1220766in^4}$$

Superstructure

$$I_m = \rho * L * J_o$$

$$\rho = \frac{8.68 * 10^{-5} \, kips/in^3}{386.4 \, in/s^2} = 2.25 * 10^{-7} \, kips * sec^2/in^4$$

$$L = 39.33 ft = 471.96 \text{in}$$

$$J_0 = I_x + I_y = 39094 in^4 + 1220766 in^4 = 1259860 in^4$$

$$J_0 = 1259860 in^4$$

$$I_m = \rho * L * J_o = 2.25 * 10^{-7} \, kips * sec^2/in^4 * 471.96 \text{in} * 1259860 in^4 = \mathbf{133.78 kips *}$$
$$\mathbf{sec^2 * in}$$

ii. Sideris Column
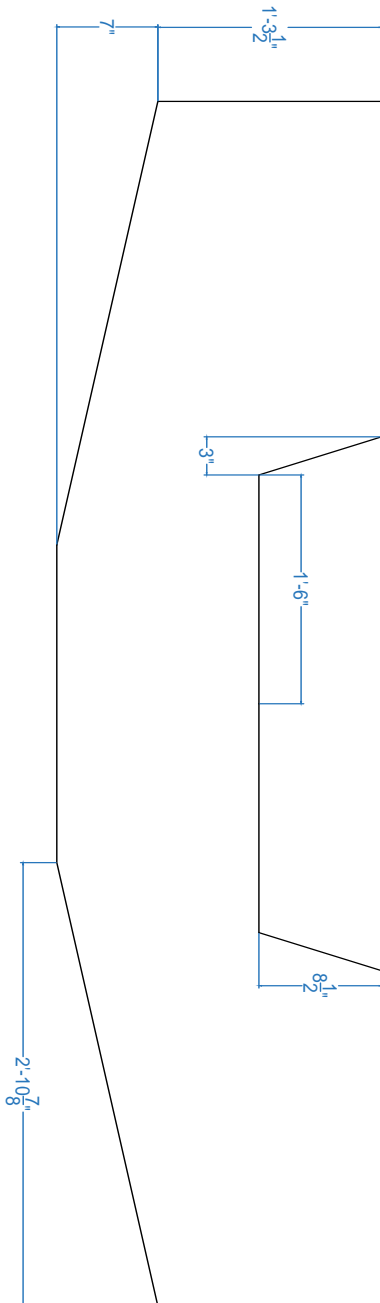
Command: MASSPROP
Select objects: 1 found
Select objects:

---------   ----- REGIONS -------------
Area: 1556.2500 sq in
Perimeter: 233.9189 in
Bounding box: X: -47.3750 -- 47.3750 in
Y: -11.1344 -- 11.3656 in
Centroid: X: 0.0000 in
Y: 0.0000 in
Moments of inertia: X: 51098.3419 sq in sq in
Y: 1224151.2275 sq in sq in
Product of inertia: XY: 0.0000 sq in sq in
Radii of gyration: X: 5.7301 in
Y: 28.0464 in
Principal moments (sq in sq in) and X-Y directions about centroid:
I: 51098.3419 along [1.0000 0.0000]
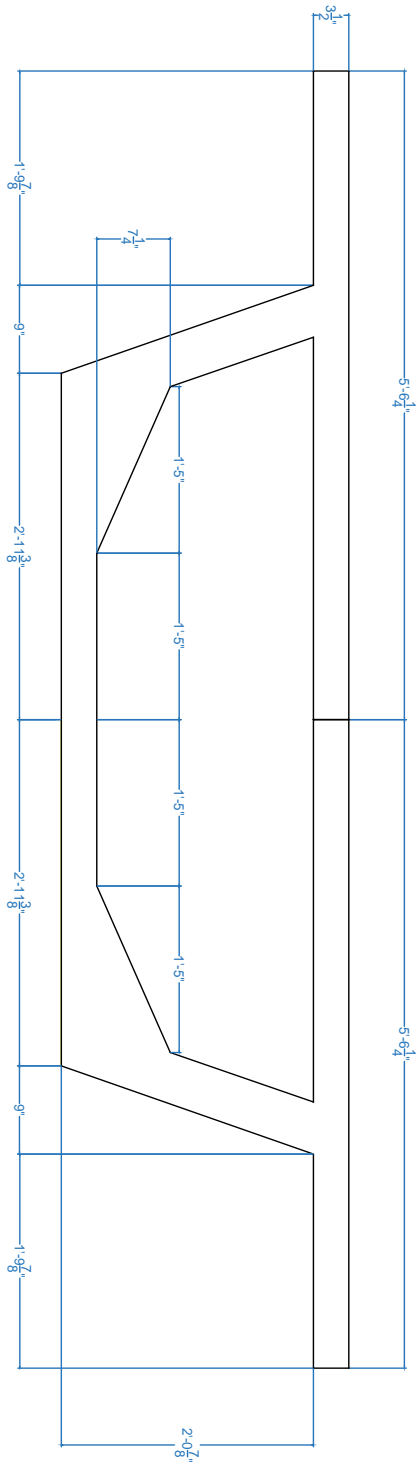
Command: MASSPROP
Select objects: 1 found
Select objects:
-------- REGIONS --------
Area: 1045.4667 sq in
Perimeter: 492.9804 in
Bounding box: X: -66.2500 -- 66.2500 in
                     Y: -15.8869 -- 12.4881 in
Centroid: X: 0.0000 in
                     Y: 0.0000 in
Moments of inertia: X: 124394.8468 sq in sq in
                     Y: 1192672.8377 sq in sq in
Product of inertia: XY: 0.0000 sq in sq in
Radii of gyration: X: 10.9080 in
                     Y: 33.7758 in
Principal moments (sq in sq in) and X-Y directions about centroid:
I: 124394.8468 along [1.0000 0.0000]
J: 1192672.8377 along [0.0000 1.0000]

Geometric Property		Superstructure	Substructure
Area	(in^2)	1047	400
Moment of Inertia – Weak Axis	(in^4)	124431	28333
Moment of Inertia – Strong Axis	(in^4)	1192584	28333
Top Fiber from Centroid	(in)	12.5	12.5
Bottom Fiber from Centroid	(in)	15.875	12.5

From Sideris, 2012

Superstructure

$$I_m = \rho * L * J_o$$

$$\rho = \frac{150\,^{lbs}/_{ft^3}}{32.17\,^{ft}/_{s^2}} = 4.66\,^{lbs * sec^2}/_{ft^4}$$

$$L = \frac{61.9ft}{2} = 30.95ft$$

$$J_0 = I_x + I_y = 124431in^4 + 1192584in^4 = 1317015in^4$$

$$J_0 = 1317015in^4$$

Converting J_o to ft^4 (units used in model)

$$J_0 = 1317015in^4 * \frac{(1ft)^4}{(12in)^4} = 63.5ft^4$$

$$I_m = \rho * L * J_o = 4.66\frac{lbs*sec^2}{ft^4} * 30.95ft * 63.5ft^4 = \mathbf{9158.42lbs * sec^2 * ft}$$

Cap Beam

$$I_m = \rho * L * J_o$$

$$\rho = \frac{150\,^{lbs}/_{ft^3}}{32.17\,^{ft}/_{s^2}} = 4.66\,^{lbs * sec^2}/_{ft^4}$$

$$L = 2'4" = 2.33ft$$

$$J_0 = I_x + I_y = 51098in^4 + 1224151in^4 = 1275249in^4 \text{ (Obtained from AutoCAD)}$$

$$J_0 = 1275249in^4$$

Converting J_o to ft^4 (units used in model)

$$J_0 = 1275249in^4 * \frac{(1ft)^4}{(12in)^4} = 61.50ft^4$$

$$I_m = \rho * L * J_o = 4.66\frac{lbs*sec^2}{ft^4} * 2.33ft * 61.5ft^4 = \mathbf{667.75lbs * sec^2 * ft}$$

Appendix II.   Multi-Spring Model-Marriott

i.   Pushover Analysis

Stress vs Strain for Confined Concrete

Stress vs Drift Ratio for Confined Concrete

Stress vs Strain for Cover Concrete

Stress vs Drift Ratio for Cover Concrete

Left Tendon Vs Right Tendon Force

ii.   Quassi-Static Cyclic Analysis-Marriott Comparison

Left Tendon Vs Right Tendon Force

Stress vs Drift ratios of individual wires of the Right Tendon

Stress vs Drift ratios of individual wires of the Left Tendon

iii. Parametric Study-Cyclic

Variable PT Multi Response

MultiSpring Response with Varying Strength of Dissipators
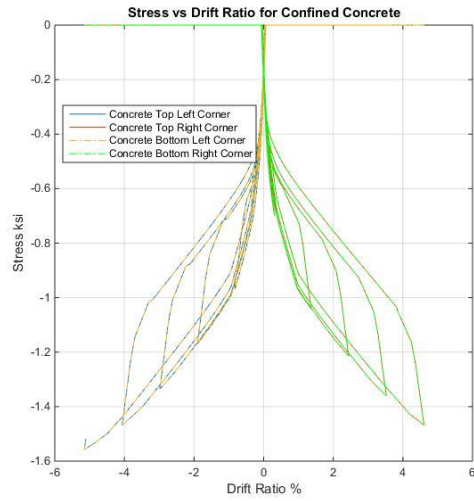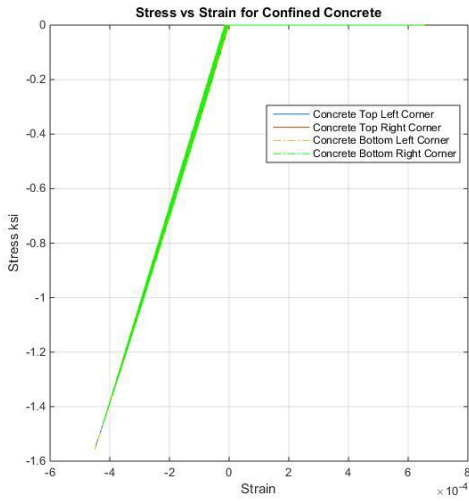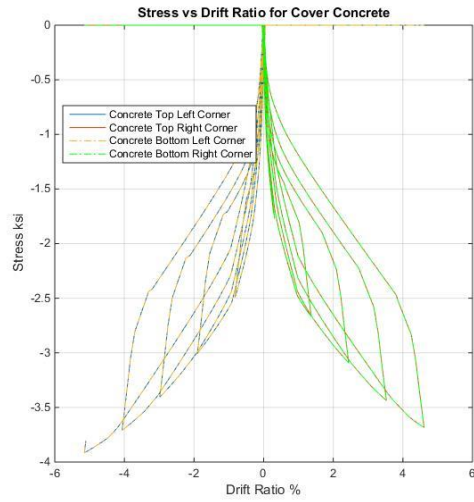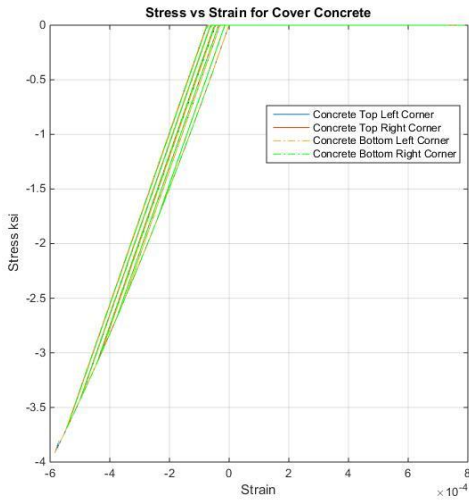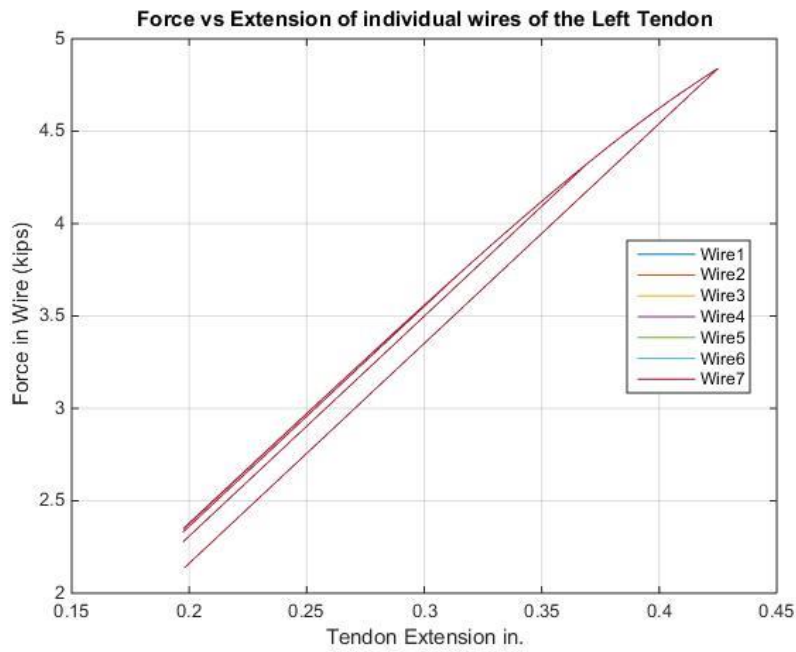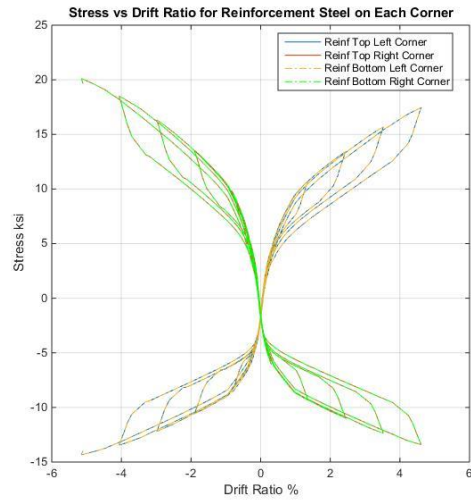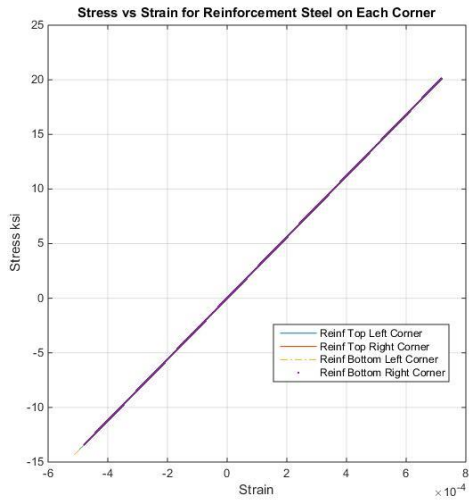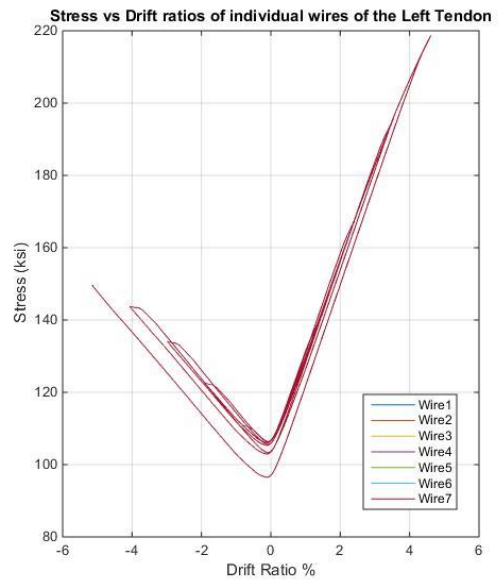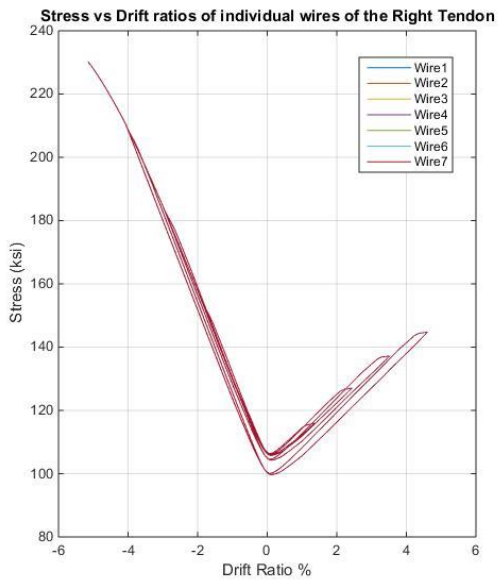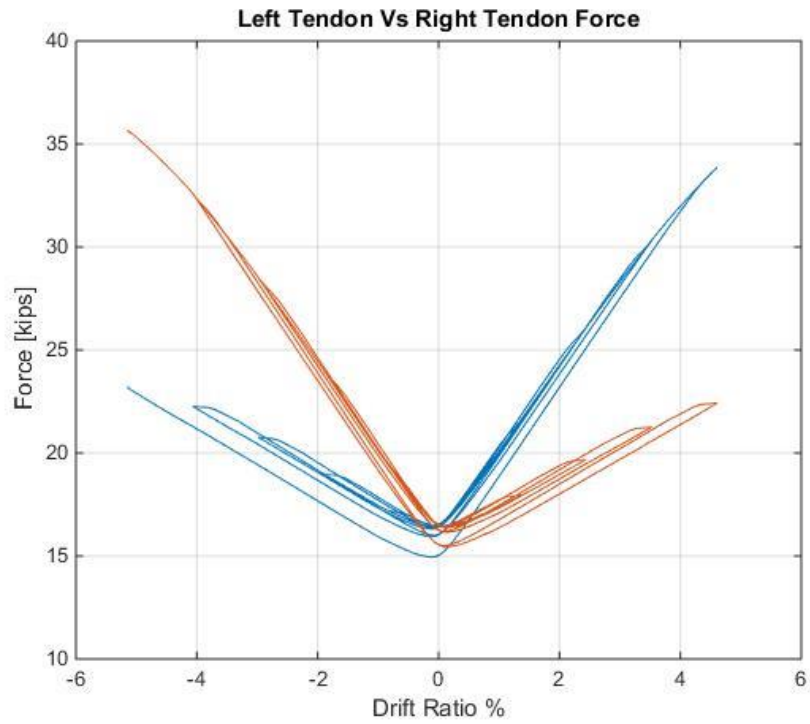
Appendix III. HSR Model-Marriott

i. Pushover Analysis

Stress vs Strain for Reinforcement Steel on Each Corner

Stress vs Drift Ratio for Reinforcement Steel on Each Corner

Stress vs Drift Ratio of Left Dissapator Element

Stress vs Drift Ratio of Central Left Dissapator Element
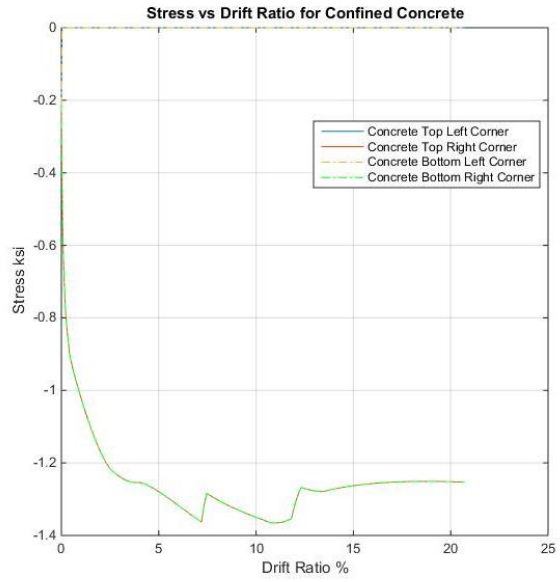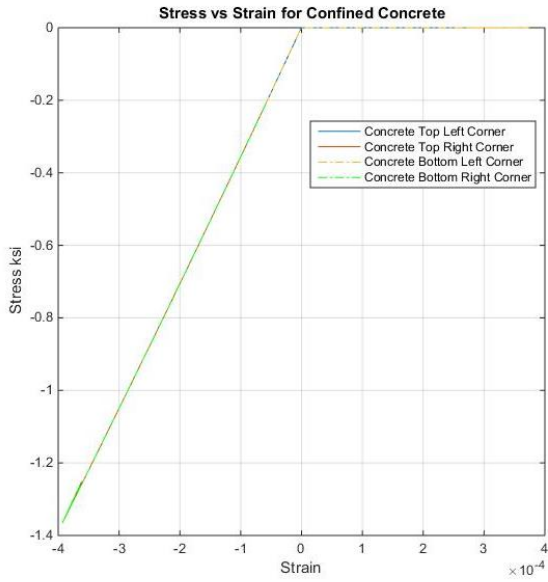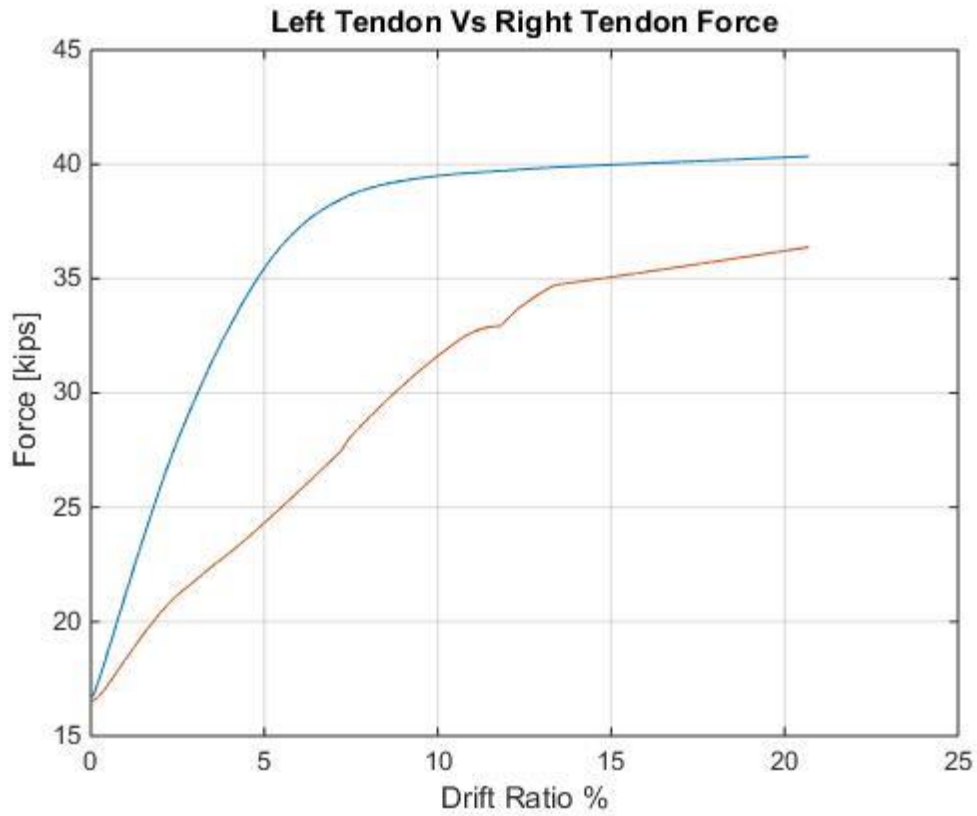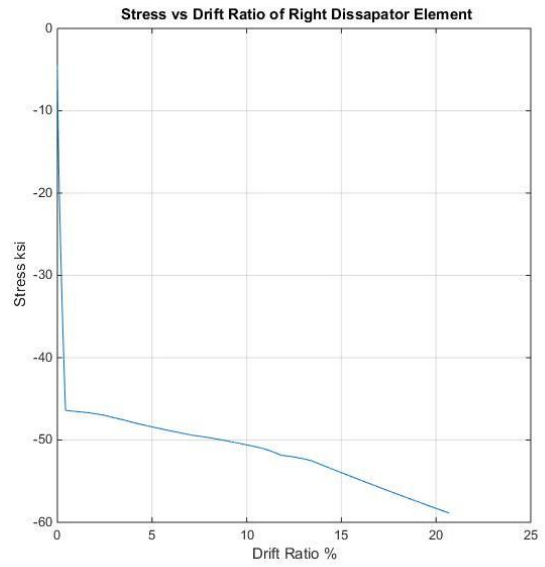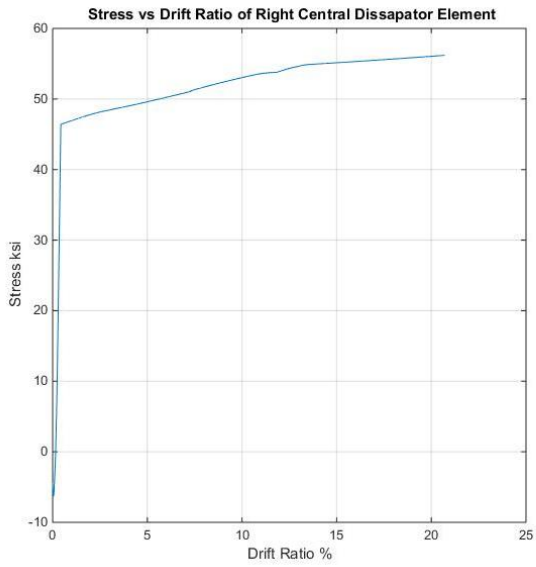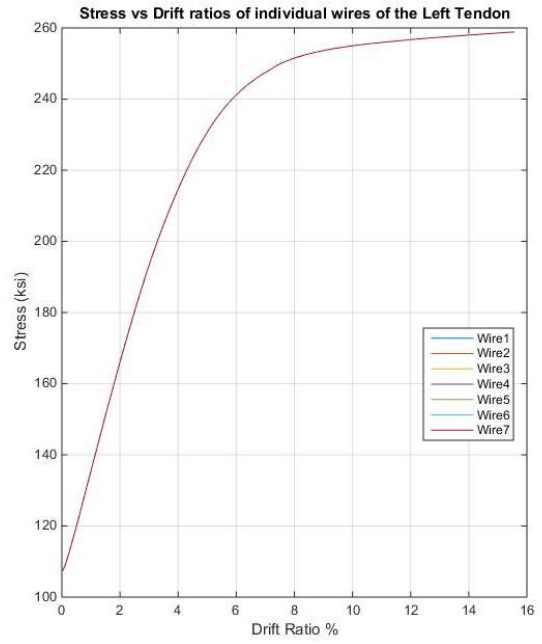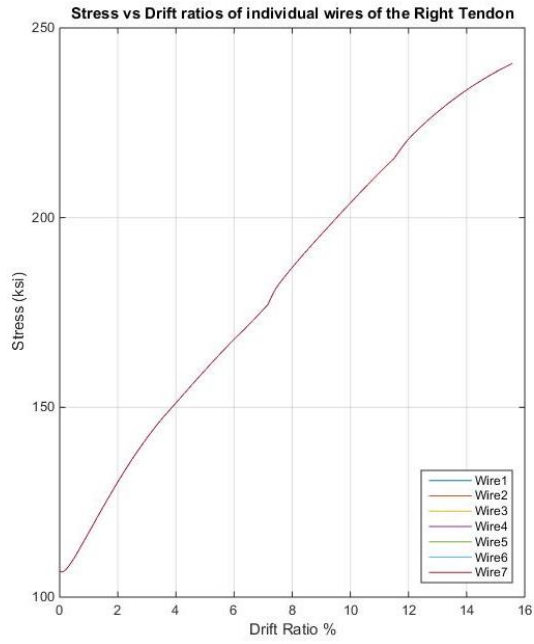
ii.   Quassi-Static Cyclic Analysis-Marriott Comparison

iii.   Parametric Study-Cyclic

HSRSpring Response with Varying Strength of Dissipators

Variable PT HSR Response
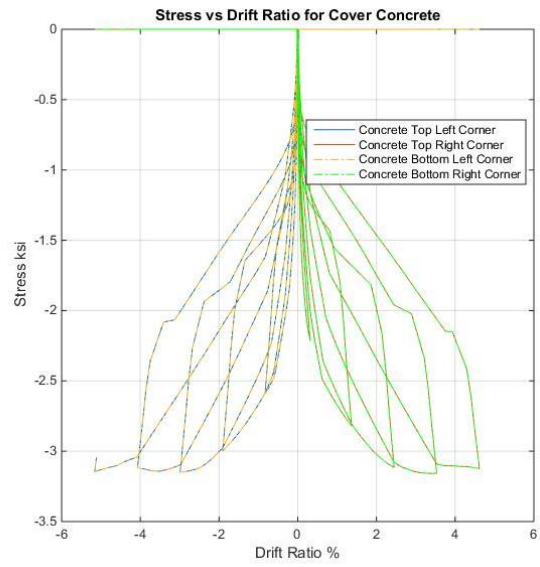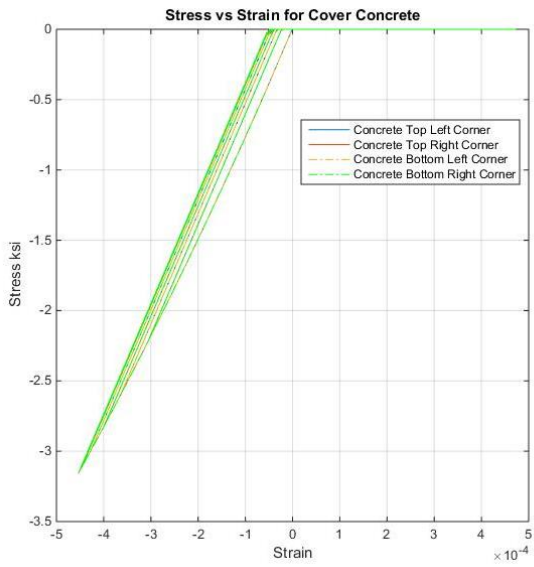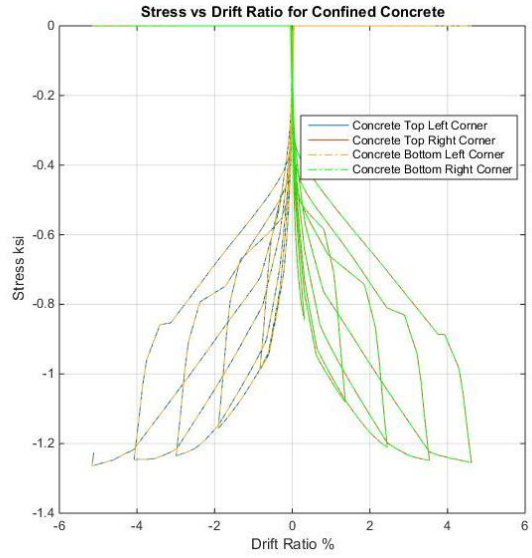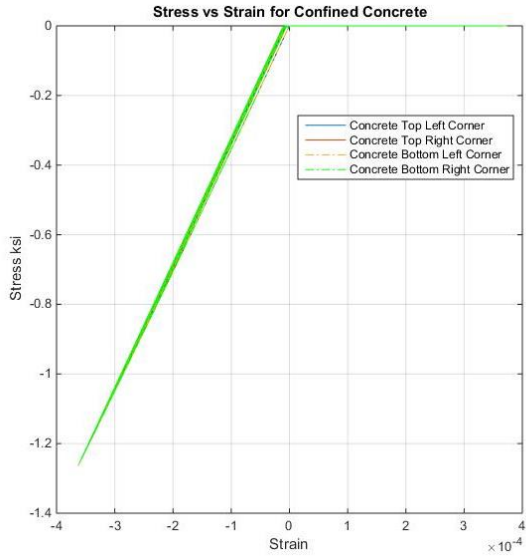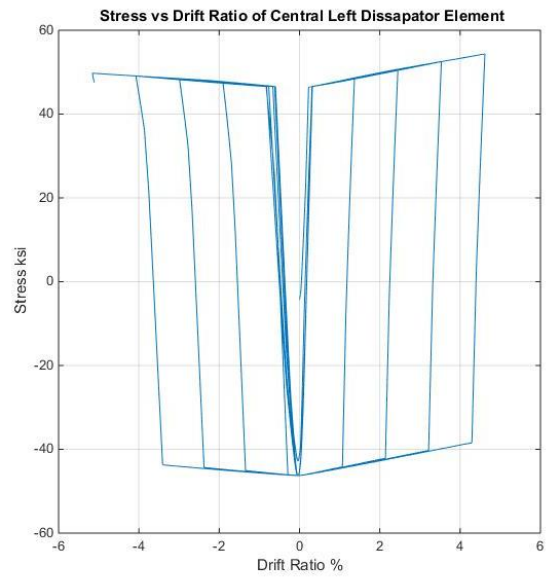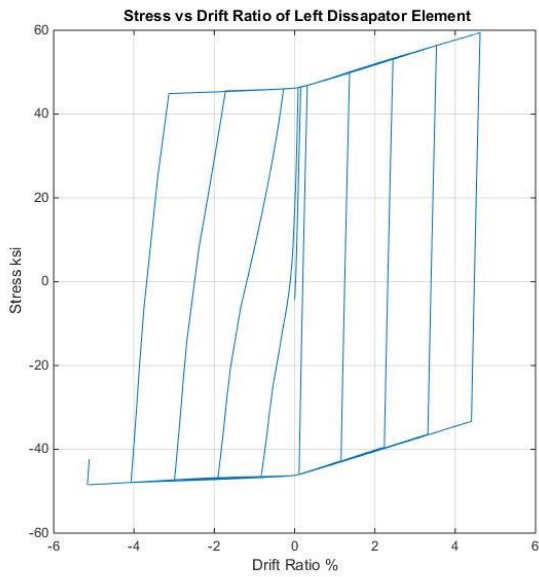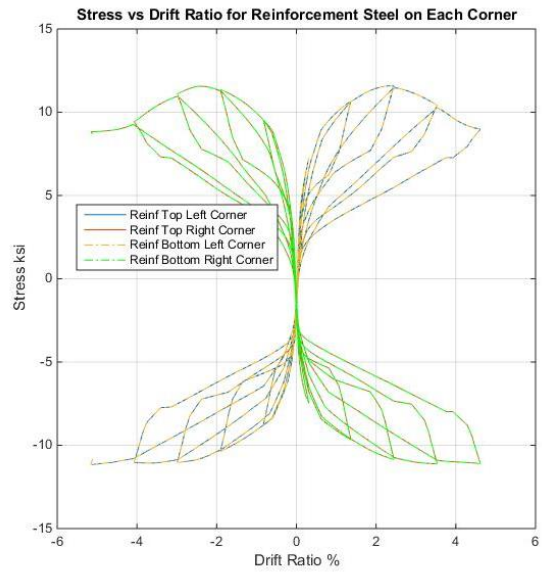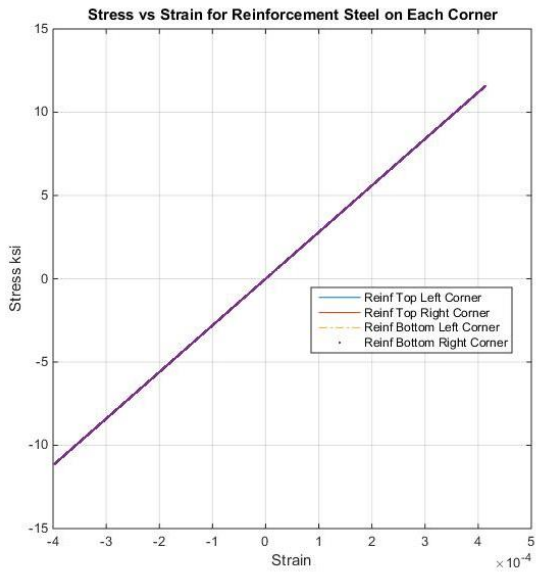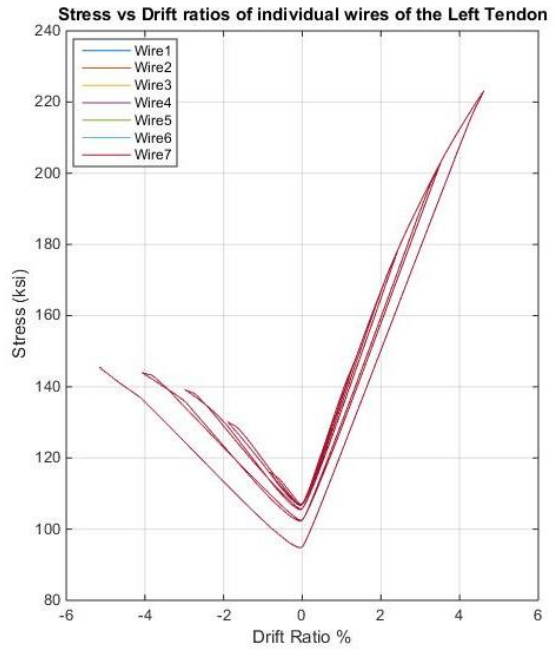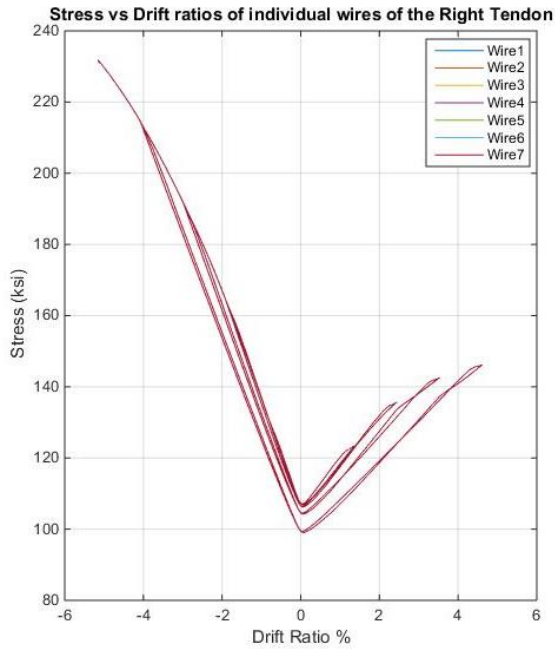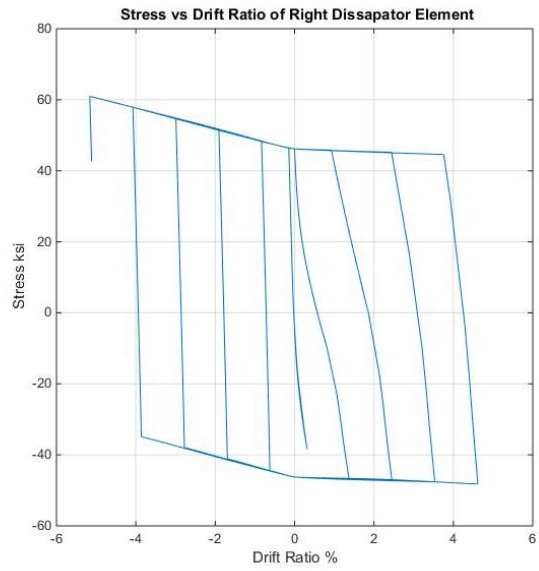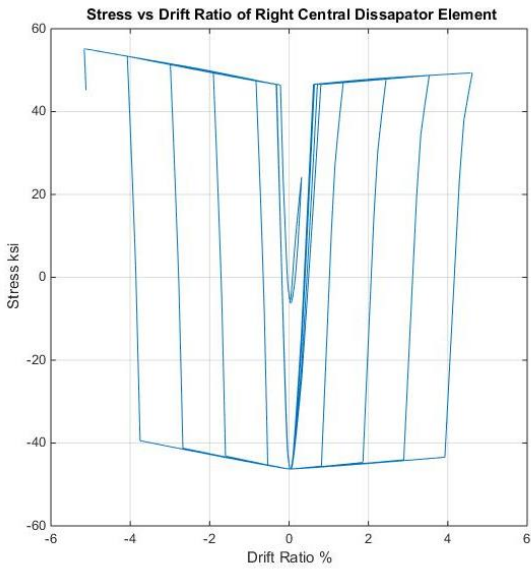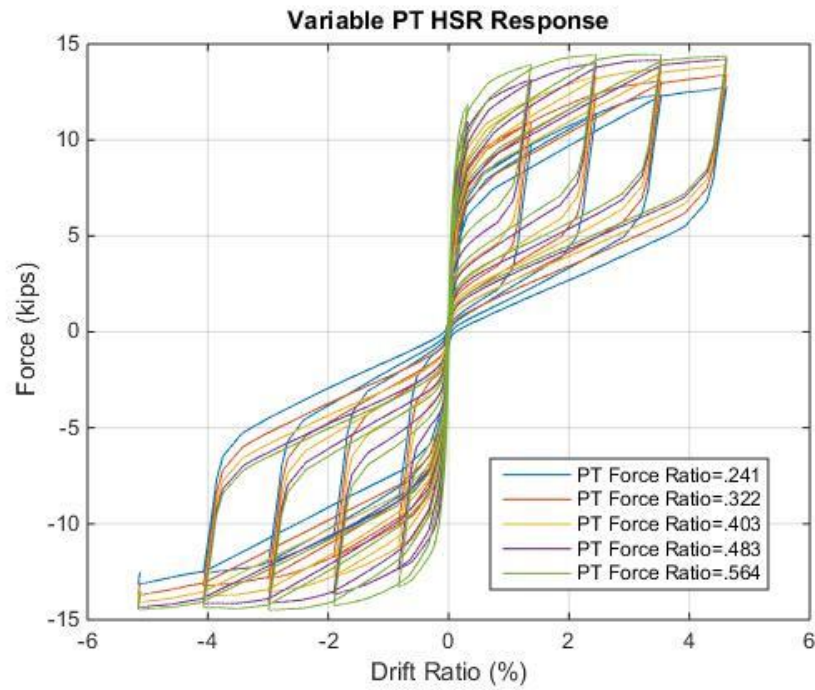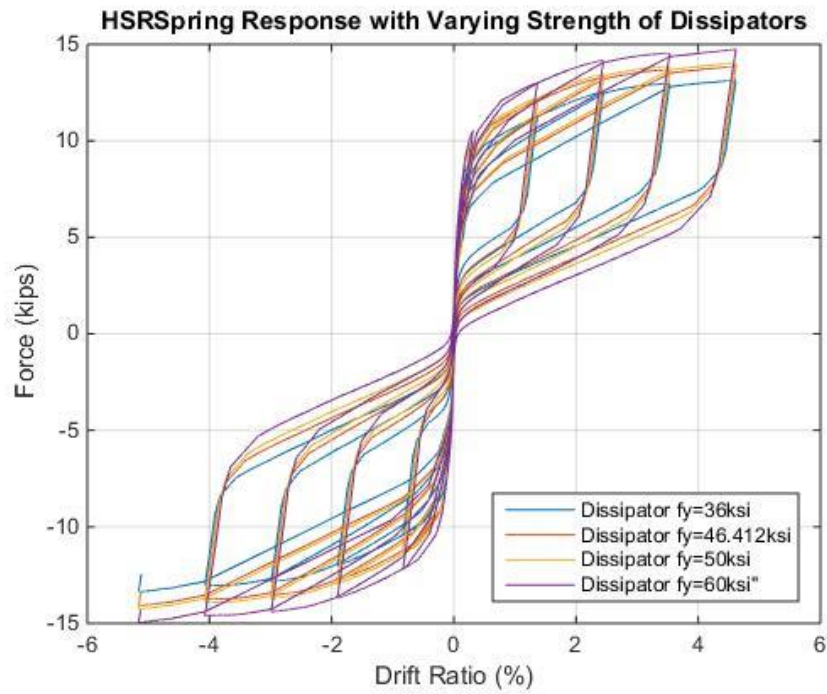
Appendix IV.   IDA Analysis for first wire fracture at 2.41%

i.   Max Displacement

Increment Number	SA(T1)	γ	M1 u_{peak}	M2 u_{peak}	M3 u_{peak}	M4 u_{peak}	M5 u_{peak}	M6 u_{peak}	M7 u_{peak}	M8 u_{peak}	M9 u_{peak}	M10 u_{peak}	M11 u_{peak}	M12 u_{peak}	M13 u_{peak}	M14 u_{peak}	M15 u_{peak}
1	0.415	0.25	0.67882	0.500985	0.571583	0.889382	0.457474	0.641626	0.311821	0.479277	0.388274	0.953687	0.233649	0.488534	0.69869	0.84989	0.91868
2	0.83	0.5	3.1509	2.755458	0.904898	1.05302	1.006157	1.711211	1.220647	0.915313	1.387102	1.762029	0.747821	0.829476	1.171694	1.126984	1.007361
3	1.245	0.75	3.292002	3.428856	2.065554	2.715732	2.076264	3.453336	2.907144	2.382264	1.84113	4.496436	2.15019	1.278146	1.813248	1.598908	2.444544
4	1.66	1	4.818762	4.369806	2.481174	3.761226	2.059182	4.525254	3.502926	4.8591	2.271564	6.722622	3.869874	1.307873	2.272284	2.09385	4.390542
5	2.075	1.25	5.293296	5.3064	5.324454	3.55455	2.796426	5.083938	3.570444	6.579738	5.168772	7.259724	4.377906	2.78595	2.48958	2.52864	4.934412
6	2.49	1.5	6.003378	6.096078	6.678522	4.221234	3.87927	5.37615	5.76477	8.989164	6.417738	8.327466	5.907402	3.884418	3.66309	3.584394	5.125698
7	2.905	1.75	6.338268	7.024428	8.142696	5.340078	4.93407	6.064218	5.892516	10.11386	7.827876	10.4204	7.34022	5.157306	4.0203	5.229936	5.219532
8	3.32	2	6.681654	8.379486	9.48951	6.234714	5.97978	7.038288	6.275934	11.43976	9.437022	12.01635	8.81046	5.30001	6.156972	6.116724	5.346864
9	4.98	3	12.00456	12.30638	13.89433	8.537778	10.14705	9.46674	7.853724	14.74353	11.76867	15.48274	12.54449	7.255476	7.274952	8.360208	7.046748
10	6.64	4	9.93843	16.72144	19.73682	9.915048	14.26118	11.18232	8.923986	17.39975	21.47148	23.5188	16.25355	9.354492	14.71808	15.21083	9.48375
11	8.3	5	13.41929	13.17958	25.17318	11.22926	18.19062	11.72542	13.31519	19.94346	33.4836	38.7405	24.87762	13.75252	22.42692	20.36484	16.78226
12	9.96	6	19.57716	15.7682	28.00746	13.17114	20.80836	14.74353	14.30332	22.46724	35.784	34.7904	31.65048	17.99694	24.30378	21.46176	24.3009
13	11.62	7	25.66512	18.57618	30.73788	15.9385	25.01964	17.07703	16.0315	25.50708	36.56304	39.74742	37.58382	21.8052	22.22514	24.41574	30.58236
14	13.28	8	28.29348	22.32018	32.80752	18.83376	27.55764	19.37808	17.38249	27.95652	43.71912	20.4516	35.73414	25.56162	17.98342	27.78264	4.939038
15	14.94	9	31.39524	25.75584	34.19136	21.29022	28.4067	21.2661	17.47253	29.65986	48.45654	58.27932	35.18496	28.8954	18.47664	30.28068	40.52322

Increment Number	SA(T1)	γ	M16 u_{peak}	M17 u_{peak}	M18 u_{peak}	M19 u_{peak}	M20 u_{peak}	M21 u_{peak}	M22 u_{peak}	M23 u_{peak}	M24 u_{peak}	M25 u_{peak}	M26 u_{peak}	M27 u_{peak}	M28 u_{peak}	M29 u_{peak}	M30 u_{peak}
1	0.415	0.25	0.653063	0.36473	0.236381	0.160292	0.118591	0.3285	0.152293	0.386066	0.82291	1.032392	0.971314	0.435029	0.347249	0.31522	0.346786
2	0.83	0.5	1.895994	0.642353	0.550778	0.328707	0.245446	1.898334	0.34659	1.128791	1.629637	1.294848	1.022306	1.083933	0.741316	1.332009	0.864736
3	1.245	0.75	2.449116	0.90736	1.660369	0.399328	0.491895	1.241258	2.66823	1.387942	2.122326	4.840578	1.595117	1.429207	1.184976	1.843416	1.842714
4	1.66	1	3.311928	1.22195	4.233204	0.762989	0.863939	3.937896	1.183678	2.031444	5.457222	5.559174	3.764664	1.763118	2.772108	1.900746	2.987478
5	2.075	1.25	3.986946	1.74213	5.534802	1.220722	1.423755	4.793238	4.58388	1.811556	4.921074	7.23753	4.315158	1.933992	4.037796	2.136456	5.640372
6	2.49	1.5	5.217858	2.390742	7.517196	1.425974	2.578194	8.049618	5.454828	3.36762	5.676408	6.934986	4.146444	1.727577	6.06861	1.697263	9.542196
7	2.905	1.75	6.242148	2.75553	9.232146	1.576714	2.17368	10.66617	5.335164	3.66435	6.2811	7.160976	4.161348	1.96326	7.93917	2.949066	12.21172
8	3.32	2	6.880968	4.559832	10.45795	2.463444	1.575113	11.2059	6.065514	4.433994	6.876324	7.205796	4.41882	3.029454	9.133848	2.972034	15.15427
9	4.98	3	7.977186	14.65402	14.41237	3.822372	9.16083	11.63635	9.037602	6.017238	9.376452	9.402102	6.480828	4.81212	14.07236	7.792794	21.73068
10	6.64	4	9.197784	20.86272	18.24048	5.444442	11.81428	15.41376	9.025398	8.161506	12.7615	13.42991	10.24096	7.660764	19.87524	14.02225	25.0119
11	8.3	5	11.99569	25.98876	21.5379	5.061906	12.37991	19.84716	11.49485	9.400068	16.92387	20.87154	9.702054	8.021106	24.68628	16.21823	27.66204
12	9.96	6	14.87099	29.41776	23.57568	5.494464	16.98557	22.41378	12.52289	11.6876	20.92986	15.42262	9.237636	8.654634	28.58256	6.43905	21.33576
13	11.62	7	17.26472	36.68562	24.05232	7.21566	23.22504	27.67446	13.96876	12.62482	23.78286	8.117262	5.716728	9.83853	31.48902	7.222662	32.09058
14	13.28	8	21.72726	45.14436	26.80146	12.30462	31.52646	34.97382	19.96956	15.16282	26.46828	8.26695	4.662324	10.89871	34.72614	4.378878	23.70942
15	14.94	9	23.34942	58.03362	30.0735	14.08354	46.2411	44.95086	22.52484	16.16481	29.49282	22.19796	10.51841	12.6931	36.68328	19.76922	11.63596

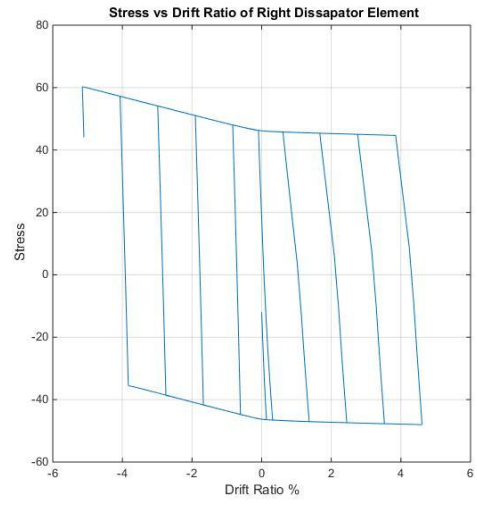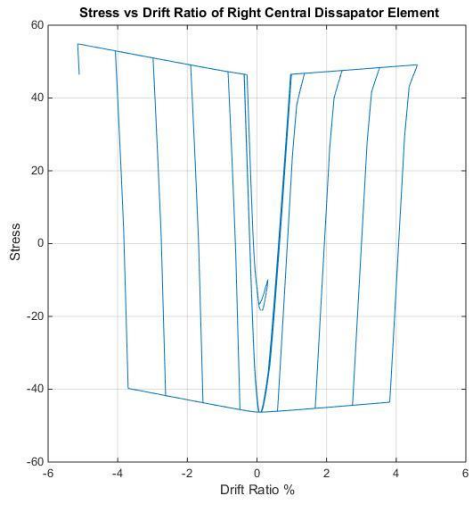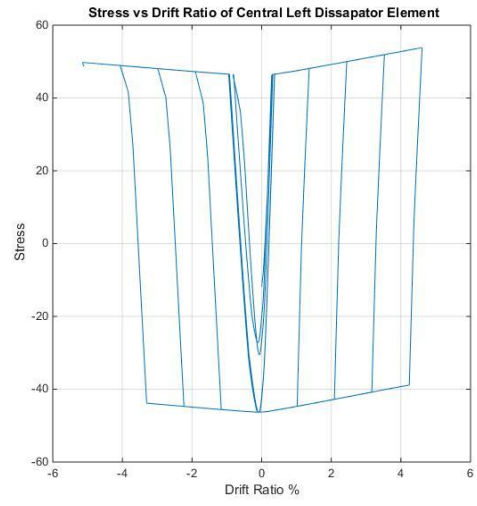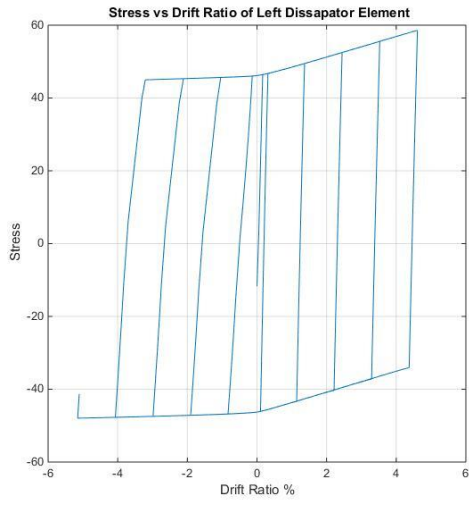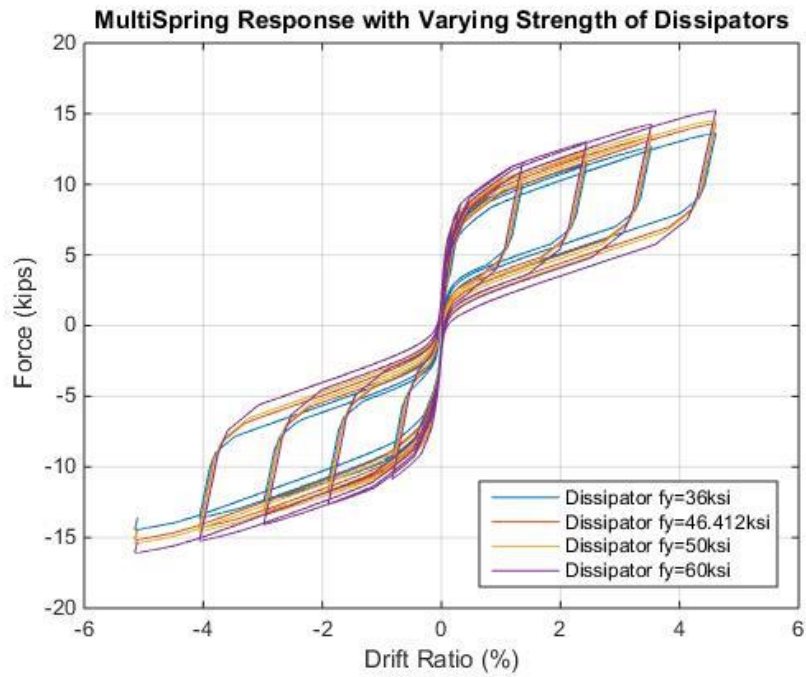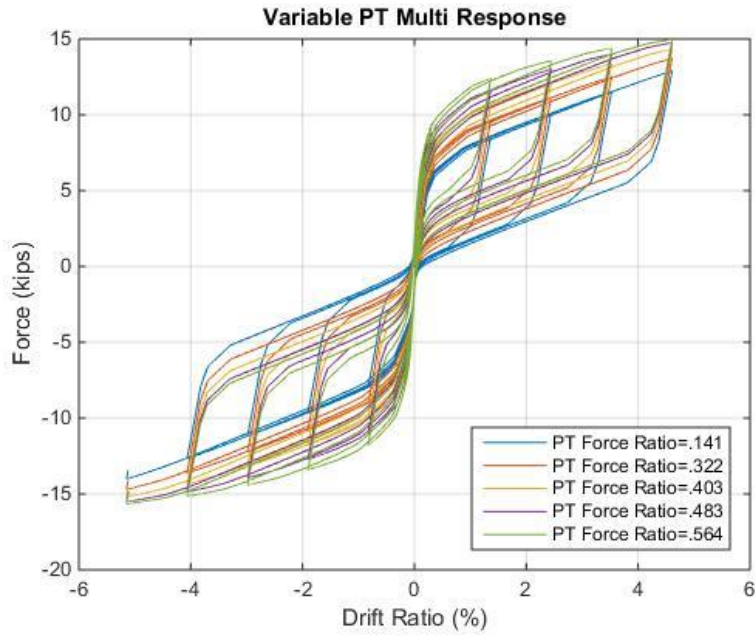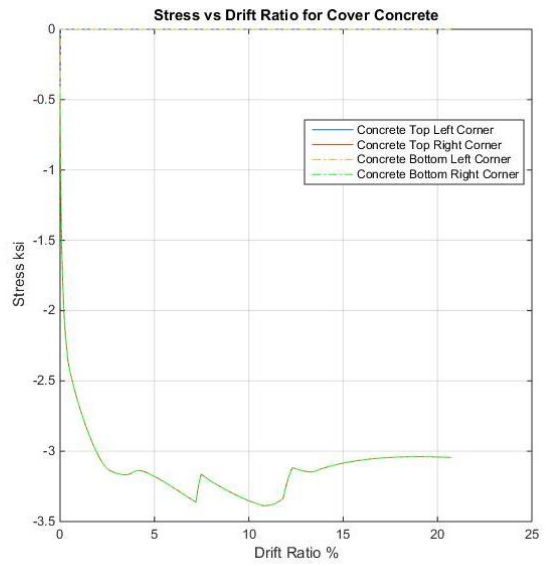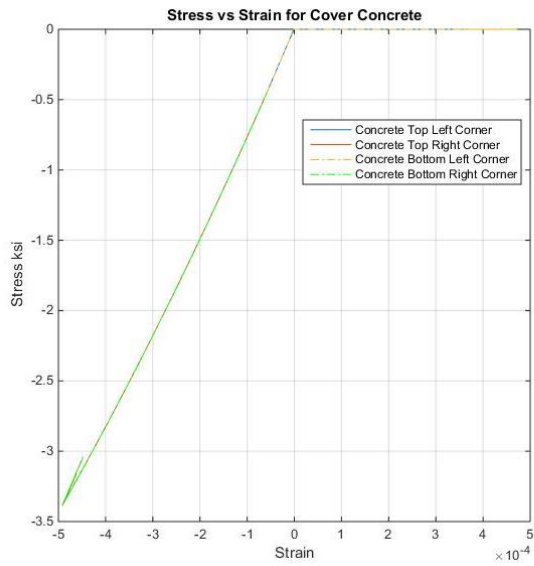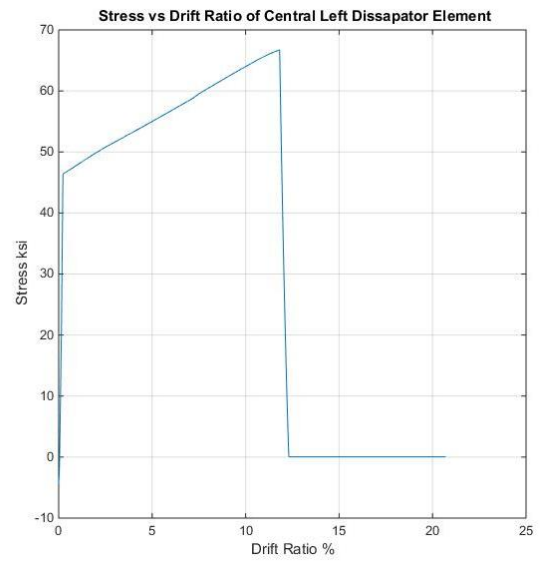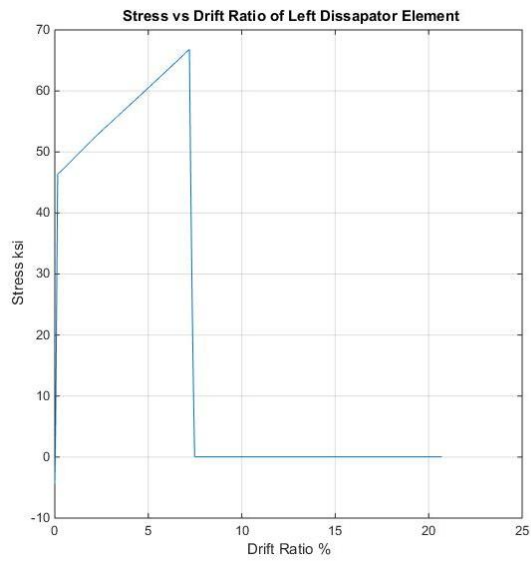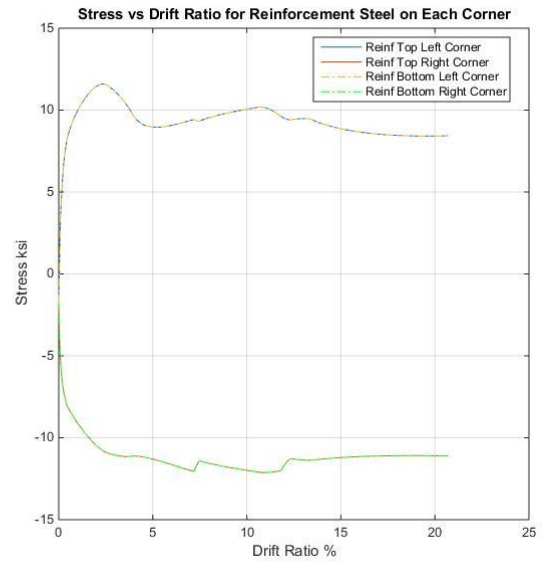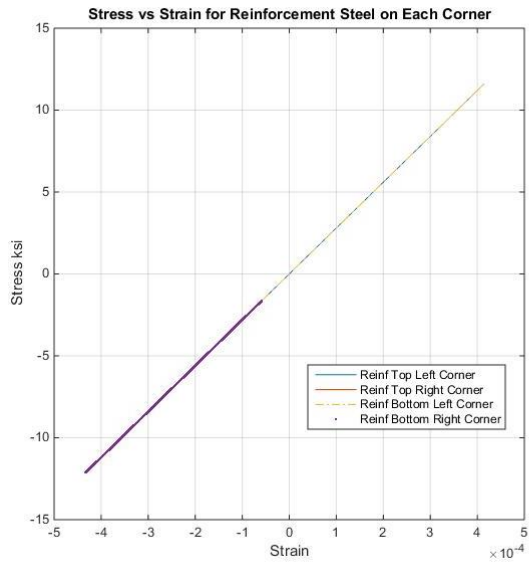| Increment Number	SA(T1)	γ	M31 u_{peak}	M32 u_{peak}	M33 u_{peak}	M34 u_{peak}	M35 u_{peak}	M36 u_{peak}	M37 u_{peak}	M38 u_{peak}	M39 u_{peak}	M40 u_{peak}	M41 u_{peak}	M42 u_{peak}	M43 u_{peak}	M44 u_{peak}
1	0.415	0.25	0.423841	0.175778	0.460908	0.573511	0.607468	0.427918	0.183182	0.186257	0.653537	0.639767	0.556171	0.319484	0.339921	0.859054
2	0.83	0.5	0.737073	0.387612	1.32296	0.880704	1.729723	0.679579	0.786479	0.390281	1.094908	1.532918	2.363598	0.462152	0.981504	1.627999
3	1.245	0.75	1.021504	0.654455	2.393262	2.503944	2.779128	1.175611	0.75319	1.815912	1.175846	1.805724	4.043052	1.583116	1.519335	2.33433
4	1.66	1	1.514918	0.566798	3.137274	3.262752	3.215214	2.054484	1.219865	2.410884	1.168834	2.386638	4.777668	1.862874	1.904904	2.60478
5	2.075	1.25	3.809862	0.817353	4.137678	3.857454	3.648132	2.650554	1.669981	3.15153	2.585106	3.198276	5.650362	2.928186	2.791584	2.698488
6	2.49	1.5	4.466502	4.799088	5.17914	4.4127	4.525614	3.718476	1.842012	3.55329	2.647404	3.647574	6.671286	2.908224	3.553182	3.456576
7	2.905	1.75	6.251616	8.171802	6.105276	5.905404	5.87979	4.442454	1.704218	4.905738	3.092292	4.511574	7.750368	4.983426	4.226562	4.39983
8	3.32	2	7.432182	11.37524	6.951582	6.73092	6.841548	4.86477	2.53539	6.15744	3.29958	4.576878	8.871138	3.995352	4.863348	4.914792
9	4.98	3	10.1732	18.05094	10.16741	10.74177	9.326646	5.551236	6.499494	15.42442	6.34869	7.05357	13.6589	9.980982	7.127676	6.402474
10	6.64	4	12.59006	22.84668	12.64565	15.73054	11.48911	7.138458	8.29251	20.59992	8.455554	9.152928	23.50224	18.40068	8.77023	8.145216
11	8.3	5	15.76548	26.95842	17.96573	22.55418	13.03468	8.161434	14.10516	29.21472	10.9764	15.01308	34.09776	21.5127	9.990234	9.927792
12	9.96	6	18.88506	30.88656	24.30954	29.58444	14.21041	8.928126	17.03043	34.57422	14.75109	18.24552	40.30956	23.36238	12.17439	11.48512
13	11.62	7	23.31702	37.51668	28.9935	34.35246	15.13568	9.17964	25.11126	20.07396	17.1968	20.97468	46.65384	24.23592	14.69882	12.55856
14	13.28	8	26.51724	38.24118	9.4806	37.6875	18.37548	9.856332	38.17494	15.15431	18.34308	23.13288	52.43958	25.4511	15.74883	12.93451
15	14.94	9	30.90078	39.44484	39.40848	42.36012	20.4939	9.660456	43.26426	64.78596	20.30148	21.7125	58.02444	25.54452	17.17173	13.2842

ii. Max Post-Tensioning Strain

Increment Number	SA(T1)	y	M1 Pt_peak Strain	M2 Pt_peak Strain	M3 Pt_peak Strain	M4 Pt_peak Strain	M5 Pt_peak Strain	M6 Pt_peak Strain	M7 Pt_peak Strain	M8 Pt_peak Strain	M9 Pt_peak Strain	M10 Pt_peak Strain	M11 Pt_peak Strain	M12 Pt_peak Strain	M13 Pt_peak Strain	M14 Pt_peak Strain	M15 Pt_peak Strain
1	0.415	0.25	0.019387	0.018833	0.019042	0.020078	0.018684	0.019263	0.018243	0.018746	0.018465	0.020277	0.018021	0.018775	0.019447	0.019969	0.020173
2	0.83	0.5	0.027895	0.026525	0.020162	0.020628	0.020488	0.022851	0.021184	0.020154	0.021777	0.023039	0.019595	0.019883	0.020978	0.020873	0.020494
3	1.245	0.75	0.028356	0.028924	0.024107	0.026433	0.024121	0.029013	0.027011	0.025173	0.023305	0.032748	0.02441	0.021357	0.023176	0.022487	0.025412
4	1.66	1	0.033923	0.03229	0.025483	0.030102	0.024091	0.032807	0.0292	0.03409	0.024793	0.040849	0.030468	0.021471	0.024806	0.024251	0.032284
5	2.075	1.25	0.035619	0.035783	0.03572	0.02932	0.026634	0.034872	0.029201	0.040251	0.035212	0.042831	0.032297	0.026651	0.025661	0.02577	0.0343
6	2.49	1.5	0.038111	0.038517	0.040598	0.031653	0.030542	0.035987	0.037364	0.048949	0.039753	0.04678	0.037922	0.030448	0.02972	0.029375	0.035027
7	2.905	1.75	0.039382	0.042036	0.045729	0.035861	0.034449	0.0384	0.037892	0.053226	0.044867	0.054302	0.042945	0.035247	0.030972	0.035142	0.0353
8	3.32	2	0.040648	0.046939	0.050734	0.03913	0.03818	0.04199	0.0392	0.058475	0.050553	0.06068	0.048409	0.035617	0.038872	0.038617	0.035782
9	4.98	3	0.060528	0.061403	0.068868	0.047215	0.053384	0.050918	0.044726	0.071516	0.059972	0.075647	0.063032	0.042603	0.042405	0.046302	0.042107
10	6.64	4	0.052389	0.080818	0.092545	0.05197	0.070257	0.057446	0.048623	0.083649	0.102516	0.109734	0.078301	0.05011	0.071277	0.07289	0.050865
11	8.3	5	0.06618	0.06576	0.118506	0.057244	0.087667	0.059556	0.065735	0.095505	0.188648	0.169048	0.11711	0.067836	0.103784	0.095551	0.080749
12	9.96	6	0.091605	0.076205	0.133365	0.065752	0.09936	0.071913	0.070143	0.108214	2.44857	0.192523	0.263187	0.084619	0.113699	0.101977	0.115943
13	11.62	7	0.121002	0.089072	0.172032	0.07723	0.11993	0.081668	0.077564	0.12342	3.87342	3.84021	0.62862	0.102003	0.096486	0.111807	0.171012
14	13.28	8	0.13455	0.105699	0.197355	0.090489	0.132509	0.091718	0.083243	0.148508	0.497381	0.095178	3.85898	0.120326	0.079314	0.128017	0.040777
15	14.94	9	0.17663	0.122448	0.222583	0.101708	0.149476	0.100309	0.083874	0.160022	5.04683	21.3158	0.241557	0.15145	0.079247	0.163403	0.436999

Increment Number	SA(T1)	y	M16 Pt_peak Strain	M17 Pt_peak Strain	M18 Pt_peak Strain	M19 Pt_peak Strain	M20 Pt_peak Strain	M21 Pt_peak Strain	M22 Pt_peak Strain	M23 Pt_peak Strain	M24 Pt_peak Strain	M25 Pt_peak Strain	M26 Pt_peak Strain	M27 Pt_peak Strain	M28 Pt_peak Strain	M29 Pt_peak Strain	M30 Pt_peak Strain
1	0.415	0.25	0.019288	0.018401	0.018032	0.017851	0.017761	0.018281	0.017821	0.018466	0.019872	0.020575	0.020332	0.018618	0.018351	0.018242	0.018357
2	0.83	0.5	0.023488	0.01927	0.018981	0.018318	0.01807	0.023509	0.018343	0.020883	0.022607	0.021572	0.020623	0.020771	0.019621	0.021546	0.020033
3	1.245	0.75	0.025415	0.020134	0.022675	0.018542	0.018864	0.026219	0.021303	0.021844	0.024208	0.033936	0.022572	0.021872	0.021073	0.023447	0.023304
4	1.66	1	0.028394	0.021193	0.031777	0.019708	0.019966	0.030672	0.021108	0.024036	0.036292	0.03658	0.030094	0.023038	0.02662	0.023701	0.027333
5	2.075	1.25	0.030873	0.023023	0.036629	0.021274	0.021893	0.033719	0.033076	0.023265	0.034284	0.042325	0.031965	0.023656	0.031063	0.024361	0.036905
6	2.49	1.5	0.035391	0.025218	0.043824	0.021939	0.025892	0.045641	0.03624	0.028743	0.036945	0.041648	0.031341	0.023046	0.038314	0.022856	0.051064
7	2.905	1.75	0.039179	0.02651	0.049874	0.022527	0.02452	0.055295	0.035786	0.029648	0.039115	0.042584	0.031548	0.023877	0.045018	0.027117	0.061457
8	3.32	2	0.041461	0.033027	0.054617	0.025545	0.022493	0.057514	0.038541	0.032562	0.041294	0.042062	0.032167	0.027534	0.04947	0.027203	0.074171
9	4.98	3	0.045372	0.071718	0.070288	0.030453	0.049715	0.059251	0.049445	0.038314	0.050249	0.050598	0.039596	0.033859	0.069914	0.044836	0.101367
10	6.64	4	0.049847	0.100004	0.086693	0.036163	0.060011	0.074683	0.049437	0.045957	0.062751	0.064089	0.045257	0.043983	0.092612	0.069329	0.117017
11	8.3	5	0.06073	0.125019	0.102426	0.034768	0.062345	0.095379	0.058428	0.050409	0.079222	0.064459	0.046962	0.045158	0.11449	0.077533	0.128365
12	9.96	6	0.072567	0.166453	0.114054	0.036314	0.081099	0.107614	0.062819	0.059156	0.095427	0.069949	0.05047	0.047349	0.132704	0.042476	0.091135
13	11.62	7	0.082914	0.278281	0.116803	0.042334	0.108329	0.134058	0.068711	0.062534	0.107728	0.055249	0.069733	0.051769	0.16954	0.051866	0.131418
14	13.28	8	0.104134	13.9865	0.124039	0.061733	0.182935	0.23973	0.094807	0.072968	0.118322	0.055346	16.8789	0.055672	1.46387	0.037376	0.10036
15	14.94	9	0.112352	5.84889	0.156203	0.068561	3.89354	0.424955	0.105442	0.076588	0.130405	0.096265	0.062235	0.061982	0.23615	0.095031	0.062467

Increment Number	SA(T1)	y	M31 Pt_peak Strain	M32 Pt_peak Strain	M33 Pt_peak Strain	M34 Pt_peak Strain	M35 Pt_peak Strain	M36 Pt_peak Strain	M37 Pt_peak Strain	M38 Pt_peak Strain	M39 Pt_peak Strain	M40 Pt_peak Strain	M41 Pt_peak Strain	M42 Pt_peak Strain	M43 Pt_peak Strain	M44 Pt_peak Strain
1	0.415	0.25	0.018578	0.017877	0.018695	0.019038	0.019151	0.018595	0.017896	0.017898	0.019326	0.019247	0.019006	0.018261	0.018319	0.019964
2	0.83	0.5	0.019585	0.018477	0.021535	0.020046	0.022919	0.019388	0.019728	0.018474	0.020801	0.022357	0.025152	0.018698	0.020387	0.022628
3	1.245	0.75	0.020496	0.019318	0.025211	0.025655	0.026629	0.021072	0.019623	0.023256	0.021061	0.023211	0.031133	0.022434	0.022159	0.025021
4	1.66	1	0.022196	0.019048	0.02786	0.02835	0.028215	0.024044	0.021169	0.025295	0.021052	0.025257	0.03369	0.023445	0.023478	0.02611
5	2.075	1.25	0.030255	0.019842	0.03154	0.030444	0.029754	0.026199	0.022729	0.027923	0.025885	0.028168	0.036771	0.027095	0.026795	0.026279
6	2.49	1.5	0.032553	0.03382	0.035229	0.032408	0.032893	0.030077	0.02333	0.029309	0.026096	0.029892	0.040496	0.027054	0.029567	0.029152
7	2.905	1.75	0.039193	0.046122	0.038643	0.037899	0.037781	0.032617	0.02286	0.034147	0.028144	0.032868	0.044495	0.034412	0.031999	0.032386
8	3.32	2	0.043513	0.058169	0.041756	0.040928	0.041255	0.03411	0.02574	0.038808	0.028464	0.033176	0.048386	0.030881	0.034277	0.034233
9	4.98	3	0.05333	0.08676	0.053444	0.055565	0.049919	0.036647	0.040007	0.075038	0.039129	0.043076	0.066967	0.05272	0.042147	0.039294
10	6.64	4	0.063431	0.109656	0.063605	0.076114	0.058147	0.042702	0.04654	0.098992	0.047061	0.048965	0.113181	0.088096	0.048008	0.045588
11	8.3	5	0.075087	0.13122	0.086434	0.10762	0.064622	0.046747	0.069829	0.155287	0.056851	0.072262	0.251505	0.102159	0.051449	0.051849
12	9.96	6	0.088102	3.96354	0.11715	0.168316	0.069869	0.049698	0.08257	0.241763	0.07139	0.089099	0.333503	0.110684	0.057478	0.057478
13	11.62	7	0.112156	0.288852	0.161433	0.238404	0.072822	0.05027	0.121792	0.08957	0.081155	0.101465	2.57434	0.114979	0.066562	0.061859
14	13.28	8	0.123727	3.93333	0.064956	0.293002	0.085568	0.053059	0.309005	0.128148	0.085833	0.112101	0.647554	0.12133	0.073675	0.063132
15	14.94	9	0.16931	0.604083	0.310564	0.403512	0.094965	0.051446	0.468244	5.72883	0.094149	0.106628	1.46596	0.119499	0.085118	0.065271

IDA Analysis for first wire fracture at 7.00%

iii. Max Displacement

Increment Number	SA(T1)	γ	M1 u_{peak}	M2 u_{peak}	M3 u_{peak}	M4 u_{peak}	M5 u_{peak}	M6 u_{peak}	M7 u_{peak}	M8 u_{peak}	M9 u_{peak}	M10 u_{peak}	M11 u_{peak}	M12 u_{peak}	M13 u_{peak}	M14 u_{peak}	M15 u_{peak}
1	0.415	0.25	0.67882	0.500985	0.571583	0.889382	0.457474	0.641626	0.311821	0.479277	0.388274	0.953687	0.233649	0.488534	0.69869	0.84989	0.91868
2	0.83	0.5	3.1509	2.755458	0.904898	1.05302	1.006157	1.711211	1.220647	0.915313	1.387102	1.762029	0.747821	0.829476	1.171694	1.126984	1.007361
3	1.245	0.75	3.292002	3.428856	2.065554	2.715732	2.076264	3.453336	2.907144	2.382264	1.84113	4.496436	2.15019	1.278146	1.813248	1.598908	2.444544
4	1.66	1	4.818762	4.369806	2.481174	3.761226	2.059182	4.525254	3.502926	4.8591	2.271564	6.722622	3.869874	1.307873	2.272284	2.09385	4.390542
5	2.075	1.25	5.293296	5.3064	5.324454	3.55455	2.796426	5.083938	3.570444	6.579738	5.168772	7.259724	4.377906	2.78595	2.48958	2.52864	4.934412
6	2.49	1.5	4.802702	4.876862	5.342818	3.376987	3.103416	4.30092	4.611816	7.191331	5.13419	6.661973	4.725922	3.107534	2.930472	2.867515	4.100558
7	2.905	1.75	5.070614	5.619542	6.514157	4.272062	3.947256	4.851374	4.714013	8.091086	6.262301	8.336318	5.872176	4.125845	3.21624	4.183949	4.175626
8	3.32	2	5.345323	6.703589	7.591608	4.987771	4.783824	5.63063	5.020747	9.151805	7.549618	9.61308	7.048368	4.240008	4.925578	4.893379	4.277491
9	4.98	3	9.603648	9.845107	11.11546	6.830222	8.11764	7.573392	6.282979	11.79482	9.414936	12.38619	10.03559	5.804381	5.819962	6.688166	5.637398
10	6.64	4	7.950744	13.37715	15.78946	7.932038	11.40895	8.945856	7.139189	13.9198	17.17718	18.81504	13.00284	7.483594	11.77446	12.16866	7.587
11	8.3	5	10.73543	10.54367	20.13854	8.983411	14.5525	9.380333	10.65216	15.95477	24.95621	25.65677	19.9021	11.00202	17.94154	16.29187	13.42581
12	9.96	6	15.66173	12.61456	22.40597	10.53691	16.64669	11.79482	11.44266	17.97379	28.09598	28.25626	25.17869	14.39755	19.44302	17.16941	19.44072
13	11.62	7	20.5321	14.86094	24.56093	12.7508	20.01571	13.66163	12.8252	20.40566	28.45757	31.8312	25.05658	17.44416	17.78011	19.53259	24.43018
14	13.28	8	22.63478	17.85614	26.18971	15.06701	22.04611	15.50246	13.90599	22.36522	30.92342	16.36128	27.30456	20.4493	14.38674	22.22611	29.19542
15	14.94	9	25.05629	20.60626	27.28498	17.03218	22.70952	17.01749	15.56942	23.72789	35.38411	46.62346	27.97229	23.1025	14.78131	24.22454	32.11978

Increment Number	SA(T1)	γ	M16 u_{peak}	M17 u_{peak}	M18 u_{peak}	M19 u_{peak}	M20 u_{peak}	M21 u_{peak}	M22 u_{peak}	M23 u_{peak}	M24 u_{peak}	M25 u_{peak}	M26 u_{peak}	M27 u_{peak}	M28 u_{peak}	M29 u_{peak}	M30 u_{peak}
1	0.415	0.25	0.653063	0.36473	0.236381	0.160292	0.118591	0.3285	0.152293	0.386066	0.82291	1.032392	0.971314	0.435029	0.347249	0.31522	0.346786
2	0.83	0.5	1.895994	0.642353	0.550778	0.328707	0.245446	1.898334	0.34659	1.128791	1.629637	1.294848	1.022306	1.083933	0.741316	1.332009	0.864736
3	1.245	0.75	2.449116	0.90736	1.660369	0.399328	0.491895	2.66823	1.241258	1.387942	2.122326	4.840578	1.595117	1.429207	1.184976	1.843416	1.842714
4	1.66	1	3.311928	1.22195	4.233204	0.762989	0.863939	3.937896	1.183678	2.031444	5.457222	5.559174	3.764664	1.763118	2.772108	1.900746	2.987478
5	2.075	1.25	3.986946	1.74213	5.534802	1.220722	1.423755	4.793238	4.58388	1.811556	4.921074	7.23753	4.315158	1.933992	4.037796	2.136456	5.640372
6	2.49	1.5	4.174286	1.912594	6.013757	1.14078	2.062555	6.439694	4.363862	2.694096	4.541126	5.547989	3.317155	1.382062	4.854888	1.357811	7.633757
7	2.905	1.75	4.993718	2.204424	7.385717	1.261371	1.738944	8.532936	4.268131	2.93148	5.02488	5.728781	3.329078	1.570608	6.351336	2.359253	9.769378
8	3.32	2	5.504774	3.647866	8.366357	1.970755	1.260091	8.96472	4.852411	3.547195	5.501059	5.764637	3.535056	2.423563	7.307078	2.377627	12.12342
9	4.98	3	6.381749	11.72321	11.52989	3.057898	7.328664	9.309082	7.230082	4.81379	7.501162	7.521682	5.184662	3.849696	11.25789	6.234235	17.38454
10	6.64	4	7.358227	16.69018	14.59238	4.355554	9.451426	12.33101	7.220318	6.529205	10.2092	10.74393	8.192765	6.128611	15.90019	11.2178	20.00952
11	8.3	5	9.596549	20.79101	17.23032	4.049525	9.903931	15.87773	9.195883	7.520054	13.5391	16.69723	7.761643	6.416885	19.74902	12.97459	22.12963
12	9.96	6	11.89679	23.42995	18.86054	4.395571	13.58846	17.93102	10.01831	9.350078	16.74389	12.33809	7.390109	6.923707	22.86605	5.15124	17.06861
13	11.62	7	13.81177	28.62331	19.24186	5.772528	18.58003	22.13957	11.175	10.09986	19.02629	6.49381	4.573382	7.870824	25.1316	5.77813	25.66008
14	13.28	8	17.38181	33.32693	21.44117	9.843696	25.03973	27.38506	15.97565	12.13026	21.17462	6.61356	3.729859	8.71897	27.44986	3.503102	18.96754
15	14.94	9	18.67954	38.35728	24.04483	11.26683	33.82891	32.42563	17.99554	12.93185	23.58994	17.75837	8.414726	10.15567	28.9931	15.81538	9.308765

Increment Number	SA(T1)	γ	M31 u_{peak}	M32 u_{peak}	M33 u_{peak}	M34 u_{peak}	M35 u_{peak}	M36 u_{peak}	M37 u_{peak}	M38 u_{peak}	M39 u_{peak}	M40 u_{peak}	M41 u_{peak}	M42 u_{peak}	M43 u_{peak}	M44 u_{peak}
1	0.415	0.25	0.423841	0.175778	0.460908	0.573511	0.607468	0.427918	0.183182	0.186257	0.653537	0.639767	0.556171	0.319484	0.339921	0.859054
2	0.83	0.5	0.737073	0.387612	1.32296	0.880704	1.729723	0.679579	0.786479	0.390281	1.094908	1.532918	2.363598	0.462152	0.981504	1.627999
3	1.245	0.75	1.021504	0.654455	2.393262	2.503944	2.779128	1.175611	0.75319	1.815912	1.175846	1.805724	4.043052	1.583116	1.519335	2.33433
4	1.66	1	1.514918	0.566798	3.137274	3.262752	3.215214	2.054484	1.219865	2.410884	1.168834	2.386638	4.777668	1.862874	1.904904	2.60478
5	2.075	1.25	3.809862	0.817353	4.137678	3.857454	3.648132	2.650554	1.669981	3.15153	2.585106	3.198276	5.650362	2.928186	2.791584	2.698488
6	2.49	1.5	3.573202	3.83927	4.143312	3.53016	3.620491	2.974781	1.47361	2.842632	2.117923	2.918059	5.337029	2.326579	2.842546	2.765261
7	2.905	1.75	5.001293	6.537442	4.884221	4.724323	4.703832	3.553963	3.92459	2.473834	3.609259	6.200294	3.986741	3.38125	3.519864	
8	3.32	2	5.945746	9.100195	5.561266	5.384736	5.473238	3.891816	2.028312	4.925952	2.639664	3.661502	7.09691	3.196282	3.890678	3.931834
9	4.98	3	8.138563	14.44075	8.133926	8.593416	7.461317	4.440989	5.199595	12.33953	5.078952	5.642856	10.92712	7.984786	5.702141	5.121979
10	6.64	4	10.07205	18.27734	10.11652	12.58443	9.19129	5.710766	6.634008	16.47994	6.764443	7.322342	18.80179	14.72054	7.016184	6.516173
11	8.3	5	12.61238	21.56674	14.37258	18.04334	10.42775	6.529147	11.28413	22.63997	8.78112	12.01046	27.12456	17.21016	7.992187	7.942234
12	9.96	6	15.10805	24.37618	19.44763	23.61787	11.36832	7.142501	13.62434	26.99107	11.80087	14.59642	31.15584	18.6899	9.739512	9.188093
13	11.62	7	18.65362	29.14387	24.12576	27.28454	12.10854	7.343712	20.08901	30.8111	13.75744	16.77974	35.28	19.38874	11.75905	10.04685
14	13.28	8	21.21379	30.97094	26.73115	30.51086	14.70038	7.885066	29.72851	34.25299	14.67446	18.5063	38.71757	20.36088	12.59906	10.34761
15	14.94	9	24.57029	32.58475	30.60518	33.08011	16.39512	7.728365	32.87837	37.54685	16.24248	17.37	41.70269	20.43187	13.73738	10.62847

iv.   Max Post-Tensioning Strain

Increment Number	SA(T1)	γ	M1 Pt_{peak} Strain	M2 Pt_{peak} Strain	M3 Pt_{peak} Strain	M4 Pt_{peak} Strain	M5 Pt_{peak} Strain	M6 Pt_{peak} Strain	M7 Pt_{peak} Strain	M8 Pt_{peak} Strain	M9 Pt_{peak} Strain	M10 Pt_{peak} Strain	M11 Pt_{peak} Strain	M12 Pt_{peak} Strain	M13 Pt_{peak} Strain	M14 Pt_{peak} Strain	M15 Pt_{peak} Strain
1	0.415	0.25	0.019387	0.018833	0.019042	0.020078	0.018684	0.019263	0.018243	0.018746	0.018465	0.020277	0.018021	0.018775	0.019447	0.019969	0.020173
2	0.83	0.5	0.027895	0.026525	0.020162	0.020628	0.020488	0.022851	0.021184	0.020154	0.021777	0.023039	0.019595	0.019883	0.020978	0.020873	0.020494
3	1.245	0.75	0.028356	0.028924	0.024107	0.026433	0.024121	0.029013	0.027011	0.025173	0.023305	0.032748	0.02441	0.021357	0.023176	0.022487	0.025412
4	1.66	1	0.033923	0.03229	0.025483	0.030102	0.024091	0.032807	0.0292	0.03409	0.024793	0.040849	0.030468	0.021471	0.024806	0.024251	0.032284
5	2.075	1.25	0.035619	0.035783	0.03572	0.02932	0.026634	0.034872	0.029201	0.040251	0.035212	0.042831	0.032297	0.026651	0.025661	0.02577	0.0343
6	2.49	1.5	0.038111	0.038517	0.040598	0.031653	0.030542	0.035987	0.037364	0.048949	0.039753	0.04678	0.037922	0.030448	0.02972	0.029375	0.035027
7	2.905	1.75	0.039382	0.042036	0.045729	0.035861	0.034449	0.0384	0.037892	0.053226	0.044867	0.054302	0.042945	0.035247	0.030972	0.035142	0.0353
8	3.32	2	0.040648	0.046939	0.050734	0.03913	0.03818	0.04199	0.0392	0.058475	0.050553	0.06068	0.048409	0.035617	0.038872	0.038617	0.035782
9	4.98	3	0.060528	0.061403	0.068868	0.047215	0.053384	0.050918	0.044726	0.071516	0.059972	0.075647	0.063032	0.042603	0.042405	0.046302	0.042107
10	6.64	4	0.052389	0.080818	0.092545	0.05197	0.070257	0.057446	0.048623	0.083649	0.102516	0.109734	0.078301	0.05011	0.071277	0.07289	0.050865
11	8.3	5	0.06618	0.06576	0.118506	0.057244	0.087667	0.059556	0.065735	0.095505	0.151609	0.157231	0.11711	0.067836	0.103784	0.095551	0.080749
12	9.96	6	0.091605	0.076205	0.133365	0.065752	0.09936	0.071913	0.070143	0.108214	0.176862	0.174782	0.151036	0.084619	0.113699	0.101977	0.115943
13	11.62	7	0.121002	0.089072	0.147161	0.07723	0.11993	0.081668	0.077564	0.12342	0.178967	0.199699	0.149807	0.102003	0.096486	0.111807	0.146538
14	13.28	8	0.13455	0.105699	0.158298	0.090489	0.132509	0.091718	0.083243	0.148508	0.194421	0.095178	0.167666	0.120326	0.079314	0.128017	0.180334
15	14.94	9	0.148878	0.122476	0.164643	0.101708	0.135867	0.100302	0.091613	0.160022	0.228501	21.3158	0.172921	0.13763	0.079247	0.163403	0.20091

Increment Number	SA(T1)	γ	M16 Pt_{peak} Strain	M17 Pt_{peak} Strain	M18 Pt_{peak} Strain	M19 Pt_{peak} Strain	M20 Pt_{peak} Strain	M21 Pt_{peak} Strain	M22 Pt_{peak} Strain	M23 Pt_{peak} Strain	M24 Pt_{peak} Strain	M25 Pt_{peak} Strain	M26 Pt_{peak} Strain	M27 Pt_{peak} Strain	M28 Pt_{peak} Strain	M29 Pt_{peak} Strain	M30 Pt_{peak} Strain
1	0.415	0.25	0.019288	0.018401	0.018032	0.017851	0.017761	0.018281	0.017821	0.018466	0.019872	0.020575	0.020332	0.018618	0.018351	0.018242	0.018357
2	0.83	0.5	0.023488	0.01927	0.018981	0.018318	0.01807	0.023509	0.020883	0.021509	0.024208	0.021572	0.020623	0.020771	0.019621	0.021546	0.020033
3	1.245	0.75	0.025415	0.020134	0.022675	0.018542	0.018864	0.026219	0.021303	0.021844	0.024208	0.033936	0.022572	0.021872	0.021073	0.023447	0.023304
4	1.66	1	0.028394	0.021193	0.031777	0.019708	0.019966	0.030672	0.021108	0.024036	0.036292	0.03658	0.030094	0.023038	0.02662	0.023701	0.027333
5	2.075	1.25	0.030873	0.023023	0.036629	0.021274	0.021893	0.033719	0.033076	0.023265	0.034284	0.042325	0.031965	0.023656	0.031063	0.024361	0.036905
6	2.49	1.5	0.035391	0.025218	0.043824	0.021939	0.025892	0.045641	0.03624	0.028743	0.036945	0.041648	0.031341	0.023046	0.038314	0.022856	0.051064
7	2.905	1.75	0.039179	0.02651	0.049874	0.022527	0.02452	0.055295	0.035786	0.029648	0.039115	0.042584	0.031548	0.023877	0.045018	0.027117	0.061457
8	3.32	2	0.041461	0.033027	0.054617	0.025545	0.022493	0.057514	0.038541	0.032562	0.041294	0.042062	0.032167	0.027534	0.04947	0.027203	0.074171
9	4.98	3	0.045372	0.071718	0.070288	0.030453	0.049715	0.059251	0.049445	0.038314	0.050249	0.050598	0.039596	0.033859	0.069914	0.044836	0.101367
10	6.64	4	0.049847	0.100004	0.086693	0.036163	0.060011	0.074683	0.045957	0.045957	0.064089	0.045257	0.043983	0.045158	0.092612	0.069329	0.117017
11	8.3	5	0.06073	0.125019	0.102426	0.034768	0.062345	0.095379	0.058428	0.050409	0.079222	0.064459	0.046962	0.045158	0.11449	0.077533	0.128365
12	9.96	6	0.072567	0.166453	0.114054	0.036314	0.081099	0.107614	0.062819	0.059156	0.095427	0.069949	0.05047	0.047349	0.132704	0.042476	0.091135
13	11.62	7	0.082914	0.278281	0.116803	0.042334	0.108329	0.134058	0.068711	0.062534	0.107728	0.055249	0.069733	0.051769	0.16954	0.051866	0.131418
14	13.28	8	0.104134	13.9865	0.124039	0.061733	0.182935	0.23973	0.094807	0.072968	0.118322	0.055346	16.8789	0.055672	1.46387	0.037376	0.10036
15	14.94	9	0.112352	5.84889	0.156203	0.068561	3.89354	0.424955	0.105442	0.076588	0.130405	0.096265	0.062235	0.061982	0.23615	0.095031	0.062467

Increment Number	SA(T1)	γ	M31 Pt_{peak} Strain	M32 Pt_{peak} Strain	M33 Pt_{peak} Strain	M34 Pt_{peak} Strain	M35 Pt_{peak} Strain	M36 Pt_{peak} Strain	M37 Pt_{peak} Strain	M38 Pt_{peak} Strain	M39 Pt_{peak} Strain	M40 Pt_{peak} Strain	M41 Pt_{peak} Strain	M42 Pt_{peak} Strain	M43 Pt_{peak} Strain	M44 Pt_{peak} Strain
1	0.415	0.25	0.018578	0.017877	0.018695	0.019038	0.019151	0.018595	0.017896	0.017898	0.019326	0.019247	0.019006	0.018261	0.018319	0.019964
2	0.83	0.5	0.019585	0.018477	0.021535	0.020046	0.022919	0.019388	0.019728	0.018474	0.020801	0.022357	0.025152	0.018698	0.020387	0.022628
3	1.245	0.75	0.020496	0.019318	0.025211	0.025655	0.026629	0.021072	0.019623	0.023256	0.021061	0.023211	0.031133	0.022434	0.022159	0.025021
4	1.66	1	0.022196	0.019048	0.02786	0.02835	0.028215	0.024044	0.021169	0.025295	0.021052	0.025257	0.03369	0.023445	0.023478	0.02611
5	2.075	1.25	0.030255	0.019842	0.03154	0.030444	0.029754	0.026199	0.022729	0.027923	0.025885	0.028168	0.036771	0.027095	0.026795	0.026279
6	2.49	1.5	0.032553	0.03382	0.032408	0.032408	0.032893	0.030077	0.02333	0.029309	0.026096	0.029892	0.040496	0.027054	0.029567	0.029152
7	2.905	1.75	0.039193	0.046122	0.038643	0.037899	0.037781	0.032617	0.02286	0.034147	0.028144	0.032868	0.044495	0.034412	0.031999	0.032386
8	3.32	2	0.043513	0.058169	0.041756	0.040928	0.041255	0.03411	0.02574	0.038808	0.028464	0.033176	0.048386	0.030881	0.034277	0.034233
9	4.98	3	0.05333	0.08676	0.053444	0.055565	0.049919	0.036647	0.040007	0.075038	0.039129	0.043076	0.066967	0.05272	0.042147	0.039294
10	6.64	4	0.063431	0.109656	0.063605	0.076114	0.058147	0.042702	0.04654	0.098992	0.047061	0.048965	0.113181	0.088096	0.048008	0.045588
11	8.3	5	0.075087	0.13122	0.086434	0.10762	0.064622	0.046747	0.069829	0.155287	0.056851	0.072262	0.251505	0.102159	0.051449	0.051849
12	9.96	6	0.088102	3.96354	0.11715	0.168316	0.069869	0.049698	0.08257	0.241763	0.07139	0.089099	0.333503	0.110684	0.057478	0.057478
13	11.62	7	0.112156	0.288852	0.161433	0.238404	0.072822	0.05027	0.121792	0.08957	0.081155	0.101465	2.57434	0.114979	0.066562	0.061859
14	13.28	8	0.123727	3.93333	0.064956	0.293002	0.085568	0.053059	0.309005	0.128148	0.085833	0.112101	0.647554	0.12133	0.073675	0.063132
15	14.94	9	0.16931	0.604083	0.310564	0.403512	0.094965	0.051446	0.468244	5.72883	0.094149	0.106628	1.46596	0.119499	0.085118	0.065271